SAMPLE - BASED MATERIAL STRUCTURE MODELING

by

Xingchen Liu

A dissertation submitted in partial fulfillment of

the requirements for the degree of

Doctor of Philosophy

(Mechanical Engineering)

at the

UNIVERSITY OF WISCONSIN–MADISON

2017

Date of final oral examination: 12/9/2016

The dissertation is approved by the following members of the Final Oral Committee:

Vadim Shapiro, Professor, Mechanical Engineering

Krishnan Suresh, Professor, Mechanical Engineering

Xiaoping Qian, Associate Professor, Mechanical Engineering

Eftychios Sifakis, Assistant Professor, Computer Sciences

Walter Drugan, Professor, Engineering Physics

Acknowledgments

It is a great pleasure to spend the past six years at UW-Madison. I am very honored and grateful to have Professor Vadim Shapiro as my advisor during my Ph.D. study. I would not be able to complete this thesis without his patience, insight, advice, and years of support and guidance. Working with him not only has been a rewarding and memorable experience but also teaches me the what it takes to succeed as a researcher. I give my most heartfelt thanks to him.

I feel fortunate to also have Professors Krishnan Suresh, Xiaoping Qian, Eftychios Sifakis, and Walter Drugan on my dissertation committee. Their excellent classes, insightful suggestions, constructive criticisms, and general guidance are vital in the completion of this work. In addition, I also owe my gratitude to Professor Ming Yuan for the helpful discussions on the nature and applicability of Markov random field sampling algorithm, and Professors Heidi-Lynn Ploeg and Wenxiao Pan for providing the sample images of bones and batteries that greatly helped my research.

Working at the Spatial Automation Laboratory has given me the opportunity to interact with my colleagues Saigopal Nelaturi, Mikola Lysenko, Vaidyanathan Thiagarajan, Goldy Kumar, Brian McCarthy, Randi Wang, and Yaqi Zhang. I appreciate their friendship and many fruitful discussions. I wish them, and the newer graduate students Xin Liu and Parag Pathak the very best in their endeavors.

I owe much more than I can express here to my family for their unconditional love and support. I especially thank my grandparents for valuing education and instilling that value in me.

Contents

List of Tables

List of Figures

SAMPLE - BASED MATERIAL STRUCTURE MODELING

Xingchen Liu

Under the supervision of Professor Vadim Shapiro

At the University of Wisconsin-Madison

The paradigm of Sample - based Material Structure Modeling is proposed to facilitate the design and manufacturing of material structures towards desired mechanical properties. By modeling material structure samples via a Markov random field, the proposed paradigm views material structure as a collection of neighborhoods. The abstraction facilitates the reconstruction of both periodic and stochastic material structures and extends to the reconstruction and design of spatially varying material structures, a principal mechanism for creating and controlling spatially varying material properties in nature and engineering. The spatially varying material properties are represented and controlled using the notion of material descriptors which include common geometric, statistical, and topological measures such as correlation functions and Minkowski functionals. The proposed method is of particular advantage in preserving the microscopic geometry and related properties of the material structure sample while achieving target macroscopic property distributions during the design of material structures. For material structures that exhibit anisotropy, properly oriented neighborhoods could greatly enhance the efficiency of the material. The expansion of the design space to include the rotation of neighborhoods is appropriate when the properties that need to be preserved can be safely regarded as rotation invariant. With the assumption of orthotropic symmetry, an automatic way to determine the principal axes of neighborhoods for material structure samples with stochastic orientations is proposed.

A Green's function based homogenization method is investigated for the efficient evaluation of the mechanical properties of neighborhoods. The formulated integral equation is converted into a system of linear equations which is shown to be symmetric and positive definite with the appropriate reference material properties and can be solved efficiently using the conjugate gradient

method. The method is verified against physical test results on additively manufactured structures whose material properties are both spatially varying (heterogeneous) and direction dependent (anisotropic). The same formulation also allows the fast estimation of mechanical properties through correlation functions to circumvent the expensive solution of boundary value problems.

Chapter 1

Introduction

1.1 Motivation

Heterogeneous materials, also known as composite materials, are ubiquitous both in nature and among engineering materials. The material heterogeneity stems from the presence of at least two distinct interacting phases (solid, liquid, gas, or void) within the same material volume. Computer models of heterogeneous materials are becoming increasingly important in order to support the latest advances in material science, biomedical applications, and manufacturing. In all cases, the ability to represent the geometry of material phase, often called a material structure, is critical to the ability to visualize, simulate, design, and manufacture natural and man-made objects made of heterogeneous materials.

A variety of methods have been proposed to model heterogeneous material at different scales. On the macroscopic scale, the spatial distribution of material composition has been a major research issue in the field of solid modeling. The research laid the foundation of the CAD system to allow the design of mechanical part with a heterogeneous interior. The formulation assumes that volume fractions suffice to represent the heterogeneous object and different material properties are achieved by the direct composition of the material phases within the same geometric domain. The modeled

material compositions are usually represented by a collection of scalar or vector fields defined over a geometric domain and therefore geometry of material phase are not realized in such models.

At the microscopic scale, the material structure of a heterogeneous material may be parameterized as a typical "unit cell" located at a "location" in space, which is usually referred as a grain - germ model. Both shape and location of the unit cell are governed by some physically justified stochastic process. The advantage of this approach includes the ability to explicitly control, vary, parameterize, and synthesize the material structure procedurally. Unfortunately, only limited classes of materials with simple unit cell geometry and distributions can be accurately modeled since the modeling process requires complete understanding and parameterization of the generative process underlying material – a challenging task even for most common materials such as sandstone [72, 90].

The limited heterogeneous materials that the grain - germ model can model lead to the belief that heterogeneous materials are too complex to model other ways but statistically. In statistics - based models, heterogeneous materials are abstracted by their low-order statistics, such as volume fraction and two-point correlation functions [174, 173]. To generate a material structure from the model, a large-scale stochastic optimization problem is often solved by iteratively matching the statistics. One advantage of the statistics - based approach is its applicability to a broad range of random heterogeneous materials because it does not depend on the stochastic process by which a material structure is formed [157]. However, once the material structure is abstracted by its low-order statistics, important geometric and topological details of the material are usually lost. As a result, different material structures with similar two-point correlation functions may lead to similar models. The stationarity of the material is often assumed since correlation functions are usually measured through the entire material sample and not equipped to parameterize information across different scales.

Texture synthesis in the field of computer graphics and computer vision has matured during the last decade. Texture synthesis aims to create large non-repetitive images from a small input texture.

The term "texture" generally refers to images containing repeated patterns with a certain amount of randomness. During the synthesis process, the new texture is synthesized based on an existing sample such that the resulting pattern and existing sample appear to be generated by the same underlying stochastic process [166]. The texture synthesis process has been proposed for modeling bone scaffold [47] given its applicability to a broad spectrum of textures. The most successful model for graphic application to date is based on the Markov Random Field (MRF), which requires the input texture to be a realization of local and stationary random process.

So far we have only examined the modeling of a single material sample. However, a computer model of the heterogeneous material goes beyond the representation of a single sample: it must account for all possible material samples in the *ensemble*, which comprises all material structures generated with the same formation process. In other words, computer models of a material should be capable of modeling the ensemble, given more and more material samples from the ensemble. Defining a model for an ensemble of material and designing a process capable of generating material samples in that ensemble is the subject of this thesis.

Among the proposed and implemented modeling schemes, the texture synthesis is the only scheme models the detailed geometry of material structures. The model is suited for a broad range of structures without the knowledge of the underlying generative process. In particular, texture synthesis may take multiple material samples as input while other models may require some statistical abstraction of the abstraction they already have. For example, the statistical distribution of the control parameters in the grain - germ model may be used to capture the variation within the ensemble.

Texture synthesis appears to provide the natural machinery to model material structure. Despite the extensive studies of texture synthesis, the study of MRF towards the modeling of two and three-dimensional material structures in the engineering design setting is rather limited. In the present study, we extend this approach to model and design material structures both in 2D and 3D. Note that texture synthesis is an algorithm to sample from the underlying MRF model. It

is important to study properties of both MRF and its sampling algorithm so that it is clear what material properties are being preserved, what information of material structure is lost, and how design constraints are enforced during the design of new material structures with respect to both the MRF model and its sampling algorithm. In order to model a material structure with MRF in a more formal engineering design setting, we intend to investigate the following questions:

- What is MRF and how to model a heterogeneous material by MRF? As computer models are simplification and abstraction of the real physical objects or phenomenon, what are the properties of the sample material persevered by MRF model and what information is lost?
- MRF generalizes Ising model by extending interactions between the nearest neighbors to the interactions within a neighborhood window. The question follows immediately is how to choose the optimal neighborhood size for MRF model.
- Material structures are generated by sampling the MRF model. What are the methods available to sample from the MRF? Even though texture synthesis can generate visually similar results, what, if any, material properties are preserved in the texture synthesis process? What is the limitation of the texture synthesis process?
- What is the design space enabled by the MRF model for a given material sample / ensemble? How to modify the design space so that different material structure can be generated?
- Non-stationary heterogeneous material sample enables a design space with spatially varying material structure and subsequently functionally graded macroscopic material properties. As MRF is inherently non-parametric, how to enable the parametric control of spatially varying material properties? How does such control affect the design space?
- Evaluation of mechanical and structural performance is essential in the design of functional material structures. Such process generally involves solving boundary value problem, which is computationally intensive for heterogeneous materials. The successful application of

the proposed method hinges on the question: how to represent and evaluate the material properties efficiently and accurately?

- To serve different design objectives, such as a more efficient use of the material, how to expand the design space defined by the sample material structure? Which material properties are preserved under the expansion?

1.2 Proposed approach

In the present study, the paradigm of *Sample - based Material Structure Modeling* is proposed to facilitate the design and manufacturing of material structures towards desired structural and mechanical properties while persevering microscopic geometry of the sample material structure. By modeling material structure sample via a Markov random field, the proposed paradigm views a material structure as a collection of neighborhoods. The design space enabled by the MRF model for a given material sample includes all the material structures that share the same set of neighborhoods. When the stationarity of the sample material structure can be safely assumed, the design space can be efficiently sampled by Wei - Levoy algorithm with the properly chosen neighborhoods.

Spatial variation of material structures is a principal mechanism for creating and controlling spatially varying material properties in nature and engineering. While the spatially varying homogenized properties can be represented by scalar and vector fields on the macroscopic scale, explicit microscopic structures of constituent phases are required to facilitate the visualization, analysis and manufacturing of functionally graded material (FGM). The challenge of FGM structure modeling lies in the integration of these two scales. As MRF is inherently non-parametric comparing with other microscopic models, the spatial variation of material structures cannot be controlled within the MRF. In addition, Wei - Levoy algorithm no longer samples the design space correctly when the sample material is not stationary on the macroscopic scale. Given the design objective of the present study, we propose to model the spatial variation of material structure on the macroscopic scale

by material properties while preserving the material structure geometry on the microscopic scale with MRF. Such formulation reduces the difficult inverse homogenization problem to a problem of filtering and leads to the modification of Wei - Levoy algorithm immediately: only neighborhoods with desired material properties will be selected for use in the designed material structure.

In addition to being functionally graded, many natural and man-made materials are also anisotropic. Whereas the above formulation only controls the position of neighborhoods, properly oriented material structures could greatly enhance not only the efficiency of the material but also the target performance of the designed structure. For material samples with non-uniform orientations, an automatic way to determine the orientations of neighborhoods directly from the target material properties is proposed. Since simply selecting neighborhoods with desired orientations eliminates too many suitable neighborhoods, we expand the design space to include the rotation of neighborhoods. The expansion is enabled by the modification of sampling process rather than preparing multiple samples of rotated neighborhoods to minimize the impact on the computational efficiency of the sampling process. Such expansion of the design space is appropriate when the properties that need to be preserved can be safely regarded as rotational invariant.

Given the extensive researches on relating material descriptors with physical properties, we propose to represent and control spatially varying material properties using the notion of material descriptors which include common geometric, statistical, and topological measures such as correlation functions and Minkowski functionals. Associating material properties with descriptors is also independent of the artificial connections between control parameters and the material structure in a procedural model. To circumvent the expensive solution of boundary value problem, a Green's function based homogenization method is investigated for the efficient evaluation of the mechanical properties.

Given a sample of material, its material structure may be digitized using a variety of imaging techniques producing a 3D image (bitmap, gray-scale, or color), which can be used for a number of diagnostic or simulation purposes [86, 71]. Three-dimensional images can be acquired by micro

computer tomography (μCT) and magnetic resonance imaging (MRI). We rely on the sampling with a regularly spaced lattice, i.e. pixels and voxels, as the primary representation in the present work.

1.3 Contributions

This thesis introduces the paradigm of the sample - based material structure modeling, a unified model to represent both microscopic scale material geometry and macroscopic material properties. The thesis is constituted by four major contributions:

1. **Material structure modeling by neighborhoods**, in which we show Wei - Levoy algorithm preserves material descriptors and therefore properties of the sample material. In addition, we propose and verify a systematic approach to determine the optimal size of neighborhoods based on the two-point correlation function.

2. **Functionally graded material structure design by material descriptors**, in which we use material descriptors to represent and evaluation the spatially varying material properties. We also propose a hybrid approach to integrate the material descriptors into the MRF sampling process.

3. **Efficient material property estimations by FFT-based homogenization**, in which we show that the integral equation formulated by the Green's function is symmetric and positive definite therefore can be solved efficiently through conjugate gradient method. In addition, a geometry - material model is proposed for structures manufactured by Fused Deposition Modeling process.

4. **Material structure design with varying neighborhood orientations**, in which we propose an automatic way to determine the orientations of anisotropic materials. We show that the proposed method enhance the efficiency of material by sampling MRF with rotated neighborhoods.

1.4 Outline

In Chapter 2, we start with a detailed exposition of heterogeneous material modeling approaches, including material composition models on the macroscopic scale, statistical models, grain - germ model, and texture synthesis on the microscopic scale, and proceed to a brief introduction of Markov random field model for heterogeneous material modeling and different sampling process, including Wei - Levoy algorithm [166], the most fundamental algorithm in textures synthesis. We then review the material descriptors that are geometric, statistical, and topological measures of the material structure. We limit our focus on correlation functions and Minkowski functional for their well-established relationships with various physical properties. Related work on material anisotropy characterization is also reviewed in preparation for Chapter 6. We finish up with a brief review of the effective material property and previous results on homogenization.

In Chapter 3, we investigate the modeling of stationary material structures by defining the design space enabled by sample - based material structure modeling as material structures that shares the same set of neighborhoods with the given material sample. Building on the results by Levina and Bickel [76], we show that, inside a predefined neighborhood window, Wei - Levoy algorithm sample the design space while preserving any material described in the reconstruction result. This set of material descriptors includes not only two-point correlation functions, but also higher order correlation functions; not only Minkowski functionals densities but also the cumulative distribution of Minkowski functionals. In addition, we measure and find good agreements on the effective elasticity tensor between the sample and reconstructed result. Assuming the existence of a germ-grain model of the material sample, we propose and verify a systematic approach to determine the optimal neighborhood size, a key parameter in the MRF model, based on the two-point correlation function. Our implementation employs the Gaussian pyramid to make the Wei-Levoy algorithm parallelable and suitable for the integration into the existing CAD system as a query-based method. Examples show the abstraction facilitates the reconstruction of both periodic and stochastic material

structures.

In Chapter 4, we generalize the model proposed in Chapter 3 to facilitate the design and reconstruction of non-stationary material structures. We propose to formulate the spatial variation of material structures on the macroscopic scale by material properties directly. Such formulation results in two different ways to modify the Wei - Levoy algorithm: use the difference in material properties between neighborhoods and target properties field as a penalty term in the neighborhood selection process or use the difference as a filter to remove neighborhoods without the target material properties. The former is favorable in computer graphics applications while the latter has a clearer meaning of the design space which is the intersection of design space defined by the MRF and by the material properties. The design space defined by the material properties includes all material structures share the same macroscopic material property distribution. We compare the two approaches and find that due to the intersection, the latter approach may not have a non-empty design space to sample from. A hybrid approach is proposed by adding a tolerance to the target properties field and using the difference in material properties as a penalty term to select the neighborhoods. The hybrid approach not only increases the efficiency of the sampling algorithm but also has a well-defined design space. To circumvent the expensive solution of boundary value problem, the spatially varying material properties are represented and controlled using the notion of material descriptors which include common geometric, statistical, and topological measures such as correlation functions and Minkowski functionals.

In Chapter 5, a Green's function based homogenization method is investigated for the efficient evaluation of the mechanical properties of the neighborhoods. The formulated integral equation is converted into a system of linear equations which is shown to be symmetric and positive definite with the appropriate reference material property and therefore can be solved efficiently using the conjugate gradient method. The method is verified against physical test results on additively manufactured structures whose the material properties are both spatially varying (heterogeneity) and direction dependent (anisotropy). The same formulation also allows the fast estimation of

mechanical properties through correlation functions and therefore allows the proposed model to be independent of the artificial connections between control parameters and the material structure in a procedural model.

A vast majority of natural or synthetic materials are characterized by their anisotropic properties, such as stiffness. Such anisotropy is effected by the spatial distribution of the fine-scale structure and/or anisotropy of the constituent phases at a finer scale. In design, proper control of the anisotropy may greatly enhance the efficiency and performance of synthesized structures. In Chapter 6, we propose a sample-based two-scale structure synthesis approach that explicitly controls anisotropic effective material properties of the structure on the coarse scale by orienting sampled material neighborhoods at the fine scale. We first characterize the non-uniform orientations distribution of the sample structure by showing that the principal axes of an orthotropic material may be determined by the eigenvalue decomposition of its effective stiffness tensor. Such effective stiffness tensors can be efficiently estimated based on the two-point correlation functions of the fine-scale structures. Then we synthesize the two-scale structure by rotating fine-scale structures from the sample to follow a given target orientation field. The effectiveness of the proposed approach is demonstrated through examples in both 2D and 3D.

In Chapter 7, we summarize the contributions of this thesis and discuss extensions and open issue in the sample - based material structure modeling. Formulating material structure as Markov Random Fields leads to a number of advantages over the traditional modeling approaches, including improved computational efficiency, the direct extension to anisotropic and multiphase materials, preservation of material descriptors and material properties yet flexible enough to model the macroscopic properties variations.

Last but not least, we note that the concept of "material" is relative because the challenge of modeling and representing the geometry of a material phase transcends the scales: it arises in the modeling of nano-materials [175], mineral formations [72, 90], manufactured composites structures [156, 24], and galaxies [92, 148].

Chapter 2

Related work

In this chapter, we start with a detailed exposition of heterogeneous material modeling approaches, including material composition models on the macroscopic scale, statistical models, grain - germ model, and texture synthesis on the microscopic scale in Section 1. In Section 2, we proceed with the review of material descriptors that are geometric, statistical, and topological measures of the material structure. We limit our focus on correlation functions and Minkowski functional for their well-established relationships with various physical properties. Related work on material anisotropy characterization is also review in preparation for Chapter 6. We finish up with a brief review of the effective material property and previous results on homogenization in Section 3.

2.1 Heterogeneous material modeling

2.1.1 Material composition modeling

Modeling of material composition has been a major research issue in solid modeling. The functionally graded material properties are usually represented compositionally by a collection of scalar or vector fields defined over a geometric domain (Figure 2.1). Without trying to be exhaustive, the following is a small sample of work in this area. Park et al. [115] use a volumetric multi-texturing

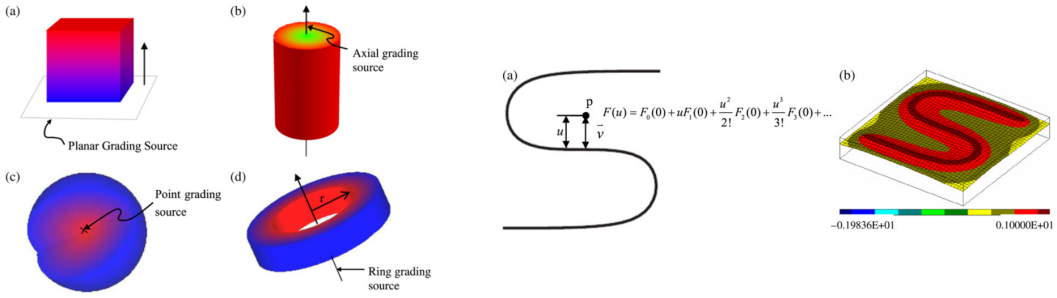

Figure 2.1: Functionally graded material properties design. Left: "Source-base" heterogeneous solid modeling. Right: Heterogeneous material modeling with distance fields. Image courtesy of [138] and [13].

method representing a three-dimensional density gradient. Siu and Tan [138] model both the distribution and the orientations of composite laminates through a source based scheme. Biswas et al. [13] formulate the material function as an interpolation of properties associated with given material features by inverse distance weighting. Other representations of material function are largely consistent with different ways to represent solids, including explicit functions [77, 50], implicit representations [116] and spline tensor products [121, 50], to cite a few. Readers may refer [65] for a survey. In addition, the iterative updating of material composition allows to optimize some material property functions for thermal stress [49], displacement [23] and structural weight [178].

Material composition modeling essentially imposes no constraints on the design space of microscopic material geometry since the ability to generate material structures from the designed material composition is generally assumed [65]. However, a blend of the constituent phases by their volume fractions cannot accurately represent the required spatially varying properties, as it does not carry geometry or topology information about the material structure [114, 157, 72]. Even though material composition models are unable to directly produce the material structure, they are useful in modeling and design of the target descriptor and property fields in the proposed paradigm.

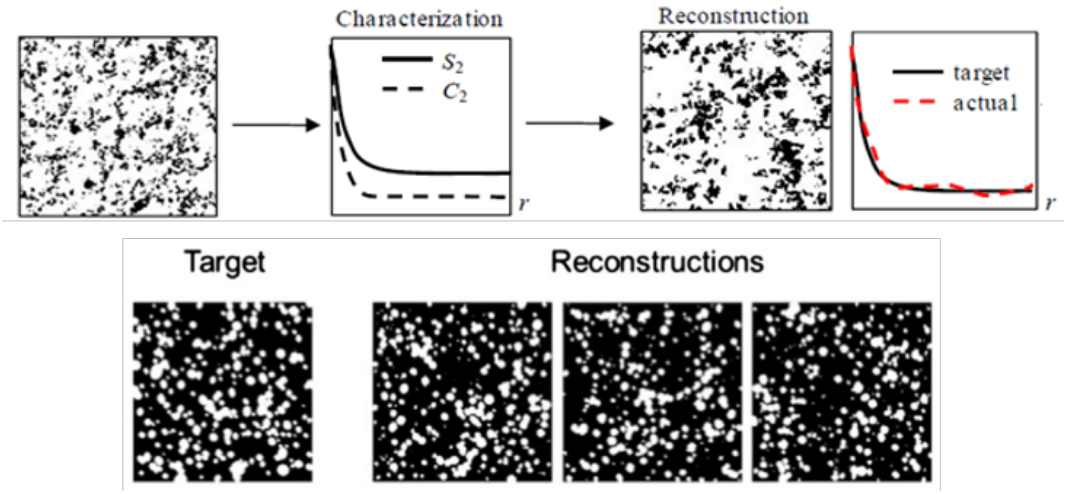

Figure 2.2: The framework of optimization - based reconstruction method. r is the distance in pixels, S_2 is two-point correlation, and C_2 is two-point cluster correlation, "target" refers to the correlations of the digitized medium, "actual" are the correlations of the reconstructed material. Image courtesy of [84].

2.1.2 Statistical modeling

At the microscopic scale, the material structure has been modeled statistically through material descriptors, such as volume fraction and correlation functions [174, 173]. The design space defined by such model includes an ensemble of material structures that share the given set of material descriptors. The process of sampling design space to generate a material structure is commonly referred as reconstruction. Reconstruction seeks to generate material structures directly from the given descriptors (see Figure 2.2). The most common approach focuses on matching material descriptors, especially two-point correlation functions between a given reference material and the desired reconstruction result, by solving a large-scale stochastic optimization problem [174, 57]. Popular optimization algorithms include simulated annealing [174, 28, 56] and termite algorithm [130]. One advantage of the optimization-based approach is its applicability to a broad range of random heterogeneous materials because it does not depend on the stochastic process by which a material structure is formed [157].

Since the objective function is optimized globally (everywhere in reconstruction result), the convergence speed for stochastic optimization is generally very slow, making this approach computationally expensive. This is a major shortcoming of all optimization-based approaches. When the reference structure is abstracted by its descriptors, important structural details of the reference material are often lost. Efforts to address this accuracy issue include using higher order correlation functions [39], incorporating two-point cluster function into the target function of the optimization as a hybrid method [58], and implementing a dilation-erosion scheme [40]. Instead of updating the reconstructed structure directly, Koutsourelakis and Deodatis iteratively updated two-point correlation functions from intermediate Gaussian random fields [68]. While their method cannot include material descriptors other than two-point correlation functions, it converges faster than other optimization-based methods as a much smaller material structure space is explored. However, once the geometric and topological information about the structure is lost, it cannot be fully recovered. Thus, different material structures with similar descriptors may lead to similar reconstruction results.

The statistical models are also limited in their ability to capture more complex material geometry, for example for anisotropic materials and those based on grayscale image samples. More complexed material descriptors need to be involved when structure morphologies can not be captured by the simple material descriptors, e.g. isotropic two-point correlation function, which could be prohibitively expensive in computation. The functional gradation of macroscopic material properties is also limited by such model.

2.1.3 Grain - germ model

The structure of a random heterogeneous material may be parameterized as a typical "unit" cell located at a "location" in space. Both shape and location of the unit cell are governed by some physically justified stochastic process. Such models have been studied extensively in stochastic geometry [62, 142], statistical physics [97, 89], and spatial statistics [148, 141, 97] and have numerous

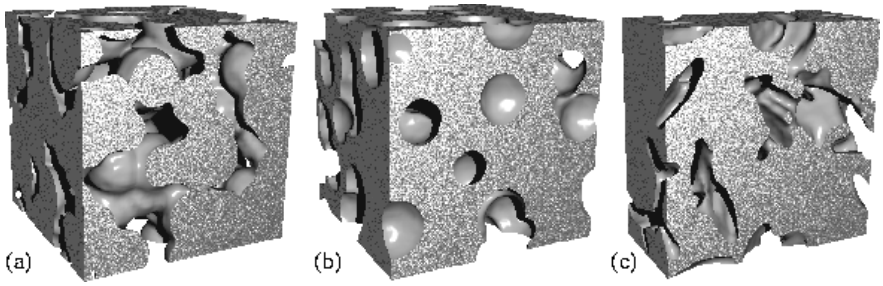

Figure 2.3: Boolean models of porous media. (a) Overlapping solid spheres, (b) spherical pores and (c) oblate spheroidal pores (aspect ratio four). Image courtesy of [125].

applications ranging from stereology [152], to geostatistics [149] and cosmology [92, 148], to name a few.

Using the standard terminology [141], we will refer to the shape of the unit cell as *grain* and its location as *germ*. A material model is generated by placing grains at germs and composing them into a material structure, for example, using Boolean set operations [130, 143] (see Figure 2.3), packing subject to non-interference (random sequential adsorption model) [157] or minimum distance constraints [122]. Typically, a grain is a random compact subset of Euclidean space, while a germ may be a sequence of locations governed by a stochastic (for example, Poisson) process. More generally, germs may be used to specify locations (positions and orientations) of more general unit cells that may include Voronoi cells, hyperplane arrangements, periodic lattice and cellular structures, and so on. For example, a masonry wall can be modeled by two stochastic processes: one to generate locations of stones (germs) and another one to generate the shapes of the stones (grains) [139]. The advantages of the generative approach include the ability to explicitly control, vary, parameterize, and synthesize the resulting material structures in the material ensemble. Unfortunately, this also requires complete understanding and parameterization of the generative process underlying the ensemble – a challenging task even for most common materials such as sandstone [72, 90].

Most of the researches in grain - germ models may be classified in terms of the proposed model for germ, grain, and the process by which they are composed to form the material structure. Reviews

Figure 2.4: A procedural porous structure model. (a) The control polygons used for B-Spline curve fitting. (b) The pore geometries represented by B-Spline curves. (c) Boolean subtraction of the pores from the external geometry and the resultant 2D representation of the irregular porous structure. Image courtesy of [66].

of various stationary stochastic models used for generating random heterogeneous materials may be found in [141] and [157]. Numerous advances in computer-aided design and manufacturing are based on similar ideas. Without trying to be exhaustive, the following is a small sample of recent work in this area. Kou and Tan [66, 67] proposed using random Voronoi tessellation, with grains bounded by B-Splines to design irregular porous artifacts with controllable pore shapes and distributions without requiring any existing objects as prerequisites (Figure 2.4). Redenbach [122, 123] showed that Laguerre tessellations outperform Voronoi tessellations in the modeling of ceramic and aluminum foams. Pasko *et al.* [117] employed FRep to model both regular lattice and irregular porous material by combining generative and reconstructive approaches through the global optimization in the parameter space of a pseudo-random model. FRep uses an analytic function to define the boundary of the material structure hence its representation is very compact. Multi-scale material structures modeled by FRep can be found in [36]. Significant emphasis has also been placed on designing unit cells with desired mechanical properties that can be used in random or periodic material structures. For example, Chen [21] developed a texture mapping design system to add internal structures into solids, which allows designers to select a material structure from a library. Sigmund [135, 136] used a topology optimization approach to synthesize unit cells with desired or novel material properties in a material structure, for example, materials with negative Poisson's ratio. As shown in [1], constructing a procedural model of random heterogeneous material

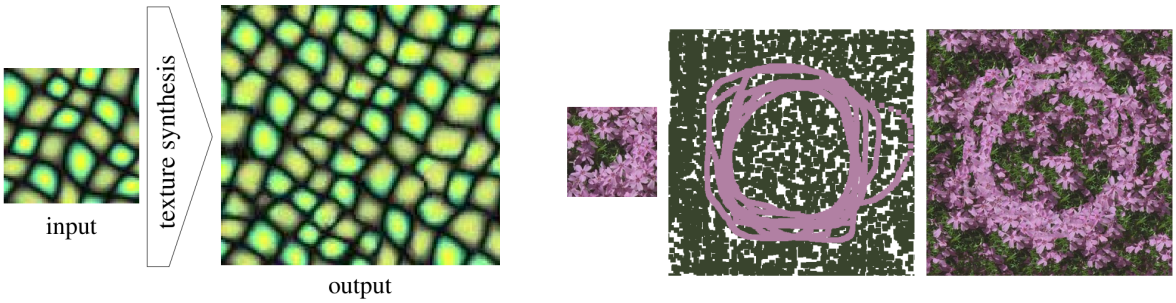

(a) Texture synthesis of stationary texture.

(b) Controlled texture synthesis of graded texture.

Figure 2.5: Texture synthesis. Image courtesy of [165] and [2].

with material descriptors matching a given sample is generally difficult.

The material structure with target material properties may be generated iteratively by updating the model parameters to match the target properties / descriptor fields. However, these models usually limited to certain types of material structures. Even for stationary material structure modeling, grain - germ models require a complete understanding and parameterization of the generative process. To model the FGM compatible with target properties, additional knowledge of the mapping between control variables and material properties is also required. These disadvantages make grain - germ models unattractive for a general approach to modeling heterogeneous material.

2.1.4 Texture synthesis

In computer graphics, the term "texture" generally refers to images containing repeating patterns with a certain amount of randomness [76, 164]. The amount of randomness can vary from regular (a tiled floor) to stochastic (a sand beach), which contribute to a wide spectrum of textures [164, 83]. Texture synthesis techniques are widely used in computer graphics and can be categorized into *procedural* and *example-based* based. Procedural methods generate the texture as a function of image element coordinates based on a set of user-specified parameters. We will not consider procedural texture synthesis methods here because they suffer from the same limitations as the grain - germ modeling approaches.

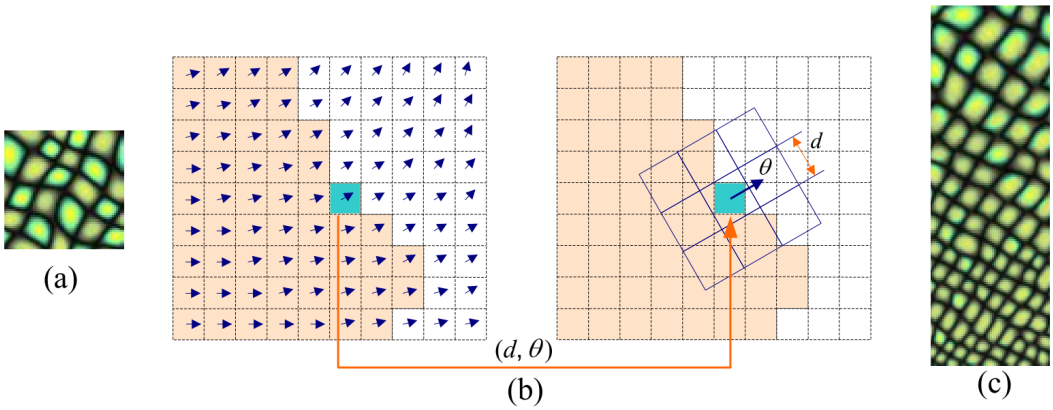

Figure 2.6: Texture synthesis with orientation control. (a) Homogeneous texture sample. (b) Field distortion synthesis. (c) Synthesis result. The green blobs are made progressively smaller towards the right. Image courtesy of [177].

Example-based texture synthesis aims to create large non-repetitive images from small sample image (Figure 2.5(a)). During the synthesis process, new images are synthesized based on an existing sample such that the resulting pattern and existing sample appear to be generated by the same underlying stochastic process [166]. Early uses of MRF focused on identification of parametric texture models, which rely on user-estimated parameters and have limited use to users in the presence of complex textures [113, 31]. More recently, MRF model proved to be highly successful as a basis for non-parametric texture synthesis.

The classical texture synthesis can reconstruct only stationary material structures that remain (statistically) invariant under translation. Such structures cannot be graded in a controlled fashion. Researches in the computer graphics community have developed useful techniques for controlling texture synthesis in non-stationary situations. In chronological order, Ashikhmin [2] use a user-painted color map to control the placement of purple flowers and green grass (Figure 2.5(b)). The same technique is used by Efros and Freeman [34] to transfer Picasso's drawing onto a picture of Richard Feynman. Zhang et al. [177] employ a scalar field together with a vector field to control both size (scale) and direction of textures. For feature size control, the idea of texton mask is introduced to create varying textures from stationary inputs, which may also be used

to smoothly blend two different textures. This idea was extended into a warp field in [93], so that the texture may be seamlessly morphed from one to another. For a complete review, readers may refer to Section 9 of [165]. All these methods follow the same basic idea, also adapted in our approach: an external control field can be used to influence and to guide placement of the next pixel (patch or material element). This relaxes the requirement of global stationarity in texture synthesis process and makes it controllable. Texture synthesis techniques have recently been used for material reconstruction by several researchers [47, 79, 15, 70]. In particular, Liu and Shapiro [79] demonstrated that Markov random field texture synthesis can be used to reconstruct a variety of periodic and random heterogeneous structures while preserving their geometric, topological, and physical properties. We will show more details of the texture synthesis algorithm as well as the underlying Markov random field model in the following section.

2.2 Material descriptors

In view of the complexity of the geometry, material descriptors have been employed to statistically characterize the material structures. One apparent material descriptor is the volume fraction ϕ occupied by a certain phase inside the material sample, such as material phase for porous material or particle phase for composite material. The Voigt-Reuss bound and tighter Hashin-Shtrikman bounds for modulus of isotropic material structure have been developed based on this first order statistic (see next section). However, as discussed in the previous section, volume fraction is a very weak material descriptor. It is widely accepted that the physical properties of heterogeneous material are highly correlated with its material structure [72, 86, 157, 114]. So it is crucial to have descriptors that are able to quantify the spatial arrangement as well as the connectivity and the geometry of phases inside heterogeneous material.

2.2.1 Correlation functions

Correlation functions have been developed specifically to quantitatively ascertain the distribution of distances between phases and are used widely in stochastic geometry [62, 142] and stereology [142]. An *n*-point correlation function can be defined as a probability that all vertices of a randomly tossed n-vertex polyhedron fall into the same phase of a material structure.

For a heterogeneous material, the indicator function $I^{(i)}(\mathbf{x})$ is defined as:

$$I^{(i)}(\mathbf{x}) = \begin{cases} 1, & \text{if } \mathbf{x} \text{ lies in phase } i, \\ 0, & \text{otherwise.} \end{cases}$$

With the assumption that the material is statistically homogeneous (also called spatially stationary), i.e. the stochastic process is translationally invariant, *n*-point correlation of phase i can be formulated mathematically as:

$$S_n^{(i)}(\mathbf{r}_1, \mathbf{r}_2, \ldots, \mathbf{r}_n) = S_n^{(i)}(\mathbf{x}_2 - \mathbf{x}_1, \mathbf{x}_3 - \mathbf{x}_1, \ldots, \mathbf{x}_n - \mathbf{x}_1) = \langle I^{(i)}(\mathbf{x}_1) I^{(i)}(\mathbf{x}_2) \ldots I^{(i)}(\mathbf{x}_n) \rangle$$

where $\langle \ldots \rangle$ denote the expectation (ensemble average) of a function. The first momentum of *n*-point correlation function

$$S_1^{(i)} = \langle I^{(i)}(\mathbf{x}) \rangle$$

is just the volume fraction ϕ. The second momentum is *two*-point correlation function

$$S_2^{(i)}(\mathbf{r}) = \langle I^{(i)}(\mathbf{x}_1) I^{(i)}(\mathbf{x}_2) \rangle$$

which can be described as the probability that a randomly tossed line having both of its ends fall into phase i (either material phase or void phase for a porous material). The *two*-point correlation function can also be written as $S_2^{(i)}(r, \theta, \phi)$, where $\mathbf{r}$ is decomposed into three components: r gives the length while θ and ϕ give the direction of the vector. If the material is also isotropic, i.e., the

material is rotation invariant, the *two*-point correlation function becomes $S_2^{(i)}(r)$. For isotropic media, $S_2^{(i)}(r)$ would degenerate into $S_1^{(i)}(r) = \phi_i$ as $r \to 0$ and converge to ϕ_i^2, since that two points fall into phase i at the same time becomes independent events if the distance between them is outside the correlation range.

Based on the above properties, one can deduce lower order correlation functions from higher order correlation functions, simply by shrinking the distances between sample points to zero. This conceptual shrinking process reveals the lower order correlation information that is already captured by the higher order correlation functions. Thus, the class of material structures sharing the same higher order correlation function is a proper subset of the one defined by lower order correlation function.

Generally speaking, higher order correlation functions yield more information about the material; and the ability of lower order correlation functions to predict many material properties, e.g. those that depend on connectivity, is still undetermined [109]. However, higher order correlation functions are defined over a large configuration space of parameters. First non-trivial instance is the three-point correlation function, which depends on 9 parameters in three dimensional space. And even with the assumption of stationarity and isotropy, an n-point correlation function still needs $\binom{n}{2}$ parameters to be fully defined. As a result, practical use of correlation function beyond order two is rare.

2.2.2 Minkowski functionals

Minkowski functionals are a set of topological and geometrical descriptors of material structure encompassing standard additive measures such as volume, area, mean width and the Euler characteristic [95]. There are precisely $d + 1$ of them in d-dimensional space, i.e. a two dimensional material structure is characterized by three Minkowski functionals, while a three dimensional material structure is characterized by four Minkowski functionals.

One way to approach Minkowski functionals is through Steiner's formula. In three dimensions,

let K be a compact convex body in $\mathbb{R}^3$, with regular boundary $\partial K \in C^2$. Consider the convex body K_ϵ parallel to K at a distance ϵ, i.e.:

$$K_\epsilon = \bigcup_{x \in K} B_\epsilon(x)$$

where $B_\epsilon(x)$ is a ball with radius ϵ. Steiner's formula shows that the volume V_ϵ of K_ϵ

$$V_\epsilon = V + F\epsilon + H\epsilon^2 + \frac{4\pi}{3}\epsilon^3 \tag{2.1}$$

where V, F and H denote the volume, surface area and integral mean curvature of K.

More generally, Steiner's formula for convex bodies in d-dimensional Euclidean space may be written as

$$V_\epsilon(K) = \sum_{\alpha=0}^{d} \binom{d}{\alpha} W_\alpha(K)\epsilon^\alpha$$

whereby the $d+1$ Minkowski functionals W_α are defined. For $d = 3$ we find by comparison

$$W_0(K) = V(K), \quad 3W_1(K) = F(K), \quad 3W_2(K) = H(K), \quad W_3(K) = G(K) = 4\pi\chi(K),$$

One important property the Minskowski functionals have is additivity. Let $\mathcal{K}$ denote the class of closed bounded convex set in $\mathbb{R}^d$. For $K_1, K_2 \in \mathcal{K}$

$$W_\alpha(K_1 \cup K_2) = W_\alpha(K_1) + W_\alpha(K_2) - W_\alpha(K_1 \cap K_2)$$

By induction,

$$W_\alpha\Big(\bigcup_{i=1}^{n} K_i\Big) = \sum_{i=1}^{n} W_\alpha(K_i) - \sum_{i=1}^{n-1}\sum_{j=i+1}^{n} W_\alpha(K_i \cap K_j) + \ldots + (-1)^{n+1} W_\alpha\Big(\bigcap_{i=1}^{n} K_i\Big) \tag{2.2}$$

Equation (2.2) suggests a way to compute non-convex set if such set can be represented as a finite union of $K_i \in \mathcal{K}$. Any material structures represented on lattices (images) fall into this category

since every pixel (voxel) is convex and constitutes the material structure.

What worth to note is that the Hadwiger's theorem of integral geometry characterizes the completeness of the Minkowski functionals. The theorem asserts that any additive, continuous, and motion invariant valuation can be represented as the linear combination of Minkowski functionals.

Minkowski functionals have been proposed as a means to compare or assess the quality of generated or reconstructed material models. For example, it has been shown in [1] that neither particle-based model, model based on level cuts of Gaussian random fields nor models based on Voronoi tesselations of Poisson-distributed points are able to accurately reproduce the Minkowski functionals of the sandstone. Minkowski functionals have also been studied in many other fields, ranging from cosmology [96, 95] to medical image processing and diagnostics (for example, [104] correlates Minkowski functionals with bone diseases such as osteoporosis).

2.2.3 Material anisotropy Characterization

The term anisotropy is overloaded in the context of material structures. Depending on how it is measured, it could refer to structural anisotropy, where the statistics of the structural geometry is anisotropic; it could also refer to property anisotropy, where the effective properties of the material structure are anisotropic. It is widely accepted that the latter is the result of the former combined with the third type of anisotropy: the material anisotropy of the constituent phases materials, which can be regarded as the structure anisotropy from a lower scale.

One common way to characterize the structural anisotropy is measuring the directional variations of average chord lengths, where a chord is a segment of an infinite straight line fully contained in a single phase (see Figure 5.4a). The method is often referred as mean intercept lengths (MIL) in the literature. Such characterization has been widely adopted for the studies of trabecular bones [168, 41, 53, 63]. The distribution of cord lengths is found to have the shapes of ellipses (ellipsoidal in three dimensions) indication the trabecular bones are orthotropic according to these measures.

Minkowski tensors, which are the tensorial generalization of Minkowski functionals, has also

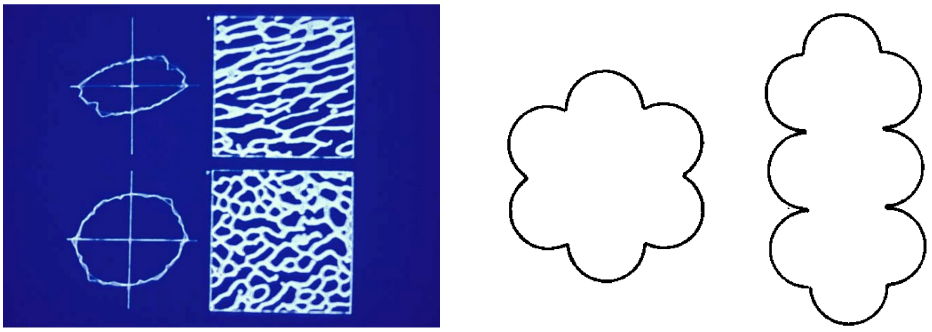

(a) Polar diagram of the Mean Intercept Length function of a cancellous bone.

(b) Two planar figures with identical boundary orientation distributions, which can not be detected by FFT and other boundary based approaches.

Figure 2.7: Existing methods to characterize anisotropy. Image courtesy of [119] and [111].

been used to characterize the structural anisotropy. Measures of anisotropy have been proposed based on eigenvalue ratios of Minkowski tensors [128, 129]. Minkowski tensors have been used in the anisotropy analysis of the shape of neuronal cells [5] and galaxies [6].

In Fourier transform, major structural direction lines in the spatial domain image correspond to high values of frequency components in the frequency domain [160]. As an alternative, Fourier transforms have been applied to characterize the structural anisotropy of electrodeposited patterns [127], trabecular bone [19], and fiber systems [160]. The wavelet transform has also been used to characterize the anisotropy in paper structure [145].

One problem of Fourier transform and wavelet transform is that they measure the boundaries of the phases rather than phases themselves, which may lead to the loss of important anisotropic information, as shown in Figure 5.4(b). Another drawback, which is shared by chord lengths and Minkowski tensors based measures, is that they are not directly related to the physical properties. In view of the descriptor - property relationship, Huber and Gibson [51] associate anisotropy of chord lengths with anisotropy of Young's modulus through an axisymmetric unit cell model proposed in [37]. Good agreements are found between experimental results and proposed formula for polyurethane foams. However, the model is tailored for low-density axisymmetric foams and

cannot be generalized to other material structures. The fabric tensor has been introduced to associate the geometric measurement with the elasticity tensor of heterogeneous material [27]. However, the isotropy of the constituent phases of the heterogeneous material needs to be assumed by the method. Such assumption will be violated when modeling heterogeneous material with anisotropic constituent phases, such as material structures prepared by additive manufacturing [80].

2.3 Effective material properties and homogenization

Tensors are commonly used to represent the constitutive relation in computer simulations of physical problems. Constitutive relation approximates the response of a material to external stimuli and is specific to that material. When the physical problem is one-dimensional, constitutive relation is frequently expressed as a simple proportionality, in the form of a scalar, such as the spring constant. When the physical problem is three-dimensional, the scalar parameter is generalized to a tensor to account for the directional dependence of the material properties.

Being specific to a material, material property tensors are usually constructed from measured material properties or constants. Depending on the physics, fourth-rank tensors and second-rank tensors are commonly used. For example, a fourth rank tensor can be constructed from one or more material properties such as Young's modulus, bulk modulus, shear modulus, Poisson's ratio, Lame parameters, and P-wave modulus that are measured from a single or multiple experiments.

A second rank tensor can be constructed from one or more material properties such as (electrical and thermal) resistivity, (electrical and thermal) conductivity, dielectric constant, magnetic permeability, and diffusion coefficient that are measured from a single or multiple experiments.

2.3.1 Effective material properties

In linear elasticity, the Cauchy stress tensor $\boldsymbol{\sigma}$, with components σ_{ij}, and strain tensor $\boldsymbol{\epsilon}$, with components ϵ_{ij} is related via

$$\boldsymbol{\sigma} = \mathbf{C}\boldsymbol{\epsilon}, \quad \text{or in index notation,} \quad \sigma_{ij} = C_{ijkl}\epsilon_{kl}. \tag{2.3}$$

The elasticity tensor C is determined by a set of six experiments, where six independent components of strain are prescribed while the components of the stress are measured. Alternatively, if the six independent components of stress were prescribed, while the strain components were measured, this leads to a relation based on the compliances tensor $\mathbf{S}$:

$$\boldsymbol{\epsilon} = \mathbf{S}\boldsymbol{\sigma}, \quad \text{or in index notation,} \quad \epsilon_{ij} = S_{ijkl}\sigma_{kl}. \tag{2.4}$$

$\mathbf{S}$ is the inverse of $\mathbf{C}$

$$\mathbf{S}\mathbf{C} = \mathbf{C}\mathbf{S} = \mathbf{I}, \quad \text{or in index notation,} \quad S_{ijkl}C_{klmn} = C_{klmn}S_{ijkl} = \frac{1}{2}(\delta_{im}\delta_{jn} + \delta_{in}\delta_{jm}). \tag{2.5}$$

Let $\overline{\epsilon}$ and $\overline{\sigma}$ be the mean value of stress $\boldsymbol{\epsilon}$ and strain $\boldsymbol{\sigma}$ in the material, their values may be measured or imposed through mean value theorem:

$$\overline{\epsilon}_{ij} := \frac{1}{|\Omega|}\int_{\Omega} \epsilon_{ij}(\mathbf{x})\, d\mathbf{x} = \frac{1}{|\Omega|}\int_{\partial\Omega} \frac{1}{2}(u_i n_j + u_j n_i)\, dS \tag{2.6}$$

and

$$\overline{\sigma}_{ij} := \frac{1}{|\Omega|}\int_{\Omega} \sigma_{ij}(\mathbf{x})\, d\mathbf{x} = \frac{1}{|\Omega|}\int_{\partial\Omega} \frac{1}{2}(t_i x_j + t_j x_i)\, dS \tag{2.7}$$

where Ω is the material domain and $\partial\Omega$ is its boundary.

In the spirit of Equation (2.3), the effective tensor of elastic moduli $\mathbf{C}^{\text{eff},u}$ of a heterogeneous

material is defined:

$$\overline{\boldsymbol{\sigma}} = \mathbf{C}^{\text{eff,u}}\overline{\boldsymbol{\epsilon}}. \tag{2.8}$$

In the spirit of Equation (2.4), the effective tensor of compliances $\mathbf{S}^{\text{eff,t}}$ of a heterogeneous material is defined:

$$\overline{\boldsymbol{\epsilon}} = \mathbf{S}^{\text{eff,t}}\overline{\boldsymbol{\sigma}}. \tag{2.9}$$

In general, $\mathbf{C}^{\text{eff,u}}$ and $\mathbf{S}^{\text{eff,t}}$ are not inverse to each other. However, it is expected that the two becomes inverse to one another if the material is stationary and large enough relative to the material structure. In this case, the superscripts u and t are dropped. Due to the symmetry of the strain and stress tensor, to measure $\mathbf{C}^{\text{eff}}$, a set of experiments measuring stress components with six independent components of strain prescribed is performed. Alternatively, measuring strain components with six independent components of stress prescribed determines $\mathbf{S}^{\text{eff}}$. The stresses and strains are prescribed and measured by Equation 2.6 and 2.7. The common choices for the six independent loads are [181]:

$$\mathbf{u} = \mathbf{E}\mathbf{x} \quad \text{or} \quad \mathbf{t} = \mathbf{L}\mathbf{n} \tag{2.10}$$

with

$$\mathbf{E} \quad \text{or} \quad \mathbf{L} = \begin{bmatrix} a & 0 & 0 \\ 0 & 0 & 0 \\ 0 & 0 & 0 \end{bmatrix}, \begin{bmatrix} 0 & 0 & 0 \\ 0 & a & 0 \\ 0 & 0 & 0 \end{bmatrix}, \begin{bmatrix} 0 & 0 & 0 \\ 0 & 0 & 0 \\ 0 & 0 & a \end{bmatrix}, \begin{bmatrix} 0 & a & 0 \\ a & 0 & 0 \\ 0 & 0 & 0 \end{bmatrix}, \begin{bmatrix} 0 & 0 & 0 \\ 0 & 0 & a \\ 0 & a & 0 \end{bmatrix}, \begin{bmatrix} 0 & 0 & a \\ 0 & 0 & 0 \\ a & 0 & 0 \end{bmatrix}, \tag{2.11}$$

where a is a constant load parameter.

2.3.2 Homogenization

Generally speaking, homogenization refers to the process of calculating effective material properties of a material structure [48, 61]. After decades of development, homogenization methods have

reached a high level of refinement and sophistication. 1960s to 1980s is the golden age for analytical homogenization methods, which can be categorized as rigorous bounds and direct estimations.

Methods evaluating rigorous bounds include the well-known first order Voigt - Reuss bounds and second order Hashin - Shtrikman's bounds for isotropic distribution phase, which will be discussed in detail in the next section. Third order bounds are later developed by Beran [11], Milton [102] and Torquato [159]. Kroner [69] develops a hierarchy of bounds by incorporating higher order statistical information from the material structure. For material structures with a high contrast of phase properties, such as porous materials, the rigorous bounds are usually too slack to give a good estimate of the effective properties.

Direct estimations of the effective properties include Gibson and Ashby's model for cellular structures [38], self-consistent method [46], Mori - Tanaka method [105], to cite a few. Readers may refer [48, 61, 170] for a review. Most direct estimation methods only work on specific morphologies of material structures.

An alternative way to solve effective material properties is to use numerical techniques on samples of material structures. Almost all numerical homogenization methods are based on the concept of a Representative Volume Element (RVE). The RVE is often assumed to be small enough compared with the macroscopic structure so that the analysis on macroscopic level can use the effective properties of the equivalent homogeneous material. Finite element method (FEM) is the most common method to solve the six independent linear elasticity problems discussed in the previous section. However, there are several drawbacks to this approach, including the need to generate a volumetric mesh of the microscopic geometry and the large number of degrees of freedom required by the analysis. Due to these limitations, the complexity of the material structures is limited by FEM. A more recent approach for homogenization is to solve Lippmann-Schwinger equation through Fourier transform and will be discussed in the next section.

2.3.3 Effective stiffness via volume fractions

Voigt - Reuss bounds

The Voigt and Reuss averages (see Figure 2.8) assume that the generated strain and stress fields are constant in the material structure and later shown to be the bounds of the effective material properties by Hill [45]:

$$\frac{1}{2}\overline{\boldsymbol{\epsilon}}(\overline{\mathbf{S}})^{-1}\overline{\boldsymbol{\epsilon}} \leqslant \frac{1}{2}\overline{\boldsymbol{\epsilon}}\mathbf{C}^{\mathrm{eff}}\overline{\boldsymbol{\epsilon}} \leqslant \frac{1}{2}\overline{\boldsymbol{\epsilon}}\overline{\mathbf{C}}\overline{\boldsymbol{\epsilon}} \tag{2.12}$$

where $\overline{\mathbf{C}} = \phi\mathbf{C_1} + (1-\phi)\mathbf{C_2}$ and $\overline{\mathbf{S}}^{-1} = \phi\mathbf{S_1} + (1-\phi)\mathbf{S_2}$.

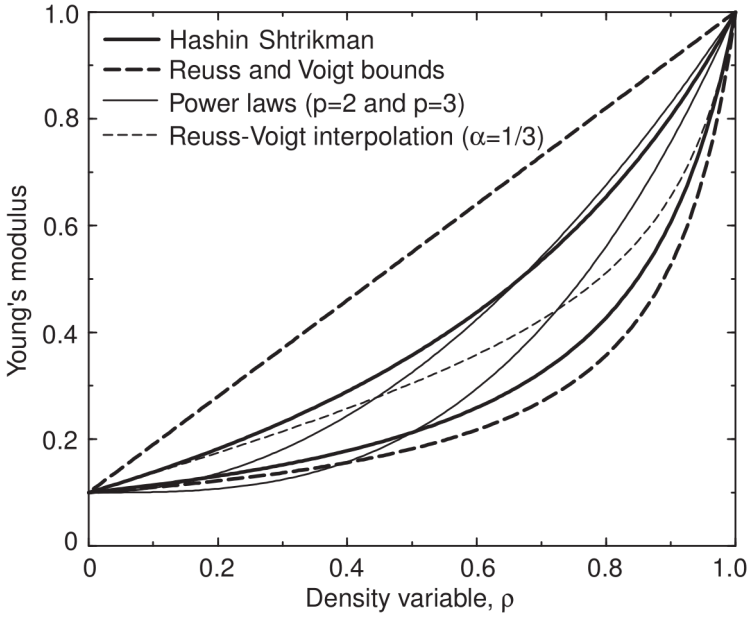

Figure 2.8: A comparison of Voigt - Reuss bounds, Hashin - Strikhman bounds, SIMP models, and the Reuss-Voigt interpolation of two materials with equal Poisson's ratio $\nu = 1/3$, and Young's moduli $E_1 = 1$ and $E_2 = 0.1$. Image courtesy of [9].

Hashin - Shtrikman bounds

Hashin - Shtrikman bounds (see Figure 2.8) are derived from Hashin - Shtrikman variational

principle, for positive- (negative-) definite $\mathbf{C} - \mathbf{C_0}$:

$$\frac{1}{2}\overline{\boldsymbol{\epsilon}}\mathbf{C}^{eff}\overline{\boldsymbol{\epsilon}} \leqslant (\geqslant) \int_{\Omega} \left\{\frac{1}{2}\boldsymbol{\epsilon_0}\mathbf{C_0}\boldsymbol{\epsilon_0} + \boldsymbol{\tau}\boldsymbol{\epsilon_0} - \frac{1}{2}\boldsymbol{\tau}(\mathbf{C} - \mathbf{C_0})^{-1}\boldsymbol{\tau} - \frac{1}{2}\boldsymbol{\tau}\boldsymbol{\Gamma}\boldsymbol{\tau}\right\} d\mathbf{x} \tag{2.13}$$

where $\mathbf{C_0}$ is the constant reference material property, $\boldsymbol{\tau}$ and $\boldsymbol{\Gamma}$ are stress polarization tensor and linear operation involving the second derivative of Green's function as defined in Appendix A. To achieve the bounds, the integrand should be stationary:

$$(\mathbf{C} - \mathbf{C_0})^{-1}\boldsymbol{\tau} + \boldsymbol{\Gamma}\boldsymbol{\tau} = \boldsymbol{\epsilon_0} \tag{2.14}$$

which is the Lippmann - Schwinger equation (Equation 6.3). The variational principle (Equation 2.13) is elegantly derived in [169].

The second - order terms in Equation (2.13) involve the correlation of two spatial locations, which can be represented by two - point correlation functions. If we assume the structural isotropy (in terms of two-point correlation function) of the material structure and approximate $\boldsymbol{\Gamma}$ with its infinite-body form $\tilde{\boldsymbol{\Gamma}}$, Equation (2.13) becomes:

$$\frac{1}{2}\overline{\boldsymbol{\epsilon}}\mathbf{C}^{eff}\overline{\boldsymbol{\epsilon}} \leqslant \frac{1}{2}\overline{\boldsymbol{\epsilon}}\mathbf{C}^{HS}\overline{\boldsymbol{\epsilon}} \tag{2.15}$$

where

$$\mathbf{C}^{HS} = \left\langle [\mathbf{I} + (\mathbf{C} - \mathbf{C^0})\mathbf{P}]^{-1} \right\rangle^{-1} \left\langle [\mathbf{I} + (\mathbf{C} - \mathbf{C^0})\mathbf{P}]^{-1}\mathrm{C} \right\rangle \tag{2.16}$$

$$\mathbf{P} = \frac{1}{4\pi}\int_{|\boldsymbol{\xi}|=1} \tilde{\boldsymbol{\Gamma}}(\boldsymbol{\xi}) dS \tag{2.17}$$

$\mathbf{C}^{HS}$ depends solely on the volume fractions of the constituent phases. Some authors may refer Hashin - Shtrikman bounds as a second order bounds as the isotropy in two-point correlation function is assumed.

Power law

Power law (see Figure 2.8) is a popular material interpolation scheme in topology optimization, SIMP in particular:

$$\mathbf{C} = \phi^{p}\,\mathbf{C^0} \tag{2.18}$$

where p is the penalty factor. For SIMP, in order to obtain the '0 - 1' designs, $p \geqslant 3$ is usually required [9]. However, as shown in Figure (2.8), the power law with $p = 3$ violates the Voigt - Reuss bounds.

Chapter 3

Material structure modeling by neighborhoods

Whereas the equivalence between solids depends on the similarity between their exterior dimensions, the equivalence between material structures is based on the equivalence of their characteristics. Material structure reconstruction is the process of generating material structures that are equivalent to the sample material, involving both modeling of the material structure and generating material structures from the constructed model. Different reconstruction methods can be compared in terms of the amount of characteristic they preserved, how well they are preserved, their abilities to generate equivalent material structures, as well as the number of types of material structures they are applicable to.

In this chapter, we investigate the modeling of material structures by defining the design space as material structures that share the same set of neighborhoods with the given material sample. We start with a brief introduction of Markov random field in the context of heterogeneous material modeling and different ways to sample the MRF model, including Wei - Levoy algorithm [166] – the most fundamental algorithm in textures synthesis. Building on the results by Levina and Bickel [76], we show that, inside a predefined neighborhood window, Wei - Levoy algorithm

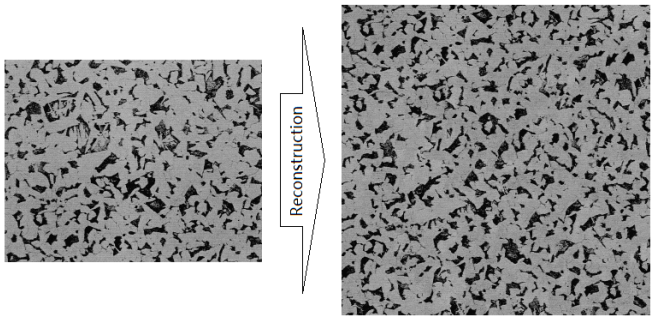

Figure 3.1: The reconstruction of a material structure of coarse pearlite in a matrix of ferrite. The reconstruction result shares similar microstructure descriptors, such as correlation functions and Minkowski functions, with the sample material after thresholding. The relative errors for volume fraction, two-point correlation function, density of perimeter and density of Euler characteristic are 1.6%, 3.8%, 1.3% and 1.7%, respectively. The sample image is reproduced from [30] by courtesy of TMS.

sample the design space while preserving any material descriptors in the reconstruction result. This set of material descriptors includes not only two-point correlation functions, but also higher order correlation functions; not only Minkowski functionals densities but also the cumulative distribution of Minkowski functionals. Based on the homogenization theory discussed in Chapter 5, the perservation of correlation function is equivalent to the perservation of mechanical properties. To verify this result, we measure and find good agreements on the effective elasticity tensor between the sample materials and reconstructed results. In addition, we propose and verify a systematic approach to determine the optimal size of neighborhoods based on the two-point correlation function. Our implementation employs the Gaussian pyramid to make the Wei-Levoy algorithm parallelable and suitable for the integration into the existing CAD system as a query-based method. Examples show the abstraction facilitates the reconstruction of both periodic and stochastic material structures. Some results in this chapter has been reported in [79].

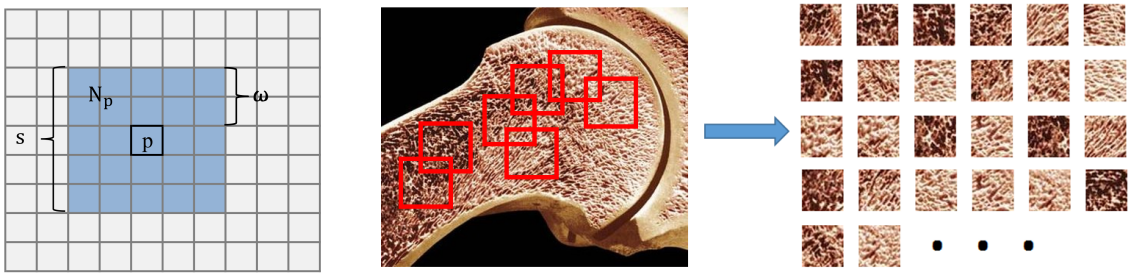

(a) A $s = 2\omega + 1$ neighborhood window N_p located at pixel p; here $\omega = 2$.

(b) Examples of neighborhoods of a trabecular bone structure. Neighborhoods are allowed to overlap.

Figure 3.2: Illustration of neighborhoods.

3.1 Markov random field model and its sampling algorithm

The Markov random field (MRF) contains a set of random variables with the Markov property described by an undirected graph. Markov property assumes that a variable is conditionally independent of all other variables given its neighbors. MRF generalizes the Ising model in the following two ways. First, random variables may take more than binary states. Also, the neighborhood of a random variable is not limited to its immediate neighbors.

Let the heterogeneous material X be a binary image on a d-dimensional lattice (d=2,3). Let t be a d - tuple indexing sites in X: X_t represent the value of X at site t. This notation extends naturally from sites to neighborhoods of sites. Let

$$N(t) = \{s : \|t - s\|_\infty \leqslant \omega, s \neq t\} \tag{3.1}$$

be a $(2\omega + 1)^d$ window centered at site t, then

$$X_{N(t)} = \{X_s : \|t - s\|_\infty \leqslant \omega, s \neq t\} \tag{3.2}$$

is the neighborhood of X_t. For the convenience of comparing the neighborhoods to each other, we

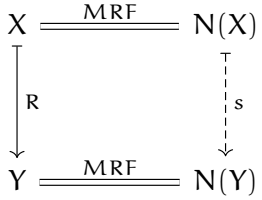

Figure 3.3: Reconstruction of material structures. X is the sample material structure and Y is the reconstruction of X. $N(X)$ and $N(Y)$ represent the ordered set of neighborhoods from the MRF model of X and Y, respectively. Material structure Y is reconstructed by sampling from $N(X)$ through algorithm s.

will also assume that the elements in $X_N(t)$ are ordered lexicographically. We acknowledge that the neighborhoods may take shapes other than a square depending on sample heterogeneous material. With the Markov assumption, the probability of X_t depends on and only on $X_N(t)$. Therefore, the heterogeneous material can be described completely by the joint probability distribution within the neighborhood window when the stationarity of sample heterogeneous can be safely assumed. The major advantage of the MRF is that it models a global material structure by specifying local properties of neighborhoods.

When modeled by MRF, we say Y is equivalent to X if and only if Y and X share the same set of neighborhoods. The concept of reconstruction is summarized in Figure 3.3, where $N(X)$ and $N(Y)$ represent the ordered set of neighborhoods from the MRF model of X and Y, respectively. Material structure Y is reconstructed by sampling the MRF model of X. The successfulness of reconstruction hinges on the capability to sampling algorithm s.

Due to the complexity of direct sampling the joint probability distribution modeled by MRF, different ways have been proposed to approximate the joint probability indirectly. Feature-based algorithms have long been used to sample MRF by matching the statistics of a common set of underlying features. For example, Heeger and Bergen [43] sample the MRF by matching marginal histograms of steerable pyramids. Cang and Ren [20] extend this approach by replacing the histogram with a deep network learning model. Even though their method significantly improves the quality of sampling, the algorithm still tends to lose local geometric details of the sample

heterogeneous material. This is a common drawback shared by feature-based approaches since only limited information (usually lower order statistics) can be captured by a finite set of features.

Gibbs sampling has also been used to approximate the joint probabilities with conditional probabilities [179, 16]. Consistent estimation of joint probabilities is usually generated by Gibbs sampling for stationary MRF. However, the iterative approach is computationally expensive: even a small sample of material structures may take days to generate.

Wei and Levoy proposed the first non-parametric sampling algorithmic for MRF. Wei - Levoy algorithm is summarized as follows:

1. Select a random start value s, let $Y_0 = X_s$.

2. Suppose next site needing to be synthesized in raster (lexicographic) order is n. let

$$d_0 = \min_t d_N \left(X_{N^*(t)}, Y_{N^*(n)} \right)$$

   where $d_N \left(X_{N^*(t)}, Y_{N^*(n)} \right) = \| X_{N^*(t)} - Y_{N^*(n)} \|$ calculates the site-wise difference between available neighborhood and $N^*(n) = \{ s : s \in N(n), Y_s \neq \emptyset \}$ denotes the subset of the neighborhood where the value of Y has already been assigned.

3. Choose t randomly from

$$\left\{ t : d_N \left(X_{N^*(t)}, Y_{N^*(n)} \right) \leqslant (1 + \epsilon)\, d_0 \right\},$$

   Set $Y_n = X_t$.

Inspired by Wei - Levoy algorithm, numerous sampling algorithms in the field of texture synthesis have been proposed to increase the speed of the algorithm and to enhance the quality of synthesis results. For example, Wei and Levoy implemented the tree-structured vector quantization (TSVQ) to reduce the linear dimension of the neighborhood. Other notable dimension reduction

methods include using a subset of the neighborhood [74] and Principal Component Analysis (PCA) [73]. More recent acceleration schemes include PatchMatch [3], Image melding [29], and PatchTable [4], whose core idea is to perform an approximate nearest neighborhood (ANN) search over $N(X)$. However, the reduction of information from neighborhoods inevitably decreases the quality of synthesis results. An alternative approach is to reduce the number of neighborhoods to search from in every synthesis step. The most effective methods are based on the notion of coherence. First introduced by Ashikhmin [2] to avoid the computationally expensive exhaustive search, the method has been extended to k-coherence in [155] which requires the preprocessing of input sample structure. The supervised learning method proposed by Bostanabad *et al.* can be seen as the combination of the two approaches as the learning model creates the classification tree while automatically reduce the dimension of the neighborhood. In our implementation, we refrain ourselves from some of the speedup techniques since such techniques inevitable limit the neighborhoods to select from. Therefore the modified algorithm may no longer share the important properties of the original algorithm we discussed in the next section.

3.2 Material structure reconstruction by Wei - Levoy algorithm

Whereas texture synthesis focuses on generating visually pleasant images, modeling the heterogeneous material requires preservation of material descriptors and properties during the modeling and sampling process. Hence, in order to utilize Wei - Levoy algorithm as a sampling method for material MRF model, we must first answer the fundamental question: *which, if any, material descriptors are preserved by Wei - Levoy algorithm?* The answer to this question determines whether it is reasonable to expect the equvilence between the sampled material and the original material sample. We now show that the answer to this question is affirmative, not only when n-point correlation functions are chosen as material descriptors, but also a larger set of material descriptors including Minkowski functionals, line path function, nearest neighbor function, and other reasonably

well-behaved properties of the material structure.

Intuitively, the method holds the property that the spatial neighborhood of each site is similar to at least one neighborhood from the sample heterogeneous material. More formally, consider a quarter of the neighborhood window $Q_t = [t - \omega + 1, t]^d$, in which the space of all possible configurations is $\Omega = 2^{w^d}$. Denote the corresponding vector of values on sampling result lattice sites as $\mathbf{Q}_t = Y_{Q_t}$. Let $F_{\mathbf{Q}}$ be the cumulative distribution function of lattice sites' values over all possible ω^n neighborhood in the original sample X. The cumulative distribution function of $\mathbf{Q}_t$ is defined as

$$F_{\mathbf{Q}_t}(\mathbf{q}) = P(\mathbf{Q}_t \leqslant \mathbf{q})$$

Levina and Bickel [76] proved that for all $t \in \mathbb{Z}^n$:

$$\sup_{\mathbf{q}\in\Omega} |F_{\mathbf{Q}_t}(\mathbf{q}) - F_{\mathbf{Q}}(\mathbf{q})| \to 0 \quad a.s. \quad as \quad T \to \infty \tag{3.3}$$

under technical assumptions which include strict stationarity, short range dependence, and mild regularity conditions. The proof in [76] assumes $d = 2$, but it extends to $d = 3$ in a straightforward manner. This result implies that, in most reasonable situations, the Wei - Levoy algorithm provides consistent estimates of the joint distribution in a predefined neighborhood window.

Based on the proof of Levina and Bickel, we may postulate that Wei - Levoy algorithm also consistently estimates all material descriptors and material properties inside such neighborhood window:

$$\sup_{\mathbf{q}\in\Omega} |F_{\mathbf{D}_t}(D(\mathbf{q})) - F_{\mathbf{D}}(D(\mathbf{q}))| \to 0 \quad a.s. \quad as \quad T \to \infty \tag{3.4}$$

This formal statement is obtained by a syntactic substitution in Equation 3.3 , where the random local configuration $\mathbf{Q}$ of material structure is replaced by a function $D(\mathbf{Q})$ of $\mathbf{Q}$. Thus, if $\mathbf{Q}_{(t)}$ is the local configurations from sampling result (input material structure), then $\mathbf{D}_t \equiv D(\mathbf{Q}_{(t)})$, Ω is the space of all possible configurations in a quarter of the neighborhood window. With an order

properly defined, $F_{\mathbf{D}_{(t)}} = P(\mathbf{D}_{(t)} \leqslant \mathbf{d})$ is the cumulative distribution function of $\mathbf{D}_{(t)}$, T is the size of input sample. Informally, a sampling method that preserves (in the limit) the joint distribution of random variables of material structure in a neighborhood will also preserve (in the limit) any reasonable function of the material structure in that neighborhood.

In particular, the n-point correlation functions $S_n(\mathbf{q})$, Minkowski functionals $W_\alpha(\mathbf{q})$ and the stiffness tensor of the material structure are instances of such function that are consistently estimated by Wei - Levoy algorithm within any neighborhood window. Notice that this implies consistent estimation of the expectation of Minkowski functionals, as well as of Minkowski functionals densities:

$$\| \frac{W_\alpha(X)}{V(X)} - \frac{W_\alpha(Y)}{V(Y)} \| \to 0 \quad a.s. \quad as \quad T \to \infty \tag{3.5}$$

where V is the macroscopic volume of material structure. The same argument extends to other commonly used material descriptors, such as line path function, nearest neighbor function as well as physical properties that are integrals of functions over material structure. The experimental validations are shown in the following two sections.

3.3 Parallelable algorithm for implicit representation

Wei - Levoy algorithm samples the MRF models of heterogeneous material persevering the material descriptors and material properties of the sample material. However, as a serial algorithm that samples the sites following a space filling curve, it suffers drawbacks such as the using of causal neighborhoods and sensitive to the sampling order. In particular, the Wei - Levoy algorithm is not parallelable and answering point membership queries requires the evaluation of the whole sampling domain. These drawbacks make Wei - Levoy algorithm unsuitable for the modeling heterogeneous material and the integration into the existing CAD system. In addition, large neighborhoods may be required for heterogeneous materials with long range correlations (see Chapter 3.4).

To address these drawbacks and make the algorithm parallelable, our implementation of the

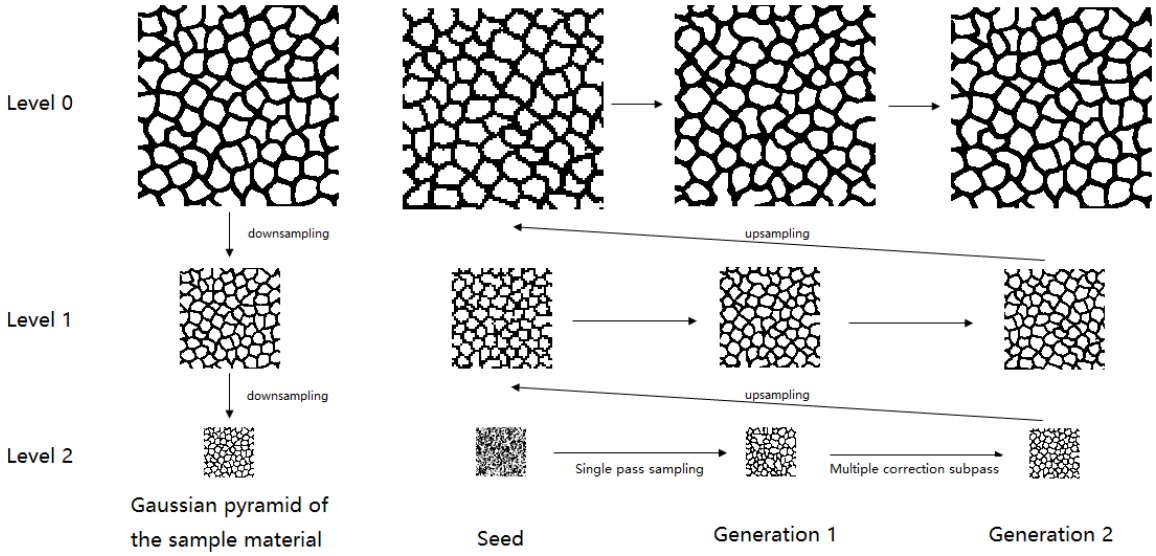

Figure 3.4: Parallelable sampling algorithm with Gaussian pyramid and correction subpasses.

algorithm engages Gaussian pyramid and correction subpasses (Figure 6.5), similar to the implementation in [167, 73]. Gaussian pyramid is a stack of series of images which are smoothed (blurred) by a Gaussian kernel and then down-sampled. After finishing the sampling at the lower resolution, the result will be up-sampled to be the template of sampling at the higher resolution. The sampling will be determined by sites sampled at the lower resolution. The benefit of using Gaussian Pyramid is twofold: firstly, it alleviates the computational burden without jeopardizing the actual size of the neighborhood by using a much smaller window size for comparison at different levels of resolution. Secondly, lower level Gaussian Pyramid can be seen as a good initial guess to guide the sampling and therefore eliminate the dependency on sampling order. In this process, closer sites gain more weight than sites further apart. We shall see that use of Gaussian Pyramid does not affect the consistency of estimation (of the joint probability distribution or of dependent material descriptors and properties), because the Gaussian kernel, which emphasizes the impact of close neighbors, is also incorporated in Levina and Bickel's proof [76].

Since the material structures are sampled basing on the neighborhoods up-sampled from a lower level of the image pyramid, the sampled material does not accurately represent the material

modeled by MRF at the current level of the MRF. Additional passes of sampling are required by using the neighborhoods from the current level of resolution. However, if we re-sample all the sites concurrently, the neighbors a site conditionally depends on are also updating, leading to slow convergence or even cyclic changes. To address this issue, we perform multiple resampling subpasses where only one site within a neighborhood is resampled in a single subpass.

3.4 Optimal neighborhood size

We ran the Wei - Levoy algorithm on six different material structure samples with different neighborhood size, from 5×5 to 15×15 (Table 3.1). These experiments serve the dual purpose: to confirm that the Wei - Levoy algorithm in fact preserves the correlation functions and to study the effect of neighborhood size on the quality of sampling. To reduce the sampling errors, 11 more samples are generated in addition to the ones in Table 3.1. For each sample, the relative errors (averaged from 12 independent samples) of two-point correlation function at different window size are plotted in Figure 3.5 (Refer Section 3.5 for more details). It is clear that the choice of neighborhood window size impacts the quality of sampling, which immediately raises the question: what is the optimal window size?

Even though MRF-based texture synthesis has been an active research area for more than a decade, there is not a consensus on a systematic approach to choosing the size of the neighborhood window [76]. It is generally believed that structured textures require a larger window. And it is not difficult to observe that a smaller neighborhood window tends to create more randomness on a structured input. In this section, we propose a rational procedure for choosing a smallest window size that is likely to preserve many widely used material descriptors. Our arguments are supported both theoretically and experimentally.

Informally, thinking of material structure as a spatial signal, the window should be large enough to cover the lowest frequency that affects the chosen material descriptor. Put another way, the very

Table 3.1: Material microstructure and their reconstruction with different window size.

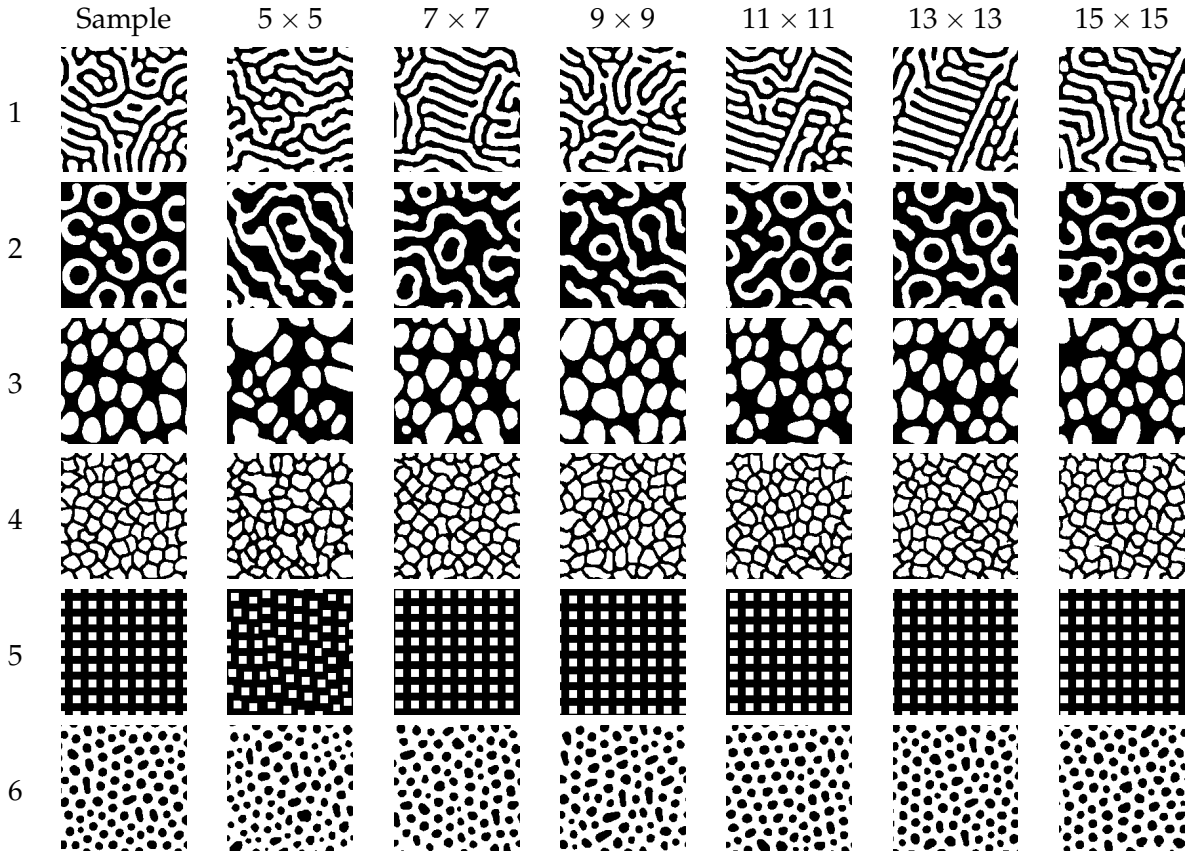

formulation of the material modeling problem rests on the assumption of stationarity: the material samples must remain in the same material class as the reference location moves throughout the sample. This implies that the window of optimal size should be large enough to capture meaningful material structure, but not larger than that. Below, we propose a method to determine an optimal window size based on the commonly assumed grain-germ model of material structure.

3.4.1 Grain-germ characterization of two-point correlation function

Recall that geometry of material structure may be conveniently conceptualized in terms of the usual grain-germ model discussed in Chapter 2. Grains refer to particles, fibers, Voronoi cells, truss

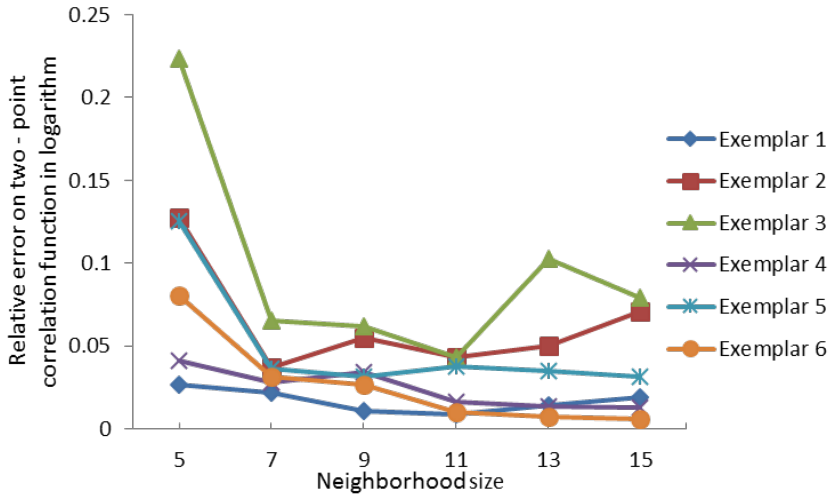

Figure 3.5: Relative errors on two–point correlation functions of reconstructions with different neighborhood sizes. Each sampling point in the graph is averaged from 12 reconstruction results to reduce sampling errors.

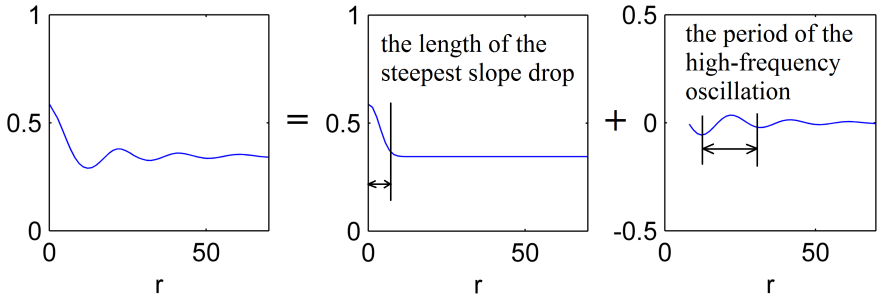

Figure 3.6: The period of the high-frequency oscillation and the length of the steepest slope drop in the correlation function.

units, pores, beams, plates, and other compact sets modeling basic repeating material elements in a material structure, while germs refer to their distribution (locations) within the material structure. Thus bone may be conceptualized as a spatial distribution of beam and plate elements [154], and metal foams may be viewed as a random allocation of truss cells positions on a randomly generated Voronoi diagram [38].

With this conceptualization, the lower order correlation functions measure the lower frequencies in material structure: the size of grains and distribution of germs, while the higher order correlation

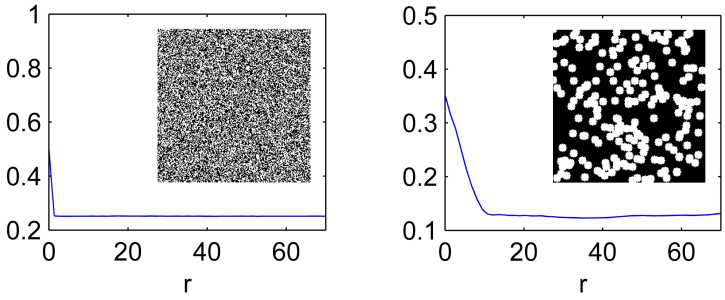

Figure 3.7: Two-point correlation functions of images of random noises, the left image has the pixels as grains while the right image has circular grains with diameter equal to 10 pixels. The left one yields a length of steepest drop of 1 pixel and the right one gives this length about 10 pixels.

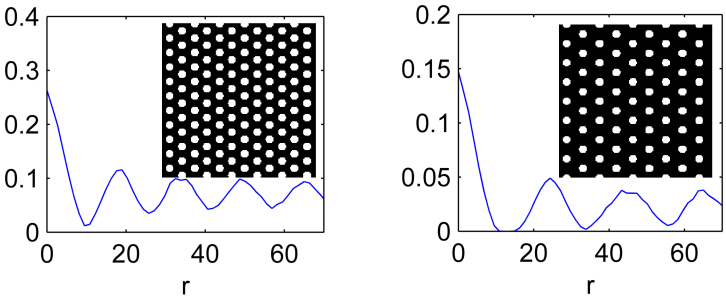

Figure 3.8: Two-point correlation functions of images of two regular patterns, both images has circular grains with diameter equal to 10 pixels. The distance between the germs in the left image is 18 pixels while the one in the right image is 24 pixels. It shows that the period of high-frequency oscillations correspond to the distance between the germs in the material structure.

functions are more sensitive to (high-frequency changes in) the shape of grains [148]. Since lower frequencies usually have longer correlation ranges, we will choose the window size based on two-point correlation function. If we ignore the high-frequency oscillations, a change in slope is observable as the correlation range increases (Figure 3.6). Hence we make our first assumption:

> *The length of the steepest drop in slope (measured along the distance axis) of the two-point correlation function measures the size of the grain.*

To be more precise, this length measures roughly the diameter of the grain.

If we subtract this low-frequency component from original two-point correlation function, we get a damped periodic function with decreasing amplitude whose period indicates the most frequent distance to the nearest neighbor grains (not to be confused with neighbors of image representation). The sharp wave crests and troughs (local maximum and minimum) suggest that the nearest neighbors locate at relatively uniform distances. In other words, we can also assume that:

> *The period of high-frequency oscillations in the two-point correlation function roughly measures the distance between the germs in the material structure.*

The decrease in amplitude is the result of more incorporated germs turning relatively uniform distances into uniformly distributed distances with growing correlation range. To further explain the concept, Figure 3.7 shows two images of random noises. Since the germs are randomly generated in both images, the corresponding two-point correlation functions do not exhibit high frequency oscillations after the steepest drops. Figure 3.8 shows two images with different inter-grain distances that are consistently estimated by the corresponding periods of high-frequency oscillations in the respective two-point correlation functions.

3.4.2 Optimal window size from estimated two-point correlation function

Based on the above assumptions, we conjecture that a minimally required size of neighborhood window (with respect to the assumed grain-germ model) is implied by the properties of the material sample's two-point correlation function:

> *the period of the high-frequency oscillation plus the length of the steepest slope drop in the correlation function.*

Mathematically, we propose a new analytic expression for two-point correlation function,

$$S_2(r) = C_2(r) + W(r)$$

Table 3.2: Fitting parameters of Corson's formula and damped periodic function.

Sample	ϕ	c	n	A	λ	θ	h	l_1	l_2	$l_1 + l_2$	s
1	0.5872	0.0316	2.2042	-0.1035	0.0481	-0.3222	-0.6158	7.0029	19.5001	26.503	7
2	0.3927	0.0175	2.077	0.0666	0.026	0.2039	0.8981	10.4699	30.8113	41.2813	11
3	0.5233	0.0227	1.8518	0.1272	0.0518	0.1322	1.2015	12.1164	47.5279	59.6443	15
4	0.6118	0.0617	1.9775	-0.0505	0.041	0.2741	-2.0109	6.2345	22.9191	29.1536	9
5	0.25	0.0346	2.0964	0.0419	0.011	0.2572	0.9925	7.4107	24.4309	31.8416	9
6	0.67	0.0308	2.1903	0.1147	0.0514	0.3092	0.6781	7.1729	20.3177	27.4905	7

which combines Corson's formula [26]:

$$C_2(r) = \phi^2 + \phi(1-\phi)e^{-cr^n} \tag{3.6}$$

and damped wave function:

$$W(r) = Ae^{-\lambda r}\cos(\theta r + h) \tag{3.7}$$

In Corson's formula (Equation 3.6), ϕ is volume fraction, c and n are empirical constants and can be determined by a least square curve fit. This formulation satisfies the constraints on two-point correlation function: $C_2(0) = \phi$ and $C_2(\infty) = \phi^2$. Corson's formula has been shown to be appropriate for random material structure [126], however, it does not account for the high frequency oscillation after the steepest drop. This difference can be modeled by a damped wave function since the oscillation fades out due to the average effect at long correlation range. In damped wave function (Equation 3.7), A, λ, ω and h are maximum amplitude, decay constant, frequency and phase of the wave that can be determined by least square curve fit as well.

The curve fitting is done in two steps: first, Corson's formula is fitted onto two-point correlation function to obtain $C_2(r)$. As shown in Figure 3.6, this fitting will screen out the oscillations from the structured part (grains) of the material structure. Then, the oscillatory component of the two-point correlation function is obtained by subtracting the fitted Corson's function from the original correlation function as $W(r) = S_2(r) - C_2(r)$ and is fitted by damped periodic function (Figure 3.9).

A parameterization of two-point correlation functions that account for the oscillatory behavior

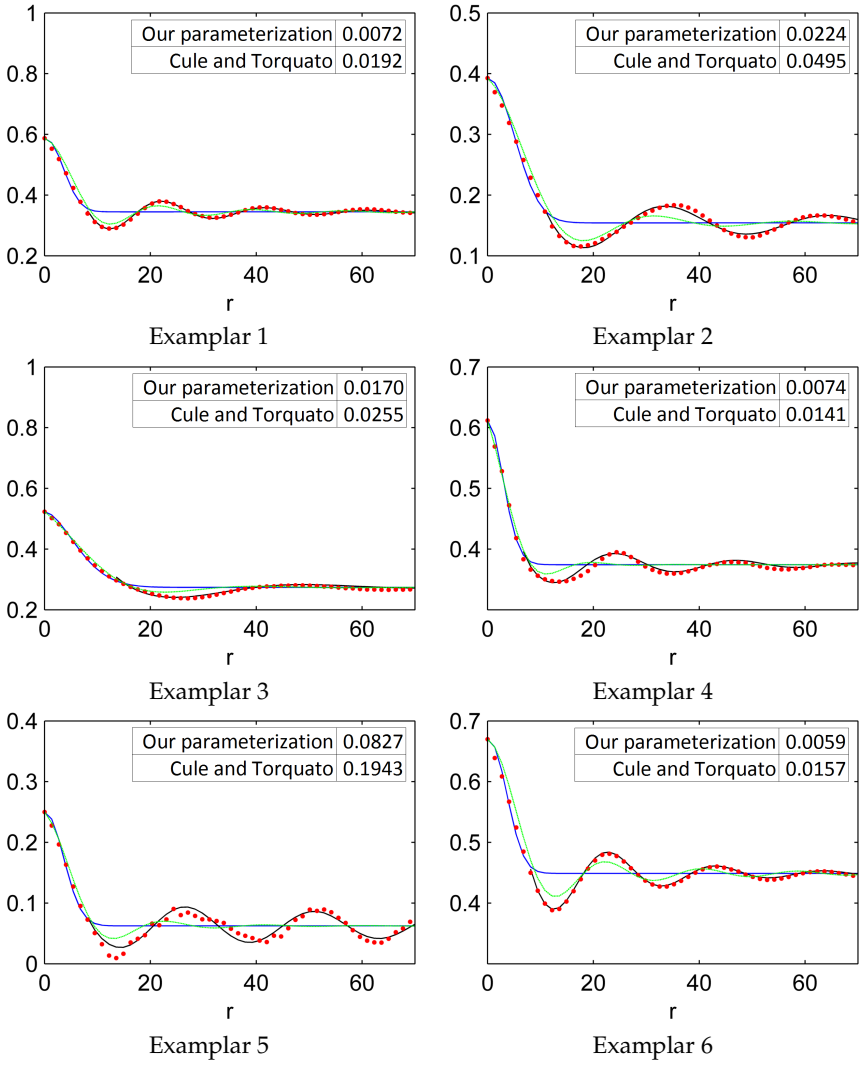

Figure 3.9: Parameterization of two-point correlation functions. The red dots are the sampled two-point correlation functions, blue solid lines plot fitted $C_2(r)$ and the black solid lines are fitted $W(r)$, green dashed lines are fitting results of [28]. The relative errors of our parameterization and method in [28] are shown on the corner of each plot.

has also been proposed in [28]. Our parameterization not only fits all six correlation functions better, but it also accounts for the two different length scales: the length of the steepest slope drop and the period of the high-frequency oscillation. Rewriting $C_2(r) = \phi^2 + a(\phi - \phi^2)$, we see that parameter a gives a rough estimate of the drop in value of $C_2(r)$ as a function of distance r. In fact,

from Equation 3.6, we can then estimate the value l_1 of r corresponding to any particular fraction a as

$$l_1 = \sqrt[n]{-\frac{\ln(a)}{c}}.$$

For example, setting $a = 0.1$ corresponds to an empirical observation that the length of the steepest slope drop is roughly 10% of the difference $(\phi - \phi^2)$ between long range and short range values of $C_2(r)$. It is also easy to see that the period of the high-frequency oscillation:

$$l_2 = \frac{2\pi}{\theta}.$$

Based on the above observations, the neighborhood window size $2\omega + 1$ should be no smaller than $l_1 + l_2$. Fitting parameters of Corson's formula and damped periodic function for all sample materials are reported in Table 3.2 and the optimal window size $2\omega + 1$ is determined based on a three-level Gaussian pyramid (see next section) implementation and calculated by the next odd number larger than $(l_1 + l_2)/4$.

We also observed that the error in correlation function may also increase when the window size is increased beyond minimally required one, for example, in the sampling results for input material sample 1 and 2. The most likely explanation for this behavior is that these input material samples are not truly homogeneous and the assumption of stationarity does not hold. In this case, a larger neighborhood window will suppress the non-homogeneous regions of the input material structure.

Table 3.3: Relative errors of reconstructed material structures in Table 3.1 at optimal window size.

	Correlation functions				Minkowski functionals densities	
Sample	1st order	2nd order	3rd order	4th order	Perimeter (mm^{-1})	Euler characteristic (mm^{-2})
1	0.96%	2.05%	2.5%	1.48%	3.24%	23.89%
2	0.95%	4.18%	6.7%	11.35%	0.6%	5.88%
3	4.07%	7.79%	9.15%	15.99%	9.38%	13.98%
4	1.25%	2.58%	2.95%	4.90%	0.08%	0.35%
5	0%	4.07%	5.4%	2.76%	0%	0%
6	1%	2.05%	0.91%	1.12%	4.12%	7.06%

3.5 Reconstructions of 2D heterogeneous materials

To compare the correlation functions of the sampled material structures to the input heterogeneous material, we measured the relative error computed in L_2 norm:

$$\frac{\|S_n(Y) - S_n(X)\|_2}{\|S_n(X)\|_2}$$

Though the definition of correlation functions is straightforward, the computation of such functions is not a trivial task. As mentioned in Chapter 2, even with the assumption on stationarity and isotropy, an n-point correlation function needs $\binom{n}{2}$ pairwise distance to fully specify, and direct estimation of n–point correlation function is $O(N^n)$ for N sites. Clearly, brute-force estimation of higher order correlation functions is impractical. We implemented an FFT-based method [148] to compute two-point correlation functions in MATLAB. Third and higher order correlation functions are estimated using software packages relying on KD-trees [91]. We emphasize that these correlation functions are compared at a much longer range than the optimal neighborhood window size, with the longest pairwise distance equal to 150, 100 and 60 pixels for two-point, three-point and four-point correlation functions, respectively.

Table 3.3 shows the relative errors in correlation functions and Minkowski functionals between the original sample and reconstructed material structures using optimal neighborhood window size. The results indicate a good agreement in first four orders of correlation functions for reconstructed

Table 3.4: Relative errors on Minkowski functionals densities of the reconstructed material structures for all neighborhood window sizes. Each error in the table is averaged from 12 reconstruction results to reduce sampling error.

	5×5			7×7			9×9		
Sample	Perimeter	Area	Euler	Perimeter	Area	Euler	Perimeter	Area	Euler
1	6.98%	1.49%	60.47%	**4.18**%	**0.77**%	**25.21**%	3.06%	0.62%	26.28%
2	4.54%	6.26%	40.69%	2.16%	1.63%	58.33%	2.33%	3.55%	50.98%
3	9.46%	13.56%	9.68%	11.33%	7.98%	12.90%	6.20%	4.99%	10.75%
4	8.69%	2.96%	7.21%	2.23%	1.91%	3.63%	**0.83%**	**2.08%**	**3.87%**
5	2.11%	2.49%	2.31%	0.00%	1.06%	0.00%	**0.00%**	**0.73%**	**0.00%**
6	10.93%	10.65%	9.14%	**8.70%**	**4.71%**	**8.62%**	7.63%	4.58%	10.67%

	11×11			13×13			15×15		
Sample	Perimeter	Area	Euler	Perimeter	Area	Euler	Perimeter	Area	Euler
1	1.99%	0.91%	34.62%	1.88%	0.71%	36.11%	1.83%	0.99%	77.35%
2	**1.79%**	**2.22%**	**59.31%**	2.36%	3.54%	100.00%	2.86%	3.66%	100.98%
3	6.43%	5.00%	7.17%	8.69%	7.06%	8.78%	**8.49%**	**5.47%**	**11.29%**
4	2.24%	1.04%	4.08%	3.26%	1.24%	5.79%	4.30%	0.90%	6.32%
5	0.00%	1.23%	0.00%	0.00%	0.79%	0.00%	0.00%	0.97%	0.00%
6	9.61%	5.31%	14.21%	8.45%	5.70%	12.76%	8.05%	7.32%	13.16%

material structures with an exception for sample 3, as predicted by the theory. sample 3 does not fully satisfy the stationarity assumption due to the limited size of the input.

To estimate values of Minkwoski functionals, we used the software package developed by Legland *et al.* [75]. The error on Minkowski functionals are compared in two different ways: the cumulative frequency of Minkowski functionals estimated at optimal window size is compared in Figure 3.10; and the Minkowski functional densities (per Equation 3.5) between the input samples and reconstruction results are compared in Table 3.3. Note that the "density of area" coincides with first order correlation function and is therefore has been omitted as redundant.

The statistics of Minkowski functionals agree well between input sample and reconstruction result, except for sample 3 and Euler characteristic of sample 1. We already conjectured that the sample 3 is too small and fails the stationarity assumption. The behavior of sample 1 may be explained by the apparent lack of "grains" in the image; in this case, the parameter l_1 and l_2 are likely to be dominated by the widths of the material(black) and void(white) paths respectively in the image. The resulting window is too small because connectivity of the image within the window

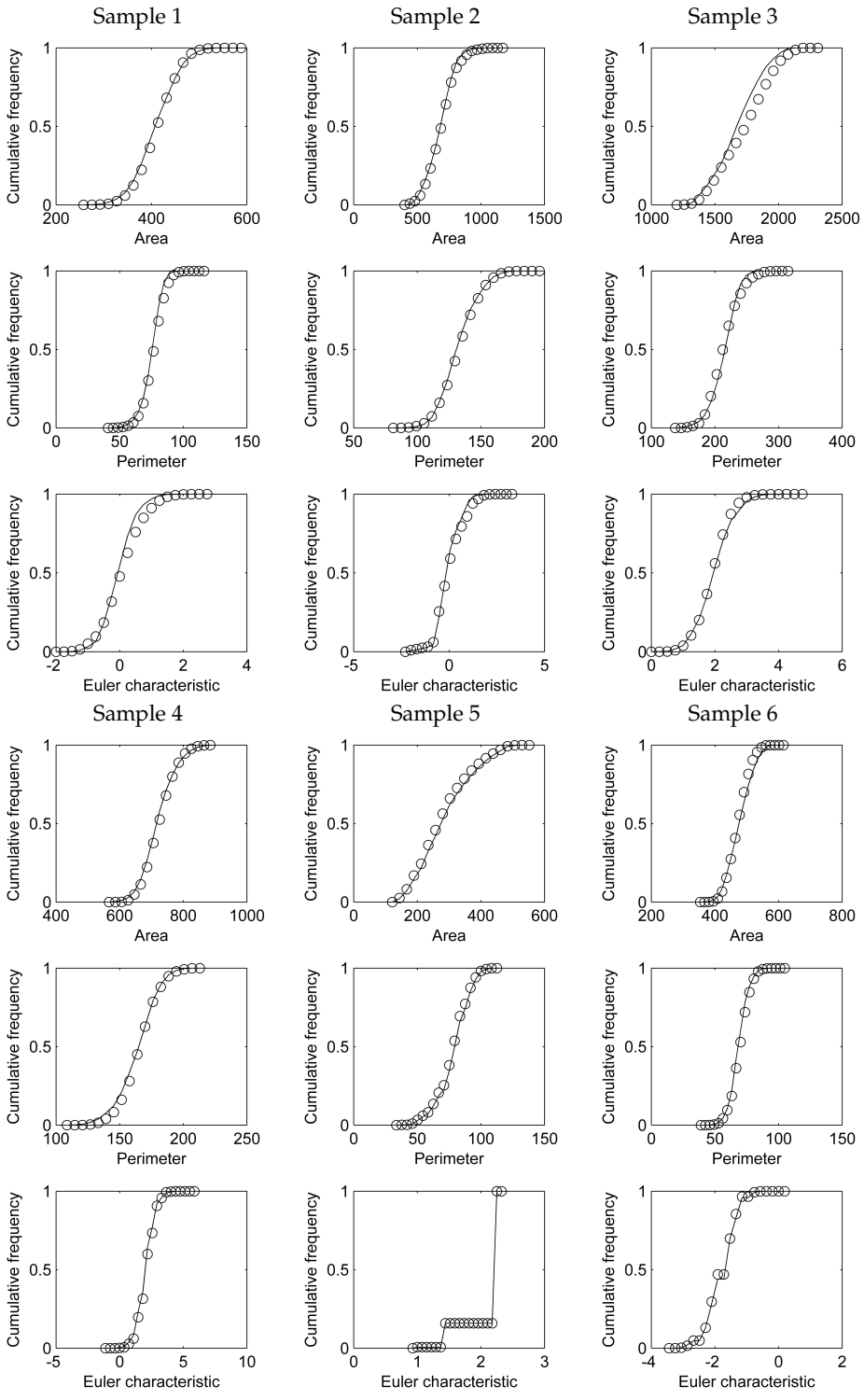

Figure 3.10: Cumulative frequency polygon of sample material and reconstruction result. The measurements from input samples are represented in solid blue line while the measurements from reconstruction results are represented in dashed black line.

Table 3.5: Timing statistics for reconstructions in different neighborhood window sizes (in seconds).

Sample	5×5	7×7	9×9	11×11	13×13	15×15
1	169.96	201.62	237.26	282.61	319.13	363.33
2	171.42	200.54	234.18	279.62	315.95	358.70
3	173.34	203.99	236.51	283.00	319.32	363.19
4	173.42	204.70	240.67	287.88	323.54	368.71
5	167.45	195.72	227.76	270.88	302.40	339.73
6	169.75	201.13	236.39	282.60	318.48	365.10

will vary widely under small perturbations. Table 3.5 shows timing statistics for reconstructions in different neighborhood window sizes.

To verify the effectiveness of our method for selecting the optimal neighborhood window size, we computed the relative errors in Minkowski functionals between the sample and reconstructed material structures at different window sizes. These are shown in Table 3.4. The relative errors for the selected neighborhood window size are shown in bold. The results suggest that in all cases the selected window sizes are either optimal or nearly optimal. A notable exception is the behavior of the Euler characteristics for samples 1 to 3. Because the Euler characteristic is quite small in all samples, even mildest violations of the stationarity conditions can lead to large relative errors in the reconstructed results. This phenomenon is exhibited clearly for sample 2, where the Euler characteristic is 4, but even the reconstruction with largest window size does not capture the topology of the sample, which is not stationary. By contrast, the sample 5 is stationary, and its topology measures (including the Euler characteristic value of 64) are properly accounted for.

To further demonstrate the effectiveness of the proposed method, we compare the effective stiffness between the sample material structures and the reconstructed ones with the smallest errors on Minkowski functionals densities in Table 3.6. Their relative difference in Frobenius norm is shown in the last column. The effective stiffness is calculated by the Green's function based homogenization discussed in Chapter 5.

Table 3.6: Comparison between the effective stiffness of the sample material structures C_S and the effective stiffness of reconstructed material structures C_R and their relative difference in Frobenius norm. The effective stiffness are calculated by Green's function based homogenization discussed in Chapter 5.

Sample material	C_S	Reconstruction	C_R	Relative error
	$\begin{bmatrix} 0.3920 & 0.1575 & 0.0101 \\ 0.1575 & 0.3938 & 0.0019 \\ 0.0101 & 0.0019 & 0.2380 \end{bmatrix}$		$\begin{bmatrix} 0.4059 & 0.1562 & 0.0051 \\ 0.1562 & 0.3829 & -0.0043 \\ 0.0051 & -0.0043 & 0.2415 \end{bmatrix}$	3.31 %
	$\begin{bmatrix} 0.2666 & 0.1129 & 0.0016 \\ 0.1129 & 0.2678 & 0.0005 \\ 0.0016 & 0.0005 & 0.1545 \end{bmatrix}$		$\begin{bmatrix} 0.2674 & 0.1148 & -0.0048 \\ 0.1148 & 0.2618 & 0.0004 \\ -0.0049 & 0.0004 & 0.1592 \end{bmatrix}$	2.78 %
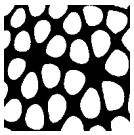	$\begin{bmatrix} 0.2981 & 0.1207 & -0.0002 \\ 0.1208 & 0.3109 & -0.0027 \\ -0.0002 & -0.0027 & 0.1843 \end{bmatrix}$	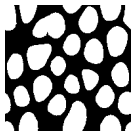	$\begin{bmatrix} 0.2808 & 0.1166 & -0.005 \\ 0.1167 & 0.3004 & -0.0022 \\ -0.005 & -0.0022 & 0.1767 \end{bmatrix}$	4.70 %
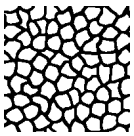	$\begin{bmatrix} 0.367 & 0.1411 & -0.0018 \\ 0.1411 & 0.3681 & 0.0008 \\ -0.0018 & 0.0008 & 0.227 \end{bmatrix}$	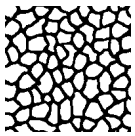	$\begin{bmatrix} 0.3582 & 0.141 & -0.0025 \\ 0.141 & 0.3638 & 0.001 \\ -0.0025 & 0.001 & 0.225 \end{bmatrix}$	1.67 %
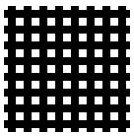	$\begin{bmatrix} 0.1952 & 0.0737 & 0 \\ 0.0737 & 0.1952 & 0 \\ 0 & 0 & 0.1044 \end{bmatrix}$	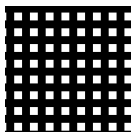	$\begin{bmatrix} 0.1952 & 0.0737 & 0 \\ 0.0737 & 0.1952 & 0 \\ 0 & 0 & 0.1044 \end{bmatrix}$	0.00 %
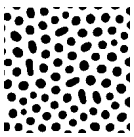	$\begin{bmatrix} 0.6210 & 0.2555 & -0.0032 \\ 0.2555 & 0.6316 & 0.0082 \\ -0.0032 & 0.0082 & 0.3738 \end{bmatrix}$	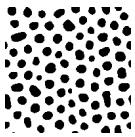	$\begin{bmatrix} 0.6358 & 0.2646 & 0.0008 \\ 0.2646 & 0.6469 & 0.0041 \\ 0.0008 & 0.0041 & 0.3857 \end{bmatrix}$	2.80 %

3.6 Reconstructions of 3D heterogeneous materials

The 3D micro-CT image measured at the pore-scale modeling research group at Imperial College London [103] served as the sample material for the reconstruction (Figure 3.11 a). The diameter of grain in sandstone is estimated to be at least 5 based on the steepest drop in the two-point correlation function, as described in Section 3.4. The flat tail of the correlation function indicates an even distribution of distances between germs, which suggests that the distance between germs in the sandstone cannot be estimated from a two-point correlation function. In this case, we pick this

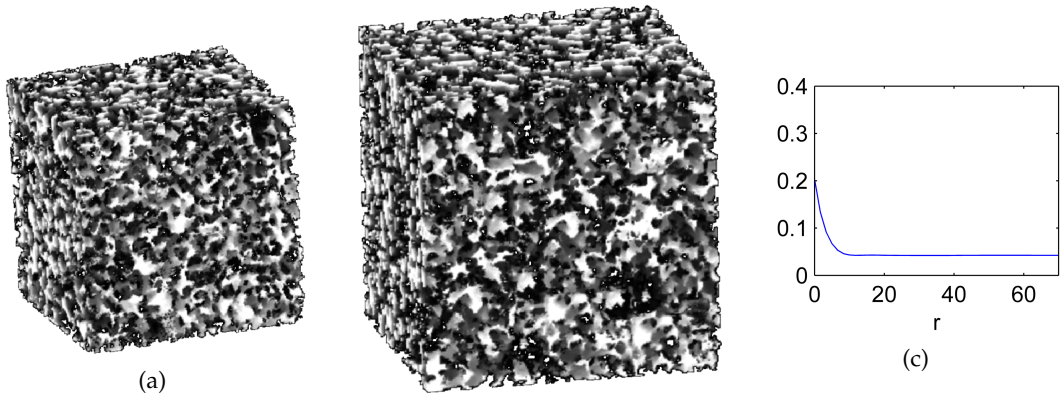

(a) (b) (c)

Figure 3.11: Reconstruction of three dimensional Berea sandstone. The sample material ($128 \times 128 \times 128$) is on the left, the reconstruction result ($154 \times 154 \times 154$) is on the right. Two-point correlation function of the Berea sandstone. The flat tail indicates an even distribution of distances between the germs.

Table 3.7: Relative errors of Berea sandstone reconstruction.

Descriptors	Relative errors
Two-point correlation function	6.31%
Volume fraction	3.26%
Density of surface area (mm^{-1})	2.23%
Density of Mean width(mm^{-2})	1.71%
Density of Euler characteristic(mm^{-3})	1.04%

distance manually to be 25, five times of the diameter of the grain, a distance that is expected to cover most of the neighboring grains. Figure 3.11 (b) shows the reconstruction of the sandstone sample (a) using $30 \times 30 \times 30$ window size. The relative errors in Table 3.7 suggest good agreement in Minkowski functionals and two-point correlation function with the sample. The reconstruction takes about 2.5 hours on an Intel Core i7 3.4GHz CPU computer with 16 gigabytes memory.

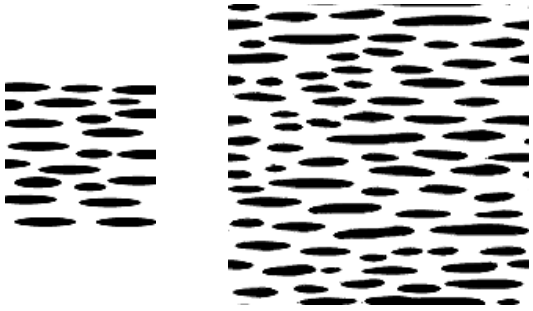

Figure 3.12: Reconstruction of an anisotropic material with neighborhood window size 5×9 on a three–level Gaussian pyramid.

3.7 Reconstructions of anisotropic and multiphase materials

3.7.1 Reconstruction of anisotropic materials

As explained in Chapter 2, the two-point correlation function is able to represent material anisotropy in principle; however, in practice, isotropy is usually assumed so that two-point correlation function becomes a function of a single parameter, distance. Additional non-trivial computations are required to incorporate the directional parameters into the two-point correlation function. The same MRF model and sampling procedure reconstructs anisotropic material without extra cost. If the material structure is strongly anisotropic, we can also adapt the shape of the neighborhood window to capture the anisotropy as shown in Figure 3.12.

3.7.2 Reconstruction of multiphase materials

It is worth noting that material structure sample images are usually acquired from microscopy, μCT and MRI in a form of gray–scale images. The gray value represents the variation inside material sample, which usually carries much more information than its binary counterpart. The optimization-based material reconstruction, requires the grayscale images to be thresholded before sampling two–point correlation function, resulting in significant loss of information in the sample and in the reconstructed material structure. The MRF and sampling algorithm extends to grayscale

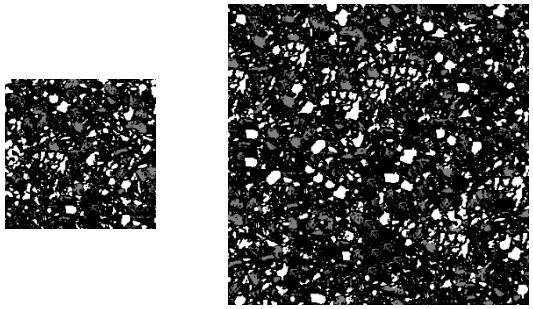

Figure 3.13: Reconstruction of a three-phase material.

image directly. Materials with more than two phases can also be represented by grayscale model and be reconstructed through the proposed method accordingly (Figure 3.13).

3.7.3 Composition of lower-dimensional models

When the acquisition of three dimensional images becomes prohibitive, two dimensional images can be acquired by optical microscope, scanning electron microscope (SEM) and transmission electron microscopy (TEM). Three dimensional information can be often extrapolated from two dimensional images [152]. A useful extension of proposed material structure modeling method allows to compose material structure models from different sources. The original idea is proposed in [164]. Instead of matching full neighborhood at full dimension, cross-sections of full neighborhoods are matched to three orthogonal views – that may come from the same material or from different materials (Figure 3.14). Reconstruction in each cross-sections will inherit the material properties from that section. The final value of a three-dimensional material structure is a composition (for example, average or maximum) of the three two-dimensional values. This technique may be used to construct a 3D material structure from a 2D sample.

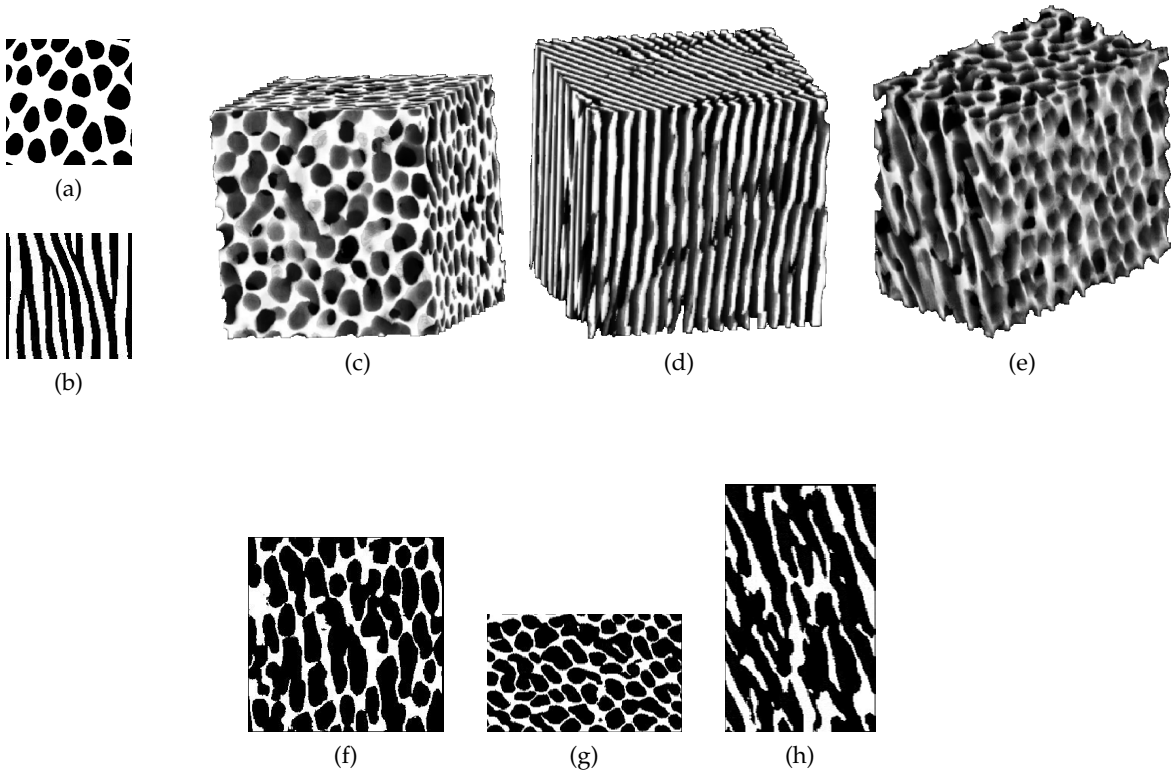

Figure 3.14: 3D material structures reconstructed from 2D samples. (c) and (d) are reconstructions from single inputs (a) and (b), respectively. (e) is a material structure reconstructed from multiple 2D samples, (a) for top and front view and (b) for left view. (f-h) are the 78th, 128th and 128th sections from top, front and side, respectively.

3.8 Discussion

The main advantage of the MRF approach to stationary material structure modeling is that, with a proper choice of neighborhood window, it automatically preserves all correlation functions, as well as other material descriptors and stiffness of materials, with nominal computational effort. The proposed algorithm accomplishes this task efficiently and does not require explicit representation or computation of material descriptors. The computational cost is non-trivial but is manageable and scales linearly with the size of neighborhood and the size of the reconstructed material structure.

We rely on the grain-germ model of materials to develop a novel approach for choosing the

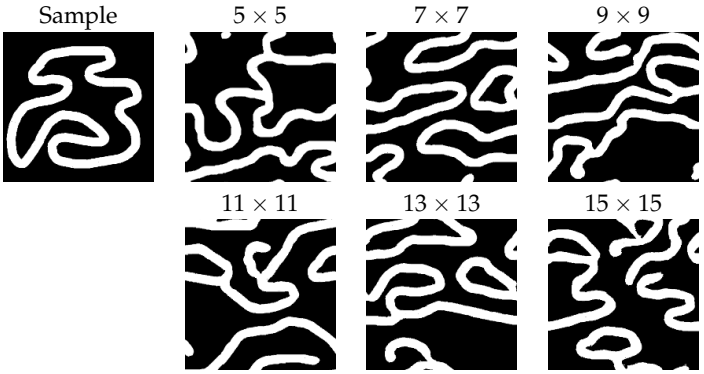

Figure 3.15: Reconstruction of a Jordan curve with different window size.

optimal size of neighborhood window and demonstrated experimentally that, with properly chosen neighborhood size, the second and higher order correlation function are preserved both inside and outside the neighborhood window. The proposed approach is validated by the empirical studies using synthetic samples in Table 1, as well as reconstruction using real materials (for example, see Figure 3.1 and Figure 3.11). We also demonstrated several extensions of the method to reconstruct material anisotropy, grayscale models, and combined lower-dimensional models.

The reconstructions of stationary material structures with such paradigm leads to a number of advantages over the traditional optimization-based approaches. These include improved computational efficiency, preservation of many material descriptors, including correlation functions and Minkowski functionals, the ability to reconstruct anisotropic materials, and direct use of the grayscale material images and two-dimensional cross-sections.

On the other hand, the proposed method is "data-driven" and cannot accept an experimentally determined or specified correlation function as the target input. The cost of the algorithm for reconstruction of material structure with long-range correlation function becomes prohibitive. Both the power and the limitations of the approach are based on assumptions of locality and stationarity of the material structure.

The method cannot be used when these assumptions do not hold. For example, consider reconstructions of the sample in the Figure 3.15. While all reconstructed structures appear similar

to the sample, none of them are able to reconstruct the essential topological property of the Jordan curve. This is not surprising because this condition does *not* satisfy the stationarity assumption. It is also easy to show that correlation functions are not sensitive to topological changes in material structure. The assumption on the stationarity will be relaxed to enable the reconstruction and design the functionally graded material structures in the next chapter.

Chapter 4

Functionally graded material structure design by material descriptors

Functionally graded materials (FGMs) are heterogeneous materials made of two or more constituent phases with properties changing gradually with position [12]. The spatial variation (gradation) of properties is determined by changes in the geometric configuration of the constituent phases that serve particular mechanical (or more generally, physical) function. FGMs are ubiquitous in nature due to their abilities to satisfy multifold functional constraints and adapt to conflicting requirements; this also explains why FGMs are a popular candidate as engineering materials. FGMs may be found in a broad spectrum of applications, including filters [87], wear resistant coatings [124], bone and dental implants [180, 98, 153], and cutting tools [13, 54]. Teeth [180], bones [98] and bamboos [137, 110] are a few examples of FGM in nature.

Traditionally, the modeling of FGM focuses on the level of macroscopic properties [115, 138, 13]. However, it is the underlying spatial variation of material structures that create and control the spatially varying properties. Recent advances in additive manufacturing [12, 112, 161, 32] and exponentially growing computing power enables the shift of engineering design from the classic material selection paradigm into a simultaneous design of material composition and structure

[132, 25]. Systematic modeling and design of graded structures with desired mechanical properties is a key ingredient of this paradigm shift.

In this chapter, we study the synthesis of two-phase functionally graded structures, such as porous structures, from a reference material sample. The challenge lies in the integration of the two scales. To circumvent the expensive solution of boundary value problem, we propose to represent and control material properties of FGM at the macroscale using the notion of material descriptors which include common geometric, statistical, and topological measures, such as volume fraction, correlation functions and Minkowski functionals. At the microscale, the material structures are modeled as Markov random fields: we formulate the problem of design and (re) construction of the FGM structure as a process of selecting neighborhoods from a reference FGM, based on target material descriptors fields. Such formulation results in two different ways to modify the sampling process: use the difference in material descriptors between neighborhoods and target descriptor fields as a penalty term in the neighborhood selection process or use the difference as a filter to remove neighborhoods without the target material descriptors. The former is favorable in computer graphics application while the latter has a clearer meaning of the design space which is the intersection of design space defined by the MRF and by the material properties. The design space defined by the material descriptors includes all material structures shares the same macroscopic material property distribution. We compare the two approaches and find that due to the intersection, the latter approach may not have a non-empty design space to sample from. A hybrid approach is therefore proposed by adding a tolerance to the target descriptor fields and using the weighted sum of differences to select the neighborhoods. The hybrid approach not only increase the efficiency of the sampling algorithm but also has a well defined design space. We identify the necessary conditions on the target descriptor field to be compatible with the material sample, and discuss how this condition can be verified and enforced. The effectiveness of the proposed framework (see Figure 4.3) in generating a smooth and continuously varying FGM structure with guaranteed properties is demonstrated by two examples: design of a graded bone structure and generating

functionally graded lattice structures with target volume fraction fields. Some results in this chapter has been reported in [81].

In the present study, the length scale of inhomogeneities is assumed to be much larger than the atomic scale but are statistically homogeneous at macroscopic, or some intermediate length scales. The former allows us to study the material structure with the equations of classical physics and the latter enables us to apply the effective properties of the material structures for the purpose of applications. A great variety of materials display this character, including metals, woods, bones, sandstone, ceramics, to list a few.

4.1 Construction problems in FGM modeling

The basic construction problem of material structure modeling is illustrated in a commutative diagram as shown in Figure 4.1. We are typically given a reference material structure sample $X \subset R^3$ whose effective material properties $P(X)$ can be evaluated via map h: one of many known homogenization methods. For example, effective Young's modulus can be homogenized through various homogenization theories, including the Gibson model for cellular materials [38], Voigt - Ruess bounds, Hashin - Strikman bounds [42], Green's function based method [107, 80], and power law [9] which is frequently used in SIMP-based topology optimization [8]. Note that $P(X)$ may be evaluated at any point of $p \in R^3$ whether it belongs to X or not, because homogenization h typically requires integrating and averaging of the mechanical properties in some neighborhood of p. We will denote the property evaluated at a point p as $P(p)$ when there is no ambiguity. Note that the neighborhoods for effective material property evaluation and the neighborhoods in MRF are related, but not necessarily the same. The effect of different neighborhood sizes will be discussed in more details in Chapter 6.

The target property fields $P(Y)$ can be designed by various gradation techniques (map g), such as interpolation schemes in solid modeling [13] and Solid Isotropic Material with Penalization

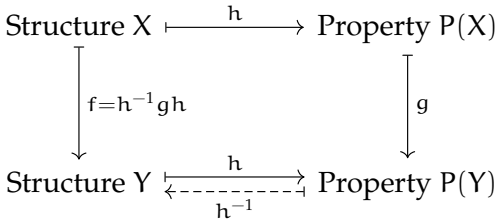

Figure 4.1: Sample-based FGM structure modeling: construct a material structure Y with material properties $P(Y)$, given a material structure X with properties $P(X)$. Map g represents various gradation techniques to design the varying properties fields.

(SIMP) [8] in topology optimization. Given the target macroscopic property distribution, the result structure Y can either be calculated from X by updating the parameters of the microscopic model or from $P(Y)$ directly through inverse homogenization [134]. It appears that the solutions to both construction problems require knowledge of the inverse homogenization map h^{-1}. Unfortunately, the relationship between the effective material properties and the corresponding material structures that produce them are known only for some periodic and cellular structures but not in general [37]. When such a relationship is not known, an iterative approach is often adopted: the structure Y is repeatedly updated and the properties $h(Y)$ evaluated until they match the target $P(Y)$. There are at least two problems with this approach. The homogenization procedure itself is a computationally expensive process that may require additional material samples and is difficult to automate. Furthermore, while the inverse homogenization approach completely disregards the input structure X, the microscopic model requires a complete understanding and parameterization of the generative process for the desired class of material structures which is not readily available for many natural and synthetic materials.

Following the discussions in Chapter 3, we propose to model the material structures via Markov random fields, with the assumption of locality of the material structure. Locality requires the constituent phase at any point depends only on the neighboring point. The range of influence of a point becomes the neighborhood of such point (see Figure 3.2). A refined version of the commutative diagram in Figure 4.1 is shown in Figure 4.2. It acknowledges explicitly that the reference material

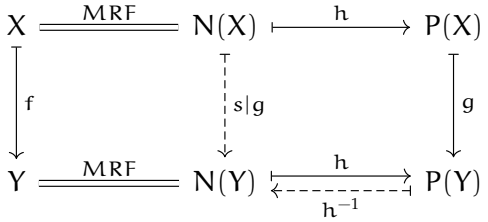

Figure 4.2: Sample - based FGM structure modeling is reformulated in terms of neighboroods N. $s|g$ represents that sampling s is conditioned by g.

structure X and the target structure Y are collections of neighborhoods $N(X)$ and $N(Y)$ respectively. A neighborhood in X about any particular point $x \in R^3$ will be denoted by $N^X(x) \equiv X_{N^3(x)}$, where $N^3(x)$ is a neighborhood of point x in R^3. The superscript is dropped for simplicity when there is no confusion. Map s mitigates f through rearranging the neighborhoods N. $s|g$ represents that sampling s is conditioned by g.

We can now restate the generic material structure construction problem more concretely in terms of neighborhoods: given a material structure X with properties $P(X)$, construct material structure Y with properties $P(Y)$, such that $\forall y \in Y$, satisfying the following two conditions:

$$\exists x \in X, \quad N(y) = N(x) \qquad \text{and} \qquad h(N(y)) = P(y) \tag{4.1}$$

The two conditions are related but not redundant. The matching of the neighborhoods simply reflects the requirement that the geometry and properties of material structure Y originates from the reference structure X. The second condition acknowledges that the approximate similarity of neighborhoods may not be sufficient to guarantee the desired target properties $P(Y)$. The conditions are not always independent, because neighborhoods with similar geometric and topological properties may indeed possess similar material properties, and it is conceivable that neighborhoods with many matching properties may indeed be very similar geometric properties. From the modeling point of view, the first condition delineates the design space as all material structures whose neighborhoods are subsets of neighborhoods of X and the second condition defines the design space

as all material structures share the same macroscopic material properties $P(Y)$. We modify the Wei-Levoy algorithm in Section 4.3 and discuss the effect of different modifications on the design space. In all cases, the material structure construction problem has been reduced to the problem of matching and selecting neighborhoods in the reference structure X and reassembling them in the target structure Y by a map t shown as a dashed arrow in Figure 4.2. We also observe that the reformulation in terms of neighborhoods reduces the difficult inverse homogenization problem to a problem of filtering: only those neighborhoods in $N(X)$ that have desired material properties $g(P(X))$ will be selected for use in the target material structure $N(Y)$.

4.2 Effective material properties via descriptors

The last remaining obstacle to solving the material structure construction problem is the need to evaluate material property P on any neighborhood in both reference and target materials. This is a non-trivial task that usually involves solving multiple boundary value problems, making the design procedure inefficient and impractical.

Instead, we propose to replace material properties $P(X)$ by their proxies: a collection of geometric, topological, and statistical material descriptors $D(X)$ that are easily computable for a given neighborhood $N(x)$ of the material structure. Specific examples of $D(X)$ include correlation functions [157] and Minkowski functionals [59]. Numerous studies [42, 104, 60, 172] focus on relating the material properties with material descriptors because the latter can be measured directly.

Using material descriptors allows us to transform the commutative diagram in Figure 4.2 into the one shown in Figure 4.3. The map a represents the relationship between material properties $P(X)$ and their material descriptors $D(X)$. Just like material properties, material descriptors $D(X)$ are spatially varying fields that are computed on neighborhoods in X and can be evaluated at any point $x \in R^3$ yielding $D(x)$. When map a is invertible, there is a one-to-one correspondence between properties $P(X)$ and descriptors $D(X)$. With this assumption, selecting neighborhoods

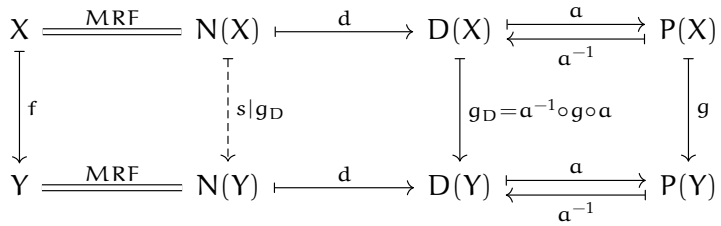

Figure 4.3: FGM structure modeling. Problem formulation via material descriptors.

$N(Y)$ possessing properties $P(Y)$ becomes equivalent to matching material descriptors $D(Y)$. The latter task is much simpler because it involves only geometric computations.

4.3 Hybrid sampling algorithm for non-stationary MRF

In Chapter 3, we have shown that the Wei - Levoy algorithm is able to duplicate a stationary material structure with a guaranteed accuracy of consistently estimating the joint distribution as well as material descriptors on a predefined neighborhood window. The practical implication of this result is twofold: (1) any neighborhood $N(y)$ in the duplicated structure Y almost surely exists in its counterpart reference structure X, i.e. we expect that $N(Y) \subset N(X)$; (2) the probability distributions of such neighborhoods with regards to both structures are also the same, as a direct consequence of the stationarity assumption. We seek to extend these results to the case when X and Y are graded material structures, through guiding the neighborhoods selection by the material descriptor fields $D(Y)$. Suppose we are looking to select a neighborhood $N(x)$ that best matches the neighborhood $N(y)$ at a location y. Just like in the stationary case, the measure d_N of neighborhood match is determined by the voxel-wise (or pixel-wise in 2D) difference:

$$d_N(x, y) = \|X_{N(x)} - Y_{N(y)}\|. \tag{4.2}$$

However, we are only interested in those neighborhoods that also satisfy the second condition of Equation 4.1, with $D(Y)$ playing the role of the target material property $P(Y)$. Accordingly, we

define an additional measure d_D to account for differences in the descriptor fields $D(x)$ and $D(y)$ at the same locations using a weighted L_1 norm:

$$d_D(x) = \sum_{i=1,2...k} w_i |D_i(x) - D_i(y)| \tag{4.3}$$

where D_i is the i-th material descriptor in D, and user-assigned weights are subject to $w_i \in [0,1], \sum_i w_i = 1$.

The final selection of the neighborhood $N(x)$ for construction of a graded material structure Y must be determined by a best match, determined by some combination of d_N and d_D. There are two ways in which d_D may be used to modify the sampling process: as a hard constraint or a soft constraint on the neighborhood selection procedure. As a *hard constraint*, for each synthesis step, neighborhoods $N(x)$ measuring large deviations from the target descriptors $D(Y)$ will not be used in the neighborhood selection process. Using the d_D as a filter to remove neighborhoods without the target material properties effectively guarantees that all synthesized neighborhoods will conform to the descriptor fields. However, eliminating too many candidate neighborhoods in could result in the intersection of two design space become empty and therefore leads to geometric discontinuities, which may in turn lead to undesirable physical defects (e.g. stress concentrations) in the synthesized structure Y. This is generally not an issue in a reconstruction, when the target field $D(Y)$ is (approximately) identical to the reference field $D(X)$, but it could easily happen in design where the target field $D(Y)$ is specified by a user or another application.

The alternative *soft constraint* use d_D as a penalty term in the neighborhood selection process. A total measure d_{total} of mismatch is defined between the two neighborhoods as a weighted (convex) combination of d_N and d_N :

$$d_{total} = (1-\alpha) d_N + \alpha d_D, \tag{4.4}$$

where $\alpha \in [0,1]$ allows to control the relative influence of geometry and material descriptors in the selection process. At each step of the synthesis process, a neighborhood N(x) with minimum d_{total}

is selected and laid onto Y. This approach is favored in computer graphics application while the hard constraint has a clearer meaning of the design space which is the intersection of design space defined by the MRF and by the material properties, which includes all material structures share the same macroscopic material property distribution.

We hereby propose a hybrid approach which adds a tolerance to the target properties field and still use the sum of the weighted difference (Equation 4.4) to select the neighborhoods. The hybrid approach not only increase the efficiency of the sampling algorithm by filtering out the unfitted neighborhoods but also has a well defined design space.

Recall that Wei-Levoy algorithm guarantees the quality of reconstruction Y only under the assumption of strict stationarity of X [76]. In contrast, the quality of the constructed graded material is determined by how well the target descriptors fields $D(Y)$ are able to adapt to the input structure X. This in turn depends on the compatibility condition which will be discussed in the next section.

4.4 The quality of the design result

In a typical design problem, target fields $D(Y)$ may be created directly as a scalar or vector field via a map g that could be a combination of various gradation techniques. It is not reasonable to expect that every such property $D(Y)$ can be realized by selecting neighborhoods in $N(X)$. For example, the system of Equations 4.1 may become "over constrained" when a target property does not exist in the reference material or there are no adjacent neighborhoods in the reference structure satisfying the properties of the adjacent neighborhood in the target field. If there exists Y satisfying both conditions in Equation 4.1, we say that the target fields $D(Y)$ are *compatible* with given reference material X and neighborhood size s. When $D(Y)$ is compatible, the sampling result is the exact solution of Equation (4.1); when the $D(Y)$ is incompatible, the sample result yields an approximate solution based on the weight α.

The "binary" definition above is often too restrictive to be true except for a few special cases,

such as reconstructing a stationary periodic structure or when target descriptor fields $D(Y)$ is exactly the same as $D(X)$ (see bone reconstruction example in Section 4.5.1). Nonetheless, it gives some theoretical backgrounds on what to expect for the quality of the synthesized result Y: in real design scenarios, a perfect solution usually does not exist due to the lack of compatibility between the inputs. To quantitatively assess the quality of the result Y, we introduce the notion of (N, D) - *compatible*, where N measures the maximum mismatch between neighborhoods (d_N) and D measures the maximum deviation from target descriptors (d_D). It is noted that the same notion may extend to quantify the degree of compatibility between X, s, and $D(Y)$ by the quality of the optimal solution of Equation 4.1. Design problems satisfying the original compatibility definition are (0,0) - compatible with this new notion.

4.5 Bone structure design and reconstruction

4.5.1 Femur bone reconstruction

In this section, we demonstrate the effectiveness of the proposed approach for reconstruction of a 2D (image of) femur bone structure (Figure 4.4(a)). Minkowski functionals are the preferred material descriptors in that they are standard measurements for bone structure characterization [55]. There are exactly $d + 1$ for a d-dimensional material structure: volume, surface area, average mean curvature, and Euler characteristic for $d = 3$, and area, perimeter, and Euler characteristics for $d = 2$. Regions of different properties in bone structures can be differentiated by Minkowski functionals.

For ease of comparisons, both d_N and d_D in Equation 4.4 are normalized into range $[0, 1]$. Three Minkowski functionals are equally weighted and α is chosen as 0.9. Both the reference and reconstruction results are discretized on a lattice of 399 by 343 pixels, with a fixed size neighborhood of 25 by 25 pixels. Figure 4.4 (b)-(d) show the fields of Minkowski functionals $D(X)$ for the reference bone structure X: area, perimeter and Euler characteristic. Since this is a reconstruction problem,

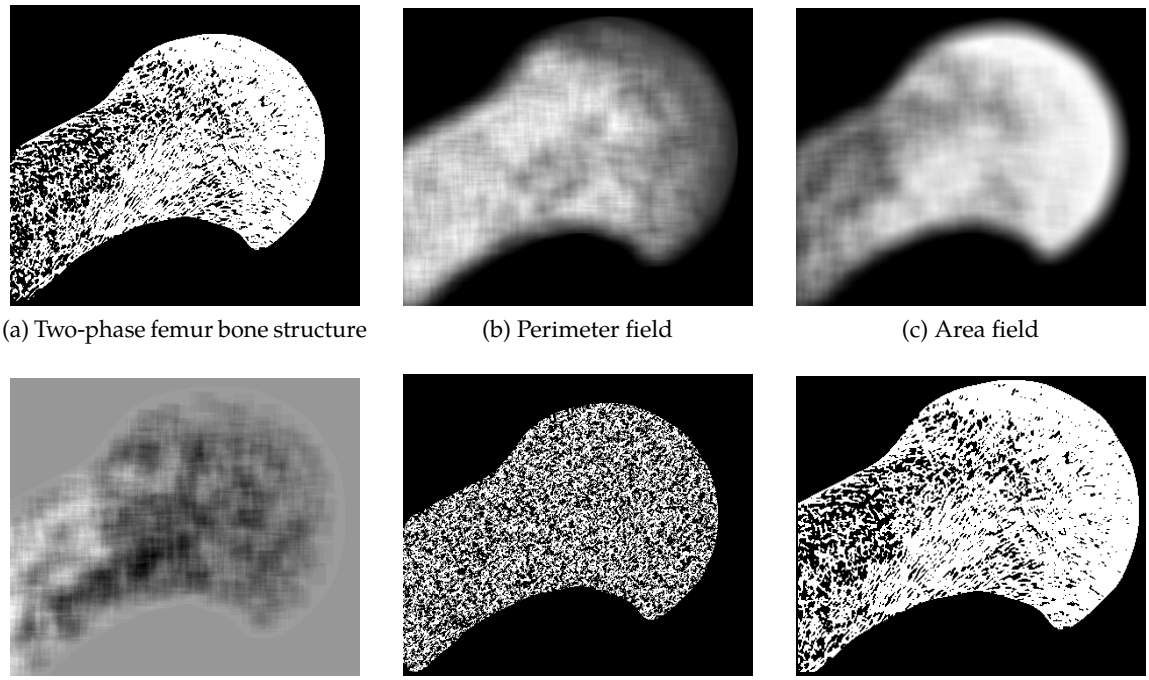

(a) Two-phase femur bone structure (b) Perimeter field (c) Area field

(d) Euler characteristic field (e) Reconstruction without Minkowski functionals fields (f) Reconstruction with Minkowski functionals fields

Figure 4.4: Femur bone structure reconstruction. (a) shows a cross-section of a two-phase femur bone structure, (b) - (d) are Minkowski functionals fields of (a), (e) and (f) are reconstruction results without and with Minkowski functionals as descriptors fields.

the target descriptors fields $D(Y)$ are identical to $D(X)$. The inputs are (0,0) - compatible because X itself is the (0,0) - compatible solution we seek. Figure 4.4 (e) and (f) are reconstructions with and without the control of Minkowski functionals fields. As expected, reconstructions with Minkowski functionals fields are noticeably better than reconstructions without it. We successfully recovered the X since we are only selecting the neighborhoods in Figure 4.4 (a) targeting its own Minkowski functionals fields. It took 3.4s for a relatively inefficient MATLAB implementation to reconstruct Figure 4.4 (f) on an Intel Core i7 3.4 GHz CPU.

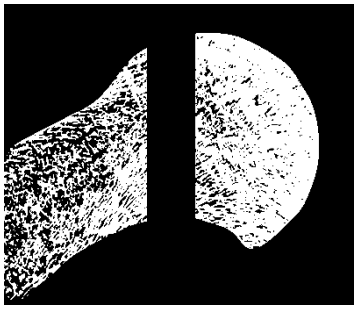

(a) Femur bone with the deteriorated region removed

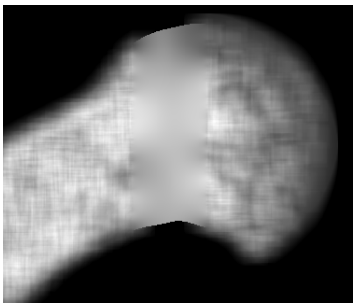

(b) Interpolated perimeter field

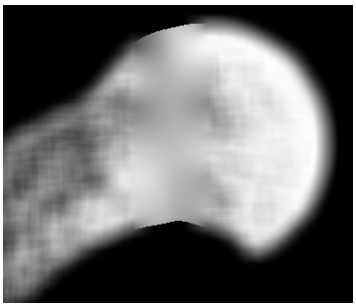

(c) Interpolated area field

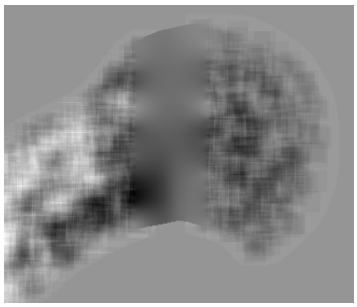

(d) Interpolated Euler characteristic field

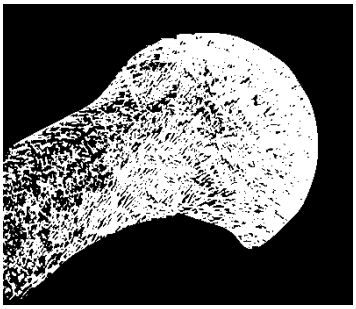

(e) Design of missing bone structure with Minkowski functionals field from original bone sample (Figure 4.4(c)).

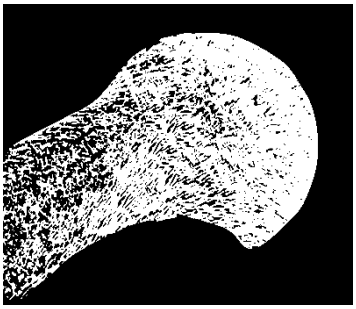

(f) Design of missing bone structure with Minkowski functionals field interpolated from existing structures.

Figure 4.5: Design of missing femur bone structures. (a) shows the Femur bone with missing bone structures. (b) - (d) are target Minkowski functionals fields designed by inverse distance interpolation from the healthy bone regions. (e) and (f) show the synthesized bone structures different target descriptors fields.

Table 4.1: Maximum and mean difference of Minkowski functionals between designed structures and original bone structures over designed region. Minkowski functionals are rescaled to [0, 1].

	Area		Perimeter		Euler characteristic	
	max	mean	max	mean	max	mean
Figure 4.5 (e)	0.2342	0.0178	0.1958	0.0121	0.3878	0.0467
Figure 4.5 (f)	0.3562	0.0236	0.2167	0.0177	0.4286	0.052

4.5.2 Bone structure design

Bone structures are vulnerable: diseases, physical injuries, and corticosteroids are among various reasons leading to their degradation. In rare cases, the deteriorated region needs to be removed and a bone scaffold may be implanted to stimulate the bone to regenerate itself as well as to bear loads. An ideal design of scaffold should mimic the bone structure in terms of mechanical properties, porosity and should be bio-compatible, bio-active or bio-resorbable to enhance tissue growth [52, 14]. With the assumption that a more natural shape would be more stimulating to bone regeneration process, it is possible to design the scaffold as the complement of the synthesized bone structure.

Figure 4.5 (a) shows a femur bone with deteriorated region removed. To design the target Minkowski functionals fields, we interpolate Minkowski functionals values of the existing bone structure weighted by the inverse distance [13] . In other words, Minkowski properties at any point are represented as the weighted sum of the properties known at some locations (typically points or boundaries), where the weights are inversely proportional to the powers of distances to these locations:

$$D(y) = \begin{cases} \sum_{i=1}^{N} \frac{D(y_i)}{d(y,y_i)^p} / \sum_{i=1}^{N} \frac{1}{d(y,y_i)^p}, & \forall i, d(y,y_i) \neq 0 \\ D(y_i), & \exists i, d(y,y_i) = 0 \end{cases} \tag{4.5}$$

where d is the Euclidean distance between two points and each y_i represents the center of an existing neighborhood in Figure 4.5 (a). Figure 4.5 (b) - (d) show the interpolated target descriptors fields with the power of distance equals 4. For non-convex domains, interpolation with interior distances may be advantageous [35].

Figure 4.5 (e) and (f) are generated bone structures from the 25 by 25 neighborhoods available in Figure 4.5 (a): with the target Minkowski functional fields calculated from the original intact bone (Figure 4.4 c) in (e), and with interpolated target Minkowski functional fields in (f). Note also that the proposed procedure connects the designed bone structures to the healthy part of (a) seamlessly. Mean and maximum differences between Minkowski functional values of the constructed results

and those computed from the original bone sample in Figure 4.5 (a) are summarized in Table 4.1. The results suggest that using inverse-distance interpolated fields as target descriptor fields is a viable alternative to replacing the original descriptor fields (which are likely to be unknown). We expect that the construction results can be improved further when additional reference materials may be available for neighborhood selection, for example, additional healthy bone samples from other sources.

4.6 Functionally graded lattice structure

One obvious way to design the property distributions of a functionally graded material is through optimization. We use the Solid Isotropic Material with Penalization (SIMP), a popular method for topology optimization, to design the distribution of stiffness inside the design domain [78]. SIMP iteratively updates the volume fraction (relative density) distribution inside the design domain to optimize the design objective, such compliances, while meeting a set of constraints, such as a constraint on the total volume of the part. The power law is used as the homogenization model to establish the relationship between material descriptor (volume fraction) and material property (stiffness) while penalizing the intermediate densities. After the iteration converges, the continuous volume fraction field is often thresholded to achieve a '0-1' design, but this is not necessary for our application. Instead, with the proposed method, we can fill the design space with any given material structures – random or periodic – according to the volume fraction field designed by the SIMP. Here, we show that the proposed method performs equally well on periodic lattices.

Table 4.2: Errors and compatibility of the 3D synthesis results.

	Volume fraction		Neighborhood	
	max	mean	max	mean
Figure 4.6 (d)	0.1004	0.0128	0.1450	0.0334
Figure 4.7 (b)	0.1700	0.0163	0.1253	0.0416
Figure 4.7 (d)	0.1378	0.0247	0.1327	0.0402
Figure 4.8 (d)	0.1481	0.0152	0.1791	0.0391

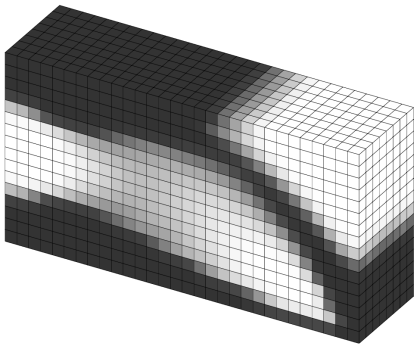

(a) Target volume fraction distribution from 0.3 to 0.85, $30 \times 16 \times 8$.

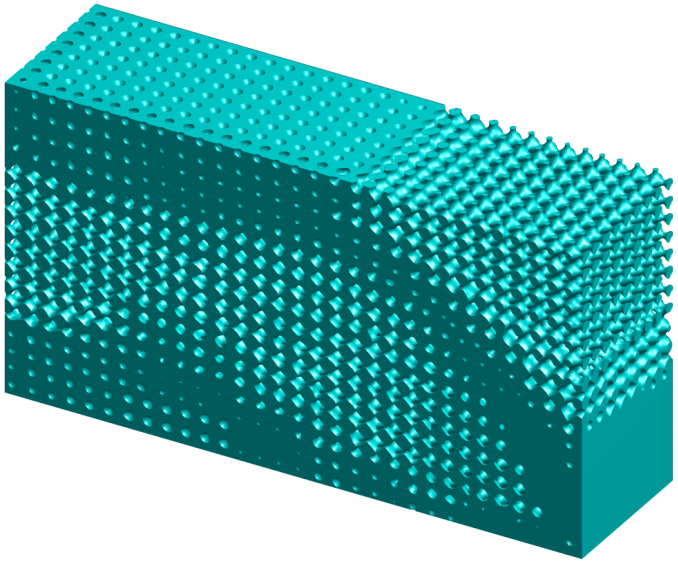

(b) FGM structure synthesized by the proposed framework, $300 \times 160 \times 80$.

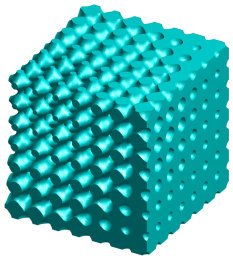

(c) Reference material, $80 \times 80 \times 80$.

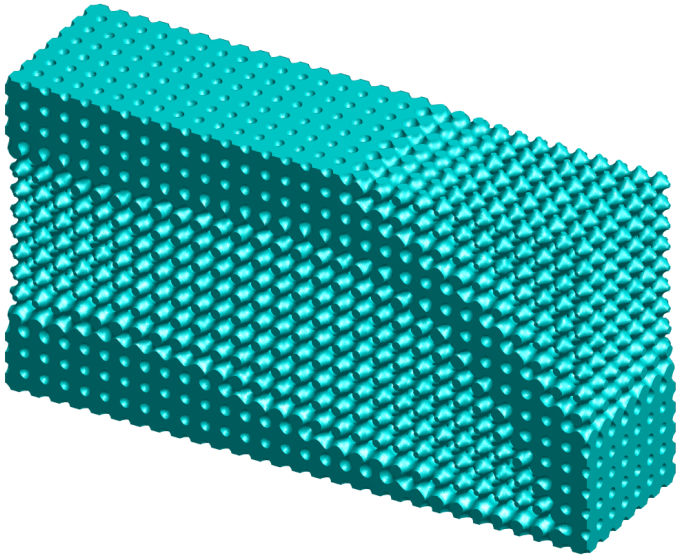

(d) FGM structure generated by procedural method, $300 \times 160 \times 80$.

Figure 4.6: Design of graded material structure that is functionally a cantilever beam with fixtures on the top and bottom left edges and downward loads on the bottom right edge. The target volume fraction field ranging from 0.3 to 0.85 is designed by SIMP with penalty factor equals 1.

Figure 4.6 demonstrates the design of a graded material structure that is functionally a cantilever beam with fixtures on the top and bottom left edges and downward loads on the bottom right edge. The target volume fraction distribution (Figure 4.6 a) is designed by SIMP with an overall volume fraction of 0.5. The lower and upper bounds of the volume fraction are 0.3 and 0.85. We set the penalty factor as one for a gradually varying volume fraction field. Figure 4.6 (c) shows the reference material: a procedurally generated spatially varying lattice. The synthesized structure is shown in Figure 4.6 (b) with a neighborhood size s of $14 \times 14 \times 14$ and 4 being the size of overlap along every direction. In some applications, such as 3D printing, the connectivity of the structure is very important: the generated structure is required to be a single connected piece. We enforce the connectivity by requiring every new neighborhood added to the synthesized structure to be a single connected one and connects to the existing neighborhoods. Other desirable properties such as smallest feature size can be guaranteed the same way by the construction. It is noted that not all volume fractions in the target fields are realized in the reference lattice. As a result, some of the target volume fractions are achieved approximately. The compatibility of the result is summarized in Table 4.2. For comparison, Figure 4.6 (d) shows the graded lattice generated using the same procedural method as the reference structure.

We observe that the reference lattice can be constructed by two types of unit cells (Figure 4.7 a and c) that are dual to each other. The two types can be differentiated by their Euler characteristics χ: $\chi = 1$ for type 1 and $\chi = -4$ or 2 for type 2. The Euler characteristic of type 2 unit cell switches from -4 to 2 with increasing volume fractions. $\chi = -4$ is calculated by gluing two triple torus ($\chi = -2$) together over a two-dimensional circle ($\chi = 0$): $-4 = -2 \times 2 - 0$. With the Euler characteristics, we control the synthesis of the lattice structures by selecting neighborhoods of type 1 or type 2 unit cells only. The results are illustrated in Figure 4.7 (b) and (d), respectively.

Summarized in Table 4.2, the difference in neighborhoods is calculated as the ratio of the mismatched voxel to the volume of the overlap region. The errors of Figure 4.6 (d) are smaller than Figure 4.6 (b) and (d). This is because that in Figure 4.6 (d) the Euler characteristics are not

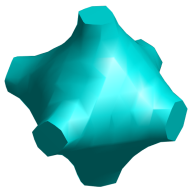

(a) Type 1 unit cell.

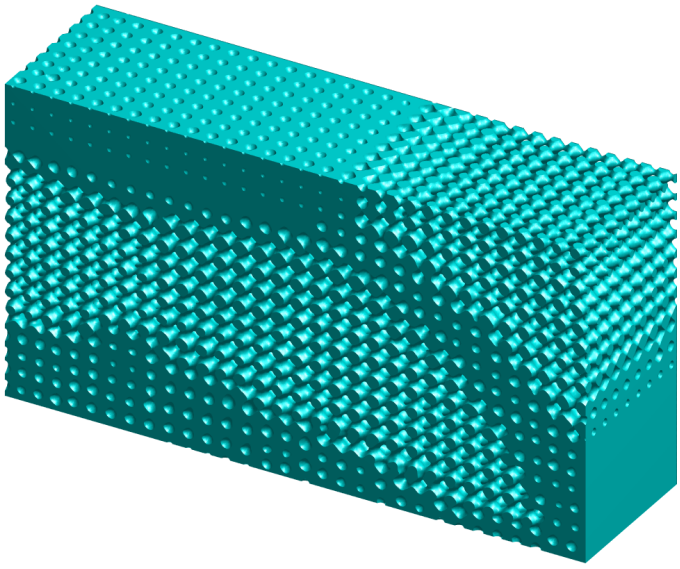

(b) FGM structure with type 1 unit cell.

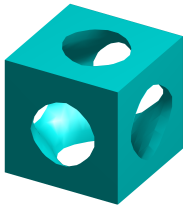

(c) Type 2 unit cell.

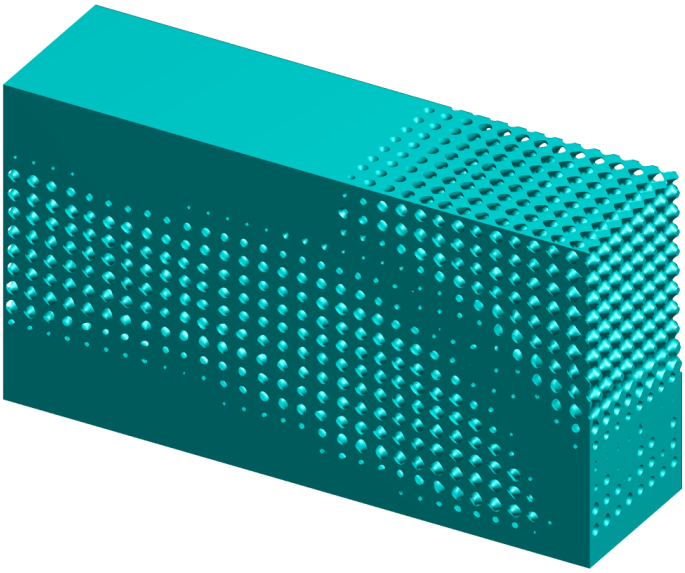

(d) FGM structure with type 2 unit cell.

Figure 4.7: Functionally graded lattice structures for a cantilever beam with different unit cells.

constrained and there are more neighborhoods to choose from. Figure 4.8 shows an additional example of a wheel design with fixtures on four lower corners and load on the center of the bottom surface. The connectivity of the neighborhood is not enforced for this example and small disconnected pieces can be seen near the edges. The neighborhoods with disconnected pieces are hardly mistakes as they do exist in the reference material. The computation time of each example takes about 90 minutes, which is significantly longer than the two-dimensional cases. This is because the algorithm is linear in time to not only the number of neighborhoods to generate in Y, but also the number of neighborhoods to search for in X and the size of overlap and all of them are significantly larger in 3D. Possible acceleration schemes are discussed in Section 4.7.

4.7 Discussion

We formulated the problems of design and reconstruction of functionally graded material structures as a process of selecting neighborhoods in a reference material sample. The new formulation allows to effectively bypass the difficult problem of inverse homogenization. We also introduced the notion of material descriptors, and Minkowski functionals in particular, to guide the construction of graded material structures, without the need to perform numeric homogenization or to solve boundary value problems. The fully implemented algorithm supports reconstruction and design of FGM structures by combining the influence of adjacent neighborhoods and target material descriptor fields with a clearing definition of the design space. We demonstrated the effectiveness of the proposed approach to reconstruction and design of graded bone structures as well as generating functionally graded lattice structures.

To speed up without compromising the quality of the result, we may compute d_N only for those neighborhoods with small d_D. Obviously, searching for such a subset of $N(X)$ will not jeopardize the quality of Y if $D(Y)$ and X are (0,0) – compatible. However, if not fully compatible, eliminating too many candidate neighborhoods in $N(X)$ could result in more geometric discontinuities, which

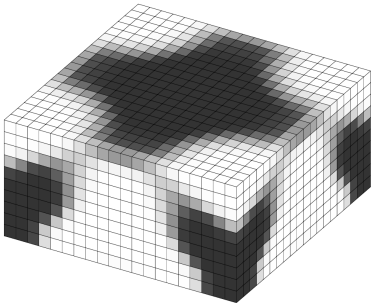

(a) Volume fraction distribution, $20 \times 20 \times 10$: view from top.

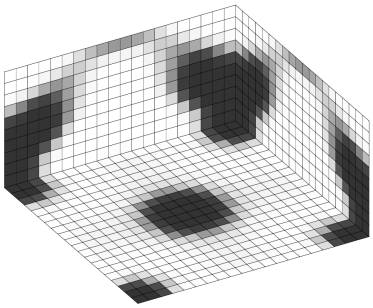

(b) Volume fraction distribution: view from bottom.

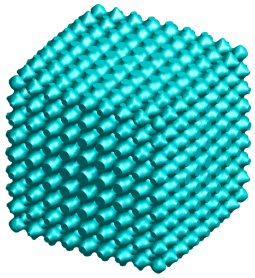

(c) Reference functionally graded lattice, $100 \times 100 \times 100$.

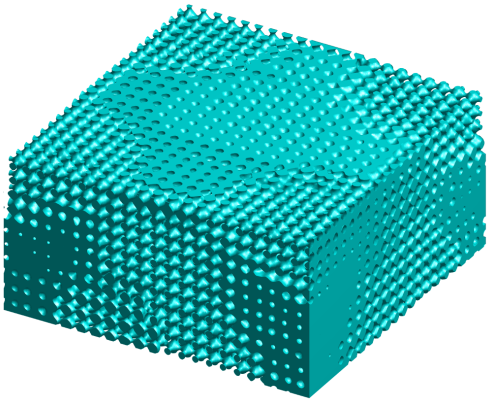

(d) FGM designed by the proposed framework: top. Resolution: $200 \times 200 \times 100$

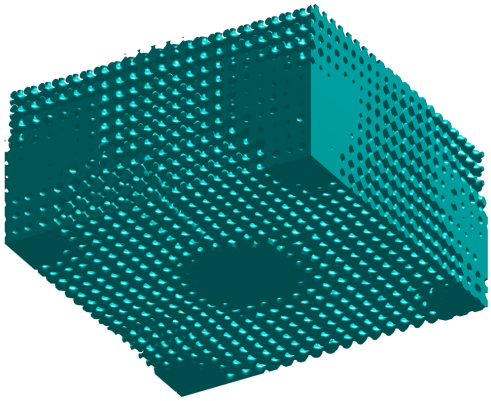

(e) Functionally graded structure designed by the proposed framework: bottom.

Figure 4.8: Design of graded material structure that is functionally a wheel structure with fixtures on four lower corners and load on the center of bottom surface. The target volume fraction field ranging from 0.3 to 0.85 is designed by SIMP with penalty factor equals 1.

may in turn lead to undesirable physical defects (e.g. stress concentrations) in the designed structure Y. This is the main reason a hybrid scheme is adopted in our implementation. To conclude, filtering $N(X)$ by $D(Y)$ should depend on the degree of compatibility and requires further studies.

An apparent limitation of the proposed method is that it cannot guarantee that the specified distribution of FGM properties is achieved, because this explicitly requires compatibility between the reference material structure and the target properties field. We note, however, that the notion of (N, D)-compatibility allows fine tuning the tradeoffs between the neighborhood and the descriptor

incompatibilities. Methods for evaluating the compatibilities *a priori* appear to be a useful direction for future explorations. Remedies for large incompatibilities include modifying the target property fields, enriching or modifying the reference material structure, or both. For example, the reference material structure may be modified using morphological operations to increase compatibility, but such modifications could also alter the properties of the reference material. New reference material structures could also be designed by other methods reviewed in Chapter 2, when the target properties are beyond the reach of the direct modification of the reference material structure.

Chapter 5

Efficient material property estimations by FFT-based homogenization

Relating the macroscopic properties to material structure is a long-standing problem, attracting the attention of Poisson, Faraday, Maxwell, Rayleigh, and Einstein [101]. Numerous studies have been conducted to relate material properties with material descriptors given the latter can be measured directly. For example, transport processes are sensitive to the distances between particles in particulate materials [158]. Minkowski functionals is known to correlate with some of the bone diseases, such as osteoporosis, as discussed in Chapter 4.

In the current Chapter, we study the efficient evaluation of mechanical property of heterogeneous material as well as its prediction through correlation functions. We limit our focus on linear elasticity but the formulation lays the foundation for non-linear problems and extends to the determination of thermal and electrical conductivity, diffusion coefficient, dielectric constant, and magnetic permeability tensors as they share the same linear form as linear elasticity. We first introduce the Lippmann-Schwinger equation, which is an intrgral equation forming the basis of the both our algorithms of effective material properties homogenization and effective material properties estimation through correlation function. Then we convert the integral equation into a

system of linear equations that is symmetric and positive definite and can be solved efficiently using the conjugate gradient method and Fourier transform. We conclude this chapter with an application of the method to homogenize a mesoscale structure fabricated by additive manufacturing. Some results in this chapter has been reported in [80].

5.1 Homogenization via Lippmann-Schwinger equation

As discussed in Chapter 2, Finite Element Method (FEM) is the most common method to homogenize heterogeneous material computationally by solving the six independent linear elasticity problems. In the present work, we discuss an alternative approach to homogenization formulated using Green's function. Although the development of the method dates back to 1970s [171, 64, 150, 69], its further application is limited by a major computational difficulty in the formulated integral equation: computing the convolution of the Green's function. As a result, the formulation was only used to predict effective properties or estimate their bounds based on the statistics of microscopic material structures [33]. It is only recently an efficient solution of the integral equation was proposed, allowing the application of the approach to the detailed models of material structures.

Evaluating the convolution using Fourier transform was first proposed by Moulinec and Suquet [107]: by the convolution theorem, the convolution in real domain becomes multiplication in the frequency domain. Just as in FEM-based homogenization, the periodic boundary conditions are usually assumed for the material [61]. Fourier transform also assumes the periodicity of the function implicitly. The first attempt [107], often referred as the basic scheme, solves the problem through the fixed-point iteration which is equivalent to the Neumann series solution of the integral equation. In this approach, the number of iterations needed for convergence grows linearly with the contrast in material coefficients between different phases. The contrast here refers to the magnitude of difference between the coefficients in the respective material tensors. As a result, the iteration may not converge for phases with infinite contrast, e.g. porous materials. It was later discovered that

the lack of convergence is due to the Neumann series expansion rather than the formulation of the problem and will be corrected if other iterative linear solvers are applied [18]. The basic scheme inspired many follow-up results, mainly focusing on improving the convergence speed and the convergence with arbitrary phase contrast [100, 162, 17, 176]. The Fourier transform of the problem was later shown to be mathematically equivalent to Galerkin approximation with trigonometric polynomials [163]. Our efficient solution described in Section 3 relies on the combination of FFT and conjugate gradient methods, exploiting the fact that the resulting system of linear equation is symmetric and positive definite.

For a heterogeneous material with elasticity tensor C subject to the displacement boundary condition, the displacement u, stress σ, strain ϵ, and body force b must conform to the following equilibrium equations:

$$\begin{aligned} \operatorname{div}\sigma + b &= 0, \quad x \in \Omega \\ \sigma = C\epsilon, \quad \epsilon &= \frac{1}{2}[\nabla u + (\nabla u)^T], \\ u(x) &= u^0(x), \quad x \in \partial\Omega. \end{aligned} \tag{5.1}$$

Given a homogeneous reference comparison material with the constant elasticity C^0, the stress polarization tensor τ may be defined:

$$\tau = \sigma - C^0\epsilon = (C - C^0)\epsilon. \tag{5.2}$$

Substituting Equation (5.2) into Equation (5.1) gives

$$(C^0_{ijkl}u_{k,l})_{,j} + \tau_{ij,j} + b_i = 0. \tag{5.3}$$

Since equations (5.3) is linear, its solution can be separated as $u = u^0 + u^1$, where u^0 is the solution

of the real body force b and u^1 is the solution of additional body force $\mathrm{div}\tau$:

$$(C^0_{ijkl}u^0_{k,l})_{,j} + b_i = 0, \tag{5.4}$$

$$(C^0_{ijkl}u^1_{k,l})_{,j} + \tau_{ij,j} = 0. \tag{5.5}$$

Introducing the Green's function (Equation A.8) into Equation (5.5) for the comparison material, the stress polarization tensor τ becomes the "body force", from Equation (A.9)

$$u^1_i(x) = \int_\Omega G_{ip}(x, x')\tau_{pq,q}(x')\, dx', \tag{5.6}$$

by integrating by parts and combining with u^0

$$u_i(x) = u^0_i(x) - \int_\Omega \frac{\partial G_{ip}(x, x')}{\partial x'_q}\tau_{pq}(x')\, dx', \tag{5.7}$$

by differentiation and the symmetry of strain tensor

$$\epsilon_{ij}(x) = \epsilon^0_{ij}(x) - \int_\Omega \Gamma_{ijpq}(x, x')\tau_{pq}(x')\, dx', \tag{5.8}$$

where

$$\Gamma_{ijpq}(x, x') = \left.\frac{\partial^2 G_{ip}(x, x')}{\partial x_j \partial x'_q}\right|_{(ij),(pq)}. \tag{5.9}$$

The bracketed subscripts imply symmetry, which is the results of symmetries in the elasticity tensor. G is the Green's function of an infinite size material:

$$[C_{ijkl}(\mathbf{x})G_{kp,l}(\mathbf{x}, \mathbf{x}')]_{,j} + \delta_{ip}\delta(\mathbf{x} - \mathbf{x}') = 0. \tag{5.10}$$

The close form expressions of Γ and G is explicitly known in the frequency domain, as summarized in the next section. Let $\delta C = C - C^0$, and substitute in Equation (5.2), Equation (5.8) leads to the

solution of ϵ, also known as the Lippmann-Schwinger equation:

$$\epsilon(x) = -\int_{\Omega} \Gamma(x, x')\delta C(x')\epsilon(x')dx' + \epsilon^0(x), \tag{5.11}$$

This derivation follows the classical results of Korringa [64] and Kroner [69].

The solution of Equation (6.3) is the strain tensor distribution $\epsilon(x)$ within the material domain. The stress tensor field is subsequently computed as the point-wise multiplication of the modeled material elasticity tensor field by the strain tensor distribution: $\sigma(x) = C(x)\epsilon(x)$. Our implementation follows Mandel's notation, where the 2nd-rank strain and stress tensors are mapped to six-dimensional vectors and the 4th-rank elasticity and compliance tensors are mapped to 6×6 matrices. After repeating this process six times independently, the effective elasticity tensor can be computed as:

$$C^{\text{eff}} = \begin{bmatrix} \vdots & \vdots & \vdots & \vdots & \vdots & \vdots \\ \sigma_1 & \sigma_2 & \sigma_3 & \sigma_4 & \sigma_5 & \sigma_6 \\ \vdots & \vdots & \vdots & \vdots & \vdots & \vdots \end{bmatrix} \begin{bmatrix} \vdots & \vdots & \vdots & \vdots & \vdots & \vdots \\ \epsilon_1 & \epsilon_2 & \epsilon_3 & \epsilon_4 & \epsilon_5 & \epsilon_6 \\ \vdots & \vdots & \vdots & \vdots & \vdots & \vdots \end{bmatrix}^{-1} \tag{5.12}$$

If the input strain vector is of unit length and parallel to the axes, the strain matrix in Equation (5.12) will be an identity matrix so that the inversion is not required. This is because the averaged strain always equals to the prescribed constant strain per Equation (2.6). This identity can also be used to verify the implementation of the algorithm.

As a Fredholm integral equation of the second type, the classical solution of Equation (6.3) requires Neumann series expansion [120] which coincides with the fixed-point iteration used in the basic scheme:

$$\epsilon^{i+1}(x) = \epsilon^i(x) - \mathcal{F}^{-1}\left[\hat{\Gamma}\mathcal{F}(\delta C\epsilon^i(x))\right] \tag{5.13}$$

where $\mathcal{F}$ and $\mathcal{F}^{-1}$ represents the forward and inverse Fourier transform and $\hat{\Gamma}$ is the Green's operator in the frequency domain. One drawback of the Neumann series expansion is that it suffers slow convergence when the contrast of material properties increases, which is undesirable for porous materials. In the next section, we show that the relationship between correlation functions and

effective elasticity tensor is a direct result of Neumann series expansion of Lippmann - Schwinger equation.

5.2 Solve Lippmann-Schwinger equation as a symmetric and positive definite linear system

As discussed in Section 1, one drawback of the Neumann series expansion solution is its slow convergence. We now describe a method to solve the Equation (6.3) by the conjugate gradient method after converting it into a system of linear equations. Though the integration kernel Γ is inseparable in the continuous domain, it can be separated approximately with the following piecewise linear approximation:

$$\begin{aligned} \Gamma(x, x')\delta C(x') &\approx \sum_{j=1}^{N} u_j(x) v_j(x'), \\ u_j(x) = \Gamma(x, j)\delta C(j), \quad v_j(x') &= \begin{cases} 1, & \text{if } x' = j \\ 0, & \text{if } x' \neq j \end{cases}. \end{aligned} \tag{5.14}$$

Substitute Equation (5.14) into Equation (6.3):

$$\begin{aligned} \epsilon(x) &= -\int_{\Omega} \Big[\sum_{j=1}^{N} u_j(x) v_j(x') \Big] \epsilon(x') dx' - \epsilon^0(x) \\ &= -\sum_{j=1}^{N} \Big[u_j(x) \int_{\Omega} v_j(x') \epsilon(x') dx' \Big] + \epsilon^0(x), \end{aligned} \tag{5.15}$$

Since $\int_{\Omega} v_j(x')\epsilon(x')dx'$ is the sampling of continuous ϵ over Ω, let

$$\int_{\Omega} v_j(x')\epsilon(x')dx' = \epsilon_j. \tag{5.16}$$

Substitute Equation (5.16) into Equation (5.15):

$$\epsilon(x) = -\sum_{j=1}^{N} u_j(x)\epsilon_j + \epsilon^0(x). \tag{5.17}$$

Substitute Equation (5.17) back into Equation (5.16), we have

$$\begin{aligned}
\epsilon_i &= -\int_\Omega v_i(x')\Big[-\sum_{j=1}^{N} u_j(x')\epsilon_j + \epsilon^0(x')\Big]dx' \\
&= -\sum_{j=1}^{N} \epsilon_j \int_\Omega v_i(x')u_j(x')dx' + \int_\Omega v_i(x')\epsilon^0(x')dx' \\
&= -\sum_{j=1}^{N} \Gamma(i,j)\delta C(j)\epsilon_j + \epsilon_i^0 \\
\epsilon_i^0 &= \Big[\delta_{ij} + \sum_{j=1}^{N} \Gamma(i,j)\delta C(j)\Big]\epsilon_j = \Big[\delta_{ij} + \sum_{j=1}^{N} \Gamma_{ij}\delta C_j\Big]\epsilon_j.
\end{aligned} \tag{5.18}$$

Or in matrix form:

$$A\epsilon = \epsilon^0,$$

$$A = \begin{bmatrix}
I + \Gamma_{11}\delta C_1 & \Gamma_{12}\delta C_2 & \dots & \Gamma_{1N}\delta C_N \\
\Gamma_{21}\delta C_1 & I + \Gamma_{22}\delta C_2 & \dots & \Gamma_{2N}\delta C_N \\
\vdots & \vdots & \ddots & \vdots \\
\Gamma_{N1}\delta C_1 & \Gamma_{N2}\delta C_2 & \dots & I + \Gamma_{NN}\delta C_N
\end{bmatrix}, \tag{5.19}$$

where $\Gamma_{ij} = \Gamma_{i-j} = \mathcal{F}^{-1}(\hat{\Gamma}(\xi))$. Note that every block in A is a 6×6 matrix representing a 4th rank tensor. Apparently, A is not symmetric in general. However, by letting

$$\begin{aligned} B &= A\delta C^{-1} \\ &= \begin{bmatrix} \delta C_1^{-1} + \Gamma_{11} & \Gamma_{12} & \dots & \Gamma_{1N} \\ \Gamma_{21} & \delta C_2^{-1} + \Gamma_{22} & \dots & \Gamma_{2N} \\ \vdots & \vdots & \ddots & \vdots \\ \Gamma_{N1} & \Gamma_{N2} & \dots & \delta C_N^{-1} + \Gamma_{NN} \end{bmatrix}, \end{aligned} \tag{5.20}$$

the linear system transforms into:

$$B\delta C(\delta C^{-1}\tau) = \epsilon^0. \tag{5.21}$$

δC can be seen as the *right preconditioner* for the linear system with τ as the unknown. Since only ϵ is required for homogenization, we just need to solve the preconditioned system $B\delta C\epsilon = \epsilon^0$. Γ is symmetric in that $\hat{\Gamma}$ is an even function by definition (Equation A.15). Given δC is also symmetric as a elasticity tensor, B is symmetric.

In order to solve this preconditioned linear system by the conjugate gradient (CG) method, B also needs to be positive definite [133]. It has been proved that the definiteness of B and δC are consistent [169]. We first give an intuitive explanation of the proof. First, Γ is positive definite because it has positive diagonal entries and is diagonally dominant as Γ decays rapidly with the increasing distance between x and x'. When C_0 is smaller than all the phases in Ω, δC is also positive definite. B is therefore positive definite.

The formal proof follows the proof given in [169], which requires virtual work equality:

$$\sigma_1 \epsilon_2 = 0, \tag{5.22}$$

for any divergence free stress σ_1 and strain ϵ_2 derived from a displacement that is 0 over the

boundary. First, we show that Γ is positive definite. Since

$$\tau_1 \Gamma \tau_2 = -\tau_1 \epsilon_2 = -\delta C \epsilon_1 \epsilon_2 = \epsilon_1 C_0 \epsilon_2, \tag{5.23}$$

Γ is seen to be positive definite after setting $\epsilon_1 = \epsilon_2$, as C_0 is positive definite.

When δC is positive definite, the positive definiteness of B is straightforward. Here we show the case when δC is negative definite. It is convenient to introduce strain polarization tensor η:

$$\tau = C_0 \eta, \qquad \eta = S_0 \tau = S_0 (C - C_0)\epsilon = S_0 \sigma - \epsilon \tag{5.24}$$

Using Equation (5.22) again,

$$\begin{aligned} \tau_1 \Gamma \tau_2 &= -\tau_1 \epsilon_2 = \eta_1 C_0 (\eta_2 - S_0 \sigma_2) \\ &= \eta_1 C_0 \eta_2 - \eta_1 \sigma_2 = \eta_1 C_0 \eta_2 - \sigma_1 S_0 \sigma_2, \end{aligned} \tag{5.25}$$

Since $(C - C_0)^{-1} C_0 = S_0 (S_0 - S)^{-1} - I$,

$$\begin{aligned} \tau (C - C_0)^{-1} \tau &= \eta L_0 (C - C_0)^{-1} L_0 \eta \\ &= \eta (S_0 - S)^{-1} \eta - \eta C_0 \eta. \end{aligned} \tag{5.26}$$

Then $\delta C^{-1} + \Gamma = \eta (S_0 - S)^{-1} \eta - \sigma_1 S_0 \sigma_2$ is negative definite when δC is negative definite. Then $B \delta C$ becomes positive definite as both B and δC are symmetric.

Given the usually large N, constructing A can be prohibitively expensive. Fortunately, for every iteration, CG only needs the results of $A\epsilon$ for any vector ϵ and there is no need to represent A explicitly. Since $A\epsilon = \epsilon + \Gamma * (\delta C \epsilon)$, where $*$ represents convolution, the vector is efficiently computed in the frequency domain. Note that the combination of Fourier transforms and CG has been explored before in [176], despite the authors' belief that the linear system is not symmetric. Our analysis of the integral equation and explicit derivation of the corresponding linear system above

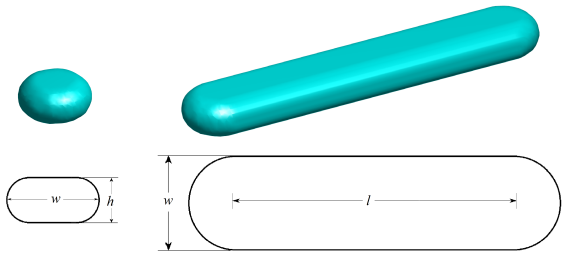

Figure 5.1: The shape of the minimum manufacturing volume and a single road. w, l, and h, represent the width, length of the road and layer height, respectively.

justifies the use of CG even though the corresponding linear system appears to be non-symmetric.

5.3 Experiment validation with FEM and physical tests

To demonstrate the effectiveness of the proposed approach, we compare the computed homogenization results with those predicted by the finite element method, and validate the predicted effective macro scale material properties by the known results of physical tests. Both of these comparisons are based on the parts that are additive manufactured. Therefore, we first review the effective geometry - material model introduced in [80].

5.3.1 Effective geometry - material model of additively manufactured structures

Intuitively, we would like to simulate the FDM printing process as a deposition of filament along the specified toolpath. At any given instant, the printer's head deposits some minimum manufacturing volume (MMV), whose shape may be approximated in terms of simple quadratic and/or superelliptic primitives with dimensions determined by the road width and layer height (see Figure 5.1 left). The shape of the road may be represented as the sweep of MMV along the toolpath specified by the instructions in the G-code, as shown on the right. Sweeping MMV over all toolpaths in the G-code yields a first approximation of the geometry discretized by the printing process. Figure 5.2 shows the design model, toolpath, and the reconstructed printed shape of a two-dimensional infill

pattern generated through Customizer by MakerBot [106]. Such an idealized geometry model was proposed in [94] and can be used to reason about stair-stepping, surface roughness, air gaps, and other small geometric differences between the designed and printed model.

We will adopt this idealized geometric model as a first approximation of the mesoscale geometry-material model, based on the assumption that most of the differences between the mechanical performance of the designed and printed structures originate in the process planning stage. This is reasonable because the air gaps and the bonding interface between the roads, which are modeled by the idealized geometry model, impact the mechanical performance of the printed structure far more significantly than dimension inaccuracy and printing imperfections due to gravity and random events such as inconsistent polymer flow. Global deformations such as warping due to thermally induced stress are not modeled since they cannot be predicted without first solving the effective material problem under consideration in this chapter. Another limitation of the idealized geometry model is that the union of the roads is not volume conservative. The model will underestimate the total volume of the base material when the distance between the parallel toolpath is smaller than the road width. We expect that such problem is less likely to happen with a proper toolpath.

A standard method for modeling a multi-phase material structure is to partition the overall domain into regions with distinct but known material properties. Thus, idealized geometry model distinguishes the space occupied the roads from the voids. However, the elastic properties of the roads themselves vary significantly over the roads and are not generally known. Firstly, it is very difficult to predict the properties of the solidified road base material that is remelted from the filament and extruded through the nozzle during the deposition process. Furthermore, the elasticity tensor of the filament itself is likely to be incomplete since only the stiffness in the direction of filament extrusion can be tested in most scenarios. Secondly, the stiffness of the deposited material changes significantly in the areas where adjacent roads are bonded together and is also difficult to predict. The quality of the bonds between the roads depend not only on the neck (contact area) formed between the adjacent roads, but also the molecular diffusion and randomization at the interface

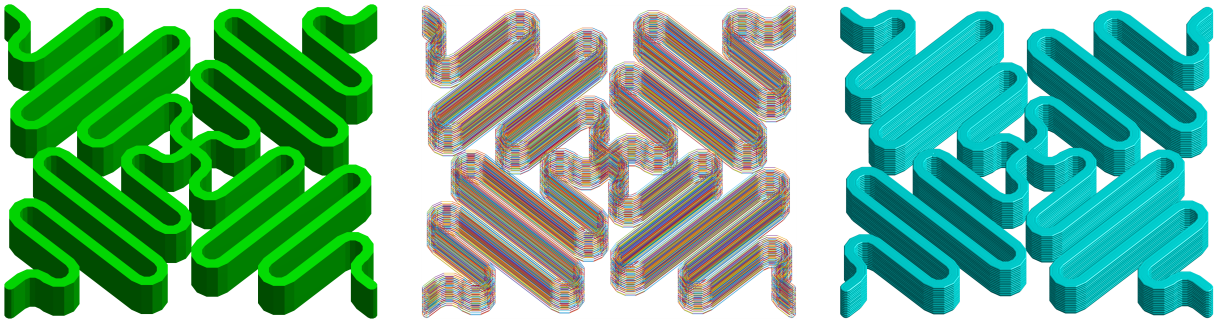

(a) Design model represented by triangle tessellation.

(b) Toolpath as a collection of line segments.

(c) Printed model reconstructed from the toolpath (b) with road width $w = 0.3$.

(d) Reconstructed printed model with $w = 0.25$.

(e) Detailed view of (c).

(f) Detailed view of (d).

Figure 5.2: Printed geometry model for a two-dimensional infill pattern.

[7]. Heat transfer and thermal history models, such as the ones proposed in [144, 7], are required to predict the strength and stiffness of the bond. The compound complexity of these physical phenomena casts serious doubts on the feasibility of being able to predict material properties of the idealized geometry model either computationally or experimentally.

In contrast, the measured material properties published by various manufacturers estimate not material properties of the constituent phases, but the effective material properties of the specimen formed by uniform patterns of parallel roads (Figure 5.3) (top). These measurements determine the compounded effects of the stiffness of the roads, air gaps and the bonding between the roads; the properties are averaged over an effective domain, shown as the blue rectangular region in Figure

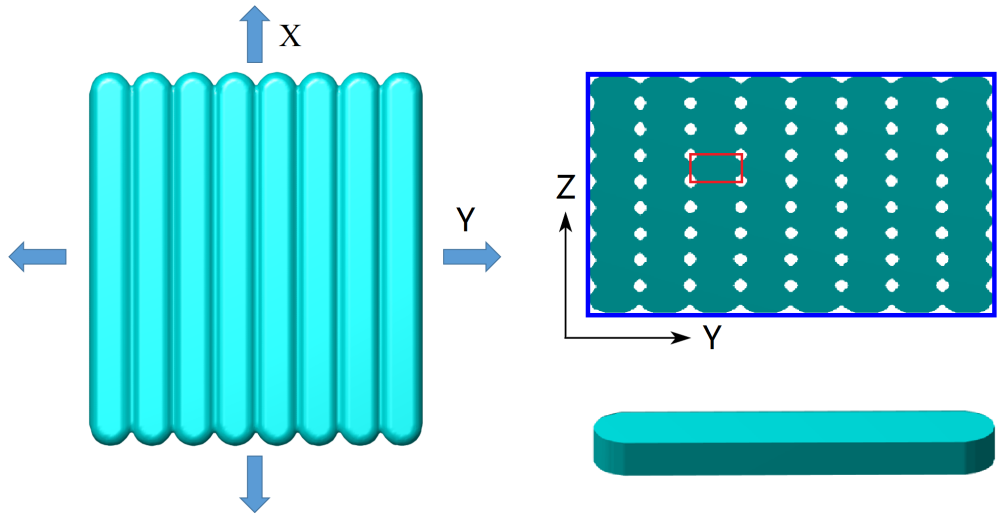

Figure 5.3: The material properties of printed structure are measured on a specimen formed by a uniform pattern of parallel roads. Left: tensile tests are performed along X and Y directions. Right top: the cross-section of the specimen. The blue rectangle indicates an effective domain of the measurement. The red rectangle indicates an effective cross-section of a road that is compatible with the assumptions in the measurement. Right bottom: reinterpreted geometry of a single road.

5.3 (middle) where they are assumed to be constant. Clearly, these measured properties cannot be applied directly to the idealized geometry model constructed from a number of roads with arbitrary orientation and spacing.

It should now be clear that the effective geometry and material models of the FDM structures are interdependent and cannot be treated separately. The difficulty is that this interdependence is implicit in the (inconsistent) assumptions underlying the geometric model and material measurement procedures, but it cannot be used explicitly to express either model in terms of the other. Hence, we propose to simultaneously modify *both* models of geometry and of material, in order to bring them into the agreement and construct a consistent effective geometry-material model.

First, the idealized road shown in Figure 5.1 is *reinterpreted* with a rectangular cross-section shown at the bottom of Figure 5.3. This reinterpretation is consistent with the material measurement process that assumes the effective rectangular cross-section of the specimen shown in Figure 5.3 does not have any voids. Secondly, because the measurement specimen is a periodic arrangement of

parallel roads, the measurement procedure implies that the measured material properties remain constant and are identical on the cross-section of each individual road. This means that the measured anisotropic material properties can now be assigned based on the reinterpreted geometry and the direction of the road, while eliminating the need to model air gaps and bonding stiffness.[1]

Next, we transform the measured material properties to be consistent with the direction of individual roads. The material properties are measured in a coordinate system with z axis pointing in the build direction and x axis aligned with the (stiffest) direction of the roads in the specimen. The measurement results are generally represented by the following transverse isotropic compliance tensor:

$$S = \begin{bmatrix} \frac{1}{E_x} & -\frac{\nu_{xp}}{E_x} & -\frac{\nu_{xp}}{E_x} & 0 & 0 & 0 \\ -\frac{\nu_{xp}}{E_x} & \frac{1}{E_p} & -\frac{\nu_p}{E_p} & 0 & 0 & 0 \\ -\frac{\nu_{xp}}{E_x} & -\frac{\nu_p}{E_p} & \frac{1}{E_p} & 0 & 0 & 0 \\ 0 & 0 & 0 & \frac{1+\nu_p}{E_p} & 0 & 0 \\ 0 & 0 & 0 & 0 & \frac{1}{2G_{xp}} & 0 \\ 0 & 0 & 0 & 0 & 0 & \frac{1}{2G_{xp}} \end{bmatrix}, \tag{5.27}$$

where E_p, ν_p and E_x, ν_x are Young's moduli and Poisson ratios in the $y-z$ symmetry plane and x-direction, respectively. G_{xp} is the shear modulus in the x-direction. The elasticity tensor C is calculated as the inverse of the compliance tensor S. Note that $y-z$ is the symmetry plane, which is different from the usual convention that $x-y$ is the symmetry plane.

The roads can be printed along any direction within the layer while remaining perpendicular to the build direction. To align the x axis of measurement with the road direction, this fourth-order elasticity tensor must be rotated within the layer [131]:

$$C'_{mnop} = R_{mi}R_{nj}R_{ok}R_{pl}C_{ijkl}, \tag{5.28}$$

[1] Printing defects such as imperfect bonding must be treated separately with thermal history models, which is outside the scope of the current discussion.

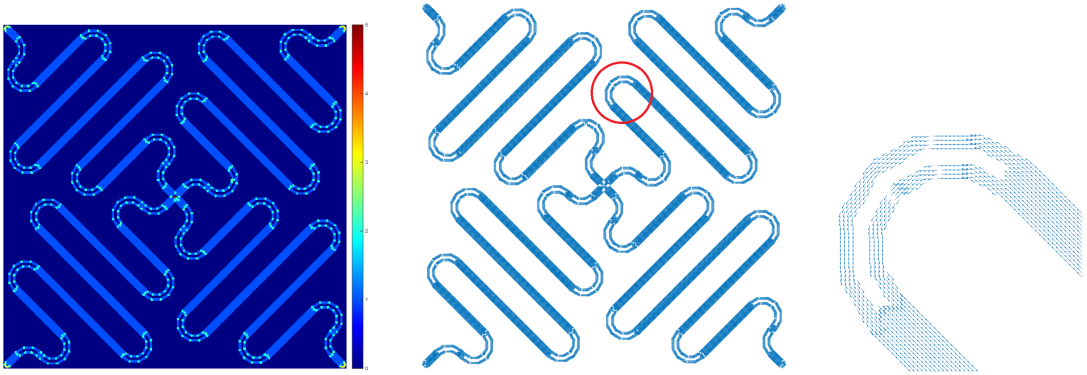

(a) Discretized first layer. The number of roads each query point belongs to is color coded. The averaged material property is returned if the query point belongs to more than one road.

(b) The stiffest direction of material tensor for each query point.

(c) The zoomed in view of (b).

Figure 5.4: Material distribution of printed model for a two-dimensional infill pattern.

where R_{ij} is the ij-th component of R:

$$R = \begin{bmatrix} \cos\theta & -\sin\theta & 0 \\ \sin\theta & \cos\theta & 0 \\ 0 & 0 & 1 \end{bmatrix}, \tag{5.29}$$

and θ is the angle between the x axis and the road direction. Figure 5.4 shows the result of aligning the material tensor with the directions of the roads within a single layer. Here, the stiffest direction of the elasticity tensor is sampled at different locations and is plotted as a vector field.

One final modification of material model is required to account for areas where multiple roads overlap. In such cases, the elasticity tensor is simply averaged over all overlapping roads. For example, if the overlap is between two parallel roads, the elasticity tensor remains the same as in both roads. If two roads form a T-section, the returned elasticity tensor becomes isotropic in the plane of the layer after averaging from the two roads.

The mesoscale geometry-material model is conveniently represented by extending the implicit

sweep-based representation of the idealized printed geometry. The point membership of a given query point against such a representation is determined by its point membership against the MMV centered at its nearest point on the toolpath.

The same implicit representation is adapted and reinterpreted to be consistent with the proposed effective geometry - material model. A transformed material tensor is associated with every road. When a material tensor is queried at a point, both the point and the relevant roads are simply projected onto the horizontal $x - y$ plane of the layer (perpendicular to the build direction). The two-dimensional point membership classification against the projected road effectively eliminates the air gaps between the adjacent bonded roads, while other voids within the layers can still be recovered. This implicit representation of the effective mesoscale geometry-material model is sufficient for many downstream applications; in particular, it forms the input for the macro scale homogenization stage discussed in the next section.

5.3.2 Comparison with finite element method

A voxelized finite element mesh of the mesoscale geometry-material printed model is created by every query point within the effective material domain as a linear element with 8 nodes. The output of FEA analysis is the nodal displacement field. The strain field can be derived by differentiating the displacement field numerically. Numerical differentiation is sensitive to the noise and may generate erroneous results. Instead, we compute the averaged strain and stress through the displacement and traction on the boundary of the material domain directly based on the following equations:

$$\overline{\epsilon}_{ij} := \frac{1}{|\Omega|}\int_{\Omega} \epsilon_{ij}(x)\, dx = \frac{1}{|\Omega|}\int_{\partial\Omega} \frac{1}{2}(u_i n_j + u_j n_i)\, dS,$$
$$\overline{\sigma}_{ij} := \frac{1}{|\Omega|}\int_{\Omega} \sigma_{ij}(x)\, dx = \frac{1}{|\Omega|}\int_{\partial\Omega} \frac{1}{2}(t_i x_j + t_j x_i)\, dS,$$

where Ω is the material domain and $\partial\Omega$ is its boundary. Equation (2.6) follows immediately from the divergence theorem.

A fictitious isotropic material with Young's modulus $E = 1$ GPa and Poisson's ratio $\nu = 0.3$ is assigned to the 2D infill pattern shown in Figure 5.2. The input material elasticity tensor field has a resolution of $296 \times 296 \times 16$ and is generated from the printed mesoscale model proposed in Section 5.3.1. A soft material ($E = 0.01$ GPa) is assigned to the void phase as the stiffness matrix in FEM becomes ill-conditioned with elements of zero stiffness. The reference material for the proposed homogenization method has Young's modulus $E = 1.5$ GPa and Poisson's ratio $\nu = 0.3$ so that the linear system remains positive definite. The effective elasticity tensors C^{eff} and C^{fem} computed respectively by the proposed homogenization method and the FEM-based method are:

$$
\begin{aligned}
C^{\text{eff}} &= \begin{bmatrix} 0.0327 & 0.0150 & 0.0139 & 0 & 0 & 0 \\ 0.0150 & 0.0327 & 0.0139 & 0 & 0 & 0 \\ 0.0139 & 0.0139 & 0.3335 & 0 & 0 & 0 \\ 0 & 0 & 0 & 0.0338 & 0 & 0 \\ 0 & 0 & 0 & 0 & 0.0338 & 0 \\ 0 & 0 & 0 & 0 & 0 & 0.0254 \end{bmatrix} \\
C^{\text{fem}} &= \begin{bmatrix} 0.0330 & 0.0141 & 0.0132 & 0 & 0 & 0 \\ 0.0138 & 0.0330 & 0.0129 & 0 & 0 & 0 \\ 0.0151 & 0.0151 & 0.4234 & 0 & 0 & 0 \\ 0 & 0 & 0 & 0.0227 & 0.0005 & 0 \\ 0 & 0 & 0 & 0.0005 & 0.0227 & 0 \\ 0 & 0 & 0 & 0 & 0 & 0.0235 \end{bmatrix}
\end{aligned}
\tag{5.30}
$$

The in-plane symmetry of the structure is reflected in the simulated result as $C^{\text{eff}}_{11} = C^{\text{eff}}_{22}$ and $C^{\text{eff}}_{13} = C^{\text{eff}}_{23}$. The homogenization also captures the in-plane spring-like behavior, which is about 10 times less stiff in the x and y directions than the z direction. We attribute the small difference between C^{eff} and C^{fem} to the different boundary conditions used. In FEM, a simple uniform displacement boundary condition is used since the Lagrange multipliers are required to apply the periodic boundary condition in FEM [146]. Both the proposed homogenization method and FEM are implemented in MATLAB. To homogenize the example in Figure 5.2, homogenization using Green's function took less than 3 hours to converge while the FEM required more than 24 hours on an Intel i7 computer with 16 gigabytes memory.

5.3.3 Comparison with physical tests

We also compare the predicted homogenization results with the physically measured effective tensile modulus reported in [140]. The samples for the physical testing are shown in Figure 5.5.

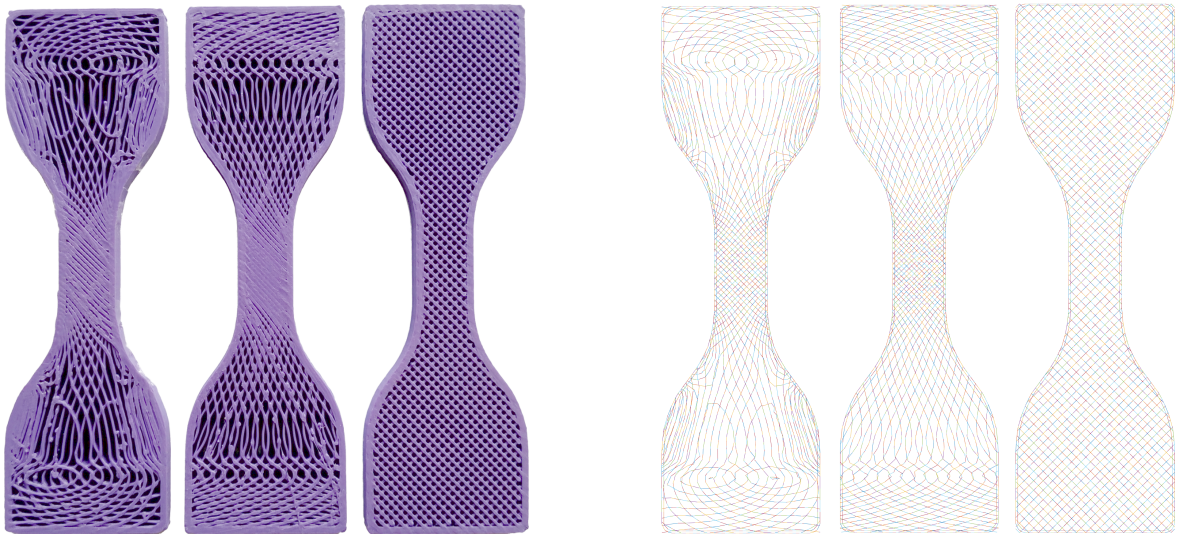

Figure 5.5: The FDM printed tensile test specimens. Left: from left to right, infill pattern A, infill pattern B and linear infill pattern. Right: the G-codes for the first two layers. Images of printed parts courtesy of [140].

During the tensile test, only displacements in the central neck region are measured for the evaluation of the effective tensile modulus of specimen. For comparison with the results of physical testing, the neck regions were reconstructed from the G-code and homogenized by the proposed approach.

The filament used for the FDM printing is ABS plastic made by Airwolf3D with measured diameter 2.82 mm and tensile modulus 2.25 GPa. The layer height is explicitly known from the G-code. However, the road width still needs to be computed from the G-code based on the conservation of volume if such information is not explicitly given. We estimate that the road width is roughly 0.6 mm. With the distance between parallel roads being 0.4 mm, this results in an overfill that eliminates most of the air gaps in regions of solid infills, such as the contour regions close to the boundary the specimen. Based on this observation, the axial stiffness E_x is estimated as almost identical to the stiffness of the filament and the transverse stiffness E_p is about 80% to 90% of the filament stiffness. Based on the experiment results in [88], the Poisson's ratio ν_{xp} and ν_p in the transverse isotropic elasticity tensor (Equation 5.27) are both set to be 0.39 and G_{xp} is set to be 1.6

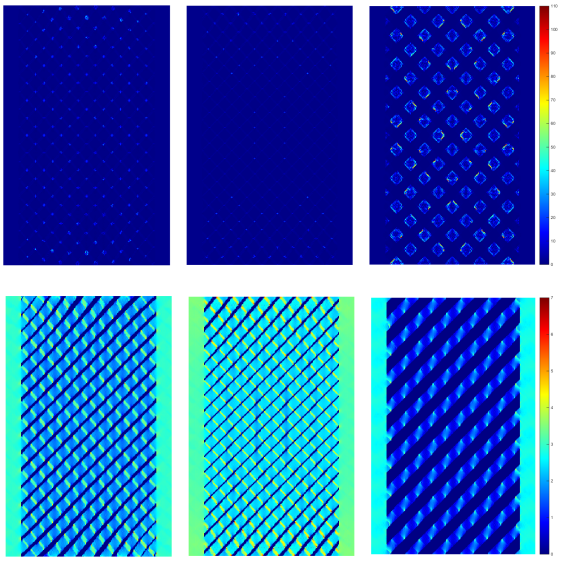

Figure 5.6: The strain and stress distributions in first layer of the homogenized regions with the displacement boundary condition along the vertical direction (x axis) of the specimen. Top row: absolute value of ϵ_x. Bottom row: absolute value of σ_x.

GPa.

The homogenized effective elasticity tensor is not directly comparable to the tensile testing result. For example, the homogenized elasticity tensor of Infill B with $E_x = 2.25$ GPa and $E_p = 1.8$ GPa is

$$\begin{bmatrix} 2.4166 & 1.1825 & 1.0978 & -0.0000 & -0.0001 & 0.0003 \\ 1.1826 & 2.2511 & 1.0561 & -0.0001 & -0.0000 & 0.0005 \\ 1.0977 & 1.0559 & 2.0888 & -0.0001 & -0.0001 & 0.0001 \\ -0.0000 & -0.0001 & -0.0001 & 0.9174 & -0.0003 & -0.0000 \\ -0.0001 & -0.0000 & -0.0001 & -0.0003 & 0.9977 & -0.0000 \\ 0.0003 & 0.0005 & 0.0001 & -0.0000 & -0.0000 & 1.2634 \end{bmatrix} \tag{5.31}$$

To compute the tensile modulus along the x, y, and z directions, we assume that the homogenized structures are orthotropic. In this particular set of examples, such assumption is reasonable given the normal and shear components in the homogenized effective elasticity tensor are essentially not coupled. The tensile modulus along the axial directions can be computed with the orthotropic

compliance tensor S:

$$S = \begin{bmatrix} \frac{1}{E_x} & -\frac{\nu_{yx}}{E_y} & -\frac{\nu_{zx}}{E_z} & 0 & 0 & 0 \\ -\frac{\nu_{xy}}{E_x} & \frac{1}{E_y} & -\frac{\nu_{zy}}{E_z} & 0 & 0 & 0 \\ -\frac{\nu_{xz}}{E_x} & -\frac{\nu_{yz}}{E_y} & \frac{1}{E_z} & 0 & 0 & 0 \\ 0 & 0 & 0 & \frac{1}{2G_{yz}} & 0 & 0 \\ 0 & 0 & 0 & 0 & \frac{1}{2G_{zx}} & 0 \\ 0 & 0 & 0 & 0 & 0 & \frac{1}{2G_{xy}} \end{bmatrix}.$$

It is clear that $E_x = \frac{1}{S_{11}}$, $E_y = \frac{1}{S_{22}}$, and $E_z = \frac{1}{S_{33}}$.

The measured and homogenized tensile moduli are reported in Table 5.1 with different stiffness in the transverse directions. The stress - strain curves for physical tests on different specimens are shown in Figure 5.7. We observe that the homogenized tensile moduli are smaller than the measured ones for Infill B and the linear infill. We believe this is due to the distance between the parallel roads being less than the road width. For example, the thickness of the vertical walls on the side of the infill pattern is reconstructed as 1 mm gives the 0.6 mm road width and 0.4 mm distance between the parallel toolpathes. However, the actual thickness of the walls of the printed parts is about 1.2 mm. The proposed printed model does not preserve the volume of the filament and underestimate the volume of the material in the printed part with overfills. Since the G-code generator used in [140] is custom-built to study the effects of different infill patterns, the overfill is less likely to happen in most of the established process planning procedures. We also observed that the measured modulus of Infill A is around the midpoint of Infill B and linear infill. Even though our predicted modulus for infill A is higher than the measured result, it agrees with the stress - strain curve shown in Figure 5.7, in which the tensile moduli for Infill A and B are much closer.

Table 5.1: The measured and homogenized tensile modulus by the proposed method. The first row shows the measured modulus (GPa) in [140]. The rest of the rows show the simulated modulus with $E_x = 2.25$ GPa and different stiffness in the transverse direction. E_p and E_x are material coefficients of the transverse isotropic material tensor (Equation 5.27).

	Infill A	Infill B	Linear
Measured modulus [140]	1.24	1.71	0.79
$E_p/E_x = 1$	1.4201	1.6769	0.7245
$E_p/E_x = 0.9$	1.3904	1.6396	0.7142
$E_p/E_x = 0.8$	1.3674	1.6103	0.7059
$E_p/E_x = 0.7$	1.3422	1.5784	0.6968

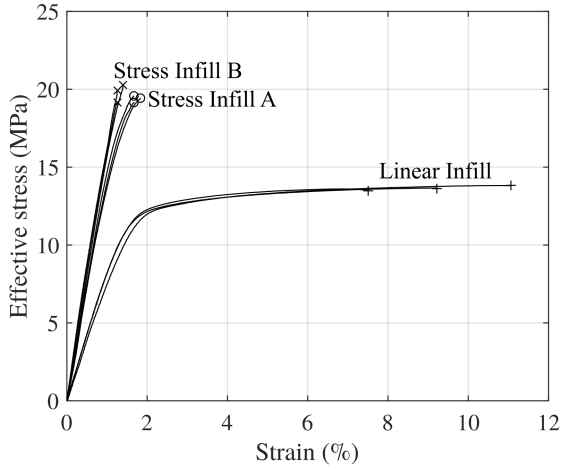

Figure 5.7: The stress - strain curve of physical testing result. Image courtesy of [140].

5.4 Discussion

In the current chapter, we showed the estimation of mechanical properties through correlation functions. We adopted and significantly improved the homogenization method using Green's function, showing that the corresponding linear system is symmetric and positive definite, and can be efficiently solved by the conjugate gradient method with matrix-vector multiplication evaluated in the frequency domain. To compare the computational results with physical tests, we we formulated and constructed an implicit representation of an effective mesoscale geometry-material model of the printed structure that captures the heterogeneity and anisotropy resulting from the printing

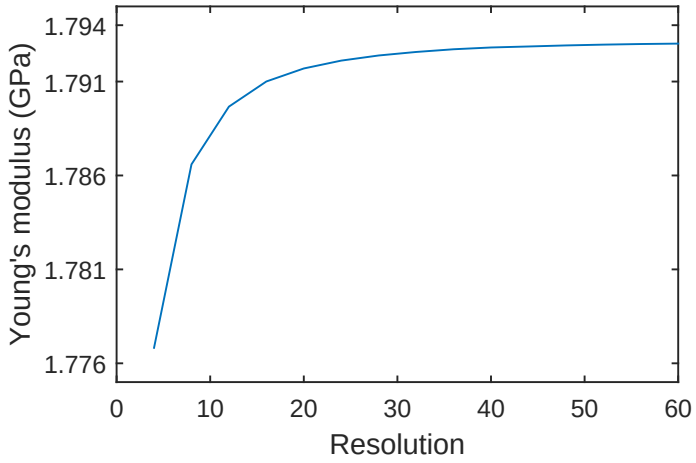

Figure 5.8: The change of effective Young's modulus with different sampling resolutions. Lower resolutions lead to the approximation errors on the Green's operator Γ.

process. We then showed how this implicit representation of the mesoscale model may be queried and homogenized at macro scale in order to predict the effective material properties of the printed structure that accounts for build orientation, directional changes, infill patterns and other mesoscale details of 3D printing. The predicted effective material properties are in good agreement with known experimental results and with the homogenization results predicted by the finite element method.

The proposed method to estimating effective material properties is not limited to linear elasticity: similar homogenization technique applies to thermal and electrical conductivity, dielectric constant, permeability, and other material properties that share the same general form as the linear elasticity tensor.

Numerical properties of the proposed homogenization method deserve further investigation. For example, the behavior of the preconditioner δC is not fully understood, and the condition number of the linear system has not yet been studied. Furthermore, homogenization process involves discretization errors in the implicit representation of printed roads, requires setting tolerances for convergence, and introduces discretization error of the Green's operator. Among these sources of

errors, the last one in particular deserves further study. Since the Green's operator is derived and evaluated in the frequency domain, higher frequencies are lost at a low sampling resolution. Figure 5.8 plots the effective Young's modulus (of the same structure) at different sampling resolutions.

Chapter 6

Material structure design with varying neighborhood orientations

Anisotropy of material refers to the dependence of material's properties on direction. Anisotropy should not be confused with heterogeneity, which is the property of being location dependent. A material can be homogeneous on the coarse scale and have its fine-scale structures being anisotropic at the same time, as is the case, for example, with carbon fiber sheets in composite manufacturing. Similar to heterogeneity, anisotropy is a property of scales, depending on the effective material property of the associated neighborhood. Many nature and man-made materials exhibit various degrees of anisotropy. For example, crystalline materials are generally anisotropic, as many of their physical properties depend on the direction of the crystal. Wood is anisotropic with a high percentage of grains parallel to the tree trunk. The fine scale structures of bones are anisotropic with internal architecture of the trabeculae adapting to the loads, making bones more efficient given the competing constraints in nature.

The term anisotropy is overloaded in the context of material structures. Depending on how it is measured, it could refer to **geometry anisotropy**, where the statistics of the structural geometry is anisotropic; it could also refer to **property anisotropy**, where the physical properties of the material

are anisotropic. It is widely accepted that the latter is the result of the former combined with the third type of anisotropy: the material anisotropy of the constituent phases of the fine scale material structure, which can be regarded as the property anisotropy from a finer scale. This also suggests that property anisotropy at the course scale can be controlled locally by rotation of the fine-scale structure, which is the orientation control mechanism adopted in the present work.

Mankind has relied on and benefited from material anisotropy for many centuries, from using the ancient combination of straw and mud to form brick for building construction to modern day prestressed concrete and fibrous composites [108]. Even though the mechanism is straightforward, most of the fine-scale structures controlling the property anisotropy of the man-made materials to date can be reasonably characterized as one-dimensional, e.g. rebar in the concrete, fiber in the composite. This is partly due to the difficulties involved in the characterization of property anisotropy of 3D material structures, and partly due to inherent complexity of the design and manufacturing of three-dimensional multiscale structures [147]. The rapid advancement of additive manufacturing technologies eliminates many of the geometric restrictions in traditional subtractive manufacturing processes, enabling the fabrication of three-dimensional multiscale structures in place of traditional solid parts. The goal of this chapter is to propose a computational framework that facilitates the design of two-scale material structures with anisotropic properties at coarse scale controlled by geometric synthesis at the fine scale.

We propose a sample-based approach to synthesis of two-scale structures while controlling the spatial orientation of the anisotropic material properties at the coarse scale (see Figure 6.1). In Section 6.1.4, an automatic way to determine the orientation of the material property anisotropy directly from the elasticity tensor of an orthotropic material is proposed (Figure 6.1c). This is done by first converting the 4th-rank elasticity tensor into the 6 by 6 matrix form with Mandel notation and calculating the eigenvalues and eigenvectors of the matrix with the commonly available tools. We then compute the principal strains of the dominant strain vector with another eigenvalue decomposition after converting the strain vector back into the tensor form. We prove that resultant

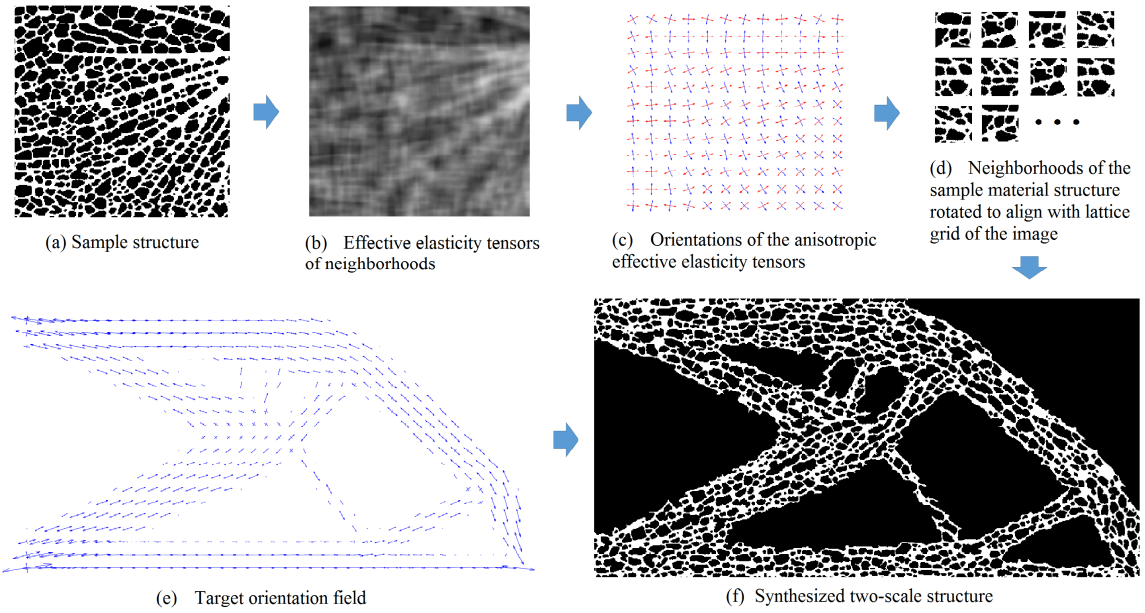

Figure 6.1: The pipeline of the proposed two-scale structure synthesis method. (a) is the input sample structure. (b) is the field of effective elasticity tensor of fine-scale structures in (a). (c) is the field of principal axes of the effective elasticity tensor with the assumption of orthography. (d) is the collection of fine-scale structures in (a) which are rotated to align with the lattice grid of the image. (e) is the input target orientation field that may be defined by the user or from an optimization routine. (f) is the final result of the synthesized two-scale structure. (b) and (d) are for illustrations purpose only.

directions of principal strains are the principal axes of the orthotropic material.

For sample structures with non-uniform orientations, multiple boundary value problems may need to be solved for the coarse scale effective material properties to characterize the spatial orientation distribution of material anisotropy. In Section 6.2, we efficiently estimate the effective elasticity tensors of fine-scale structures based on their two-point correlation functions (Figure 6.1b). A significant speed-up is observed without sacrificing the accuracy of the spatial orientation distribution of the fine-scale structures.

In Section 6.3, we develop and implement texture synthesis techniques to generate the two-scale structures whose material anisotropies follow target orientation fields prescribed on the coarse scale. First, the principal axes of the fine-scale structures in the sample are aligned with directions

of the image lattice grid (Figure 6.1d). This step is a necessary addition to the traditional texture synthesis algorithms where the orientation of the sample structure is often assumed to be constant. Then the new two-scale structure is synthesized by rotating these fine-scale structures to align with the target orientation field (Figure 6.1e). Gaussian pyramid and correction subpasses are engaged to parallelize the algorithm. The effectiveness of the proposed approach is demonstrated through examples. Some results in this chapter has been reported in [82].

6.1 Orientation of an anisotropic material

Various existing ways to characterize the anisotropy of material structures have been reviewed in Chapter 2. One common drawback they share is the lack of direct connection to the physical properties of interest. In this section, we identify the orientation of a material directly from its elasticity tensor - the material property of interest in the present chapter. We note that the proposed method also applies to other tensorial properties, such as thermal and electrical conductivity. We define the orientation of a material by the directions of its principal axes. For orthotropic material, principal axes of material are defined as the three orthogonal directions where three planes of symmetry meet [44]. We generalize the definition of principal axes to other anisotropic materials in Section 6.1.4. To find the principal axes of a material, the following conjecture is made:

> *The principal axes of an orthotropic material coincide with the principal directions of the strain, which is the dominant eigentensor (eigentensor associated with the largest eigenvalue) of the material's elasticity tensor if such principal directions are uniquely defined.*

The eigentensor of a fourth-rank tensor is defined by Mehrabadi and Cowin [99]: "The eigenvectors of the 3-dimensional fourth-rank anisotropic elasticity tensor, considered as a second-rank tensor in a 6-dimensional space, are called eigentensor when projected back into the 3-dimensional space."

We say the principal directions of a strain tensor are uniquely defined when the strain is not isotropic or transverse isotropic, i.e. the three principal strains all have different numeric values.

We choose Mandel notation as 6×6 matrix representation of the fourth-rank elasticity tensor. The advantage of Mandel notation over Voigt notation is explained in [118]. We include a brief discussion on the Eigen decomposition of the elasticity tensor before proving the conjecture in 2D. The discussion may be obvious to some researchers and unknown to others, and therefore is included.

6.1.1 Eigen decomposition of the elasticity tensor

Eigen decomposition of elasticity tensor was first studied by Lord Kelvin [85], who determined the eigentensor of a fourth-rank tensor in 3-dimensional space by the eigenvectors of the second-rank tensor in 6-dimensional space. Since the eigenvectors of elasticity tensor in Mandel notation are strains, we refer to them as strain eigentensor and to corresponding stress vector as stress eigentensor. The properties of strain and stress eigentensors follow the general properties of eigenvectors regardless of the material symmetry. For example, the stress and strain can be decomposed into a sum of six or fewer eigentensors. And the stress eigentensor is proportional to its strain eigentensor. We also note that dominant strain eigentensor is the unit strain that maximize the strain energy, hence the efficiency, of the material.

Kelvin determined the eigenstrains for many material symmetries and summarized his results in Encyclopaedia Britannica. We give a brief summary of his results here. Readers may refer [99] for a detailed review. For materials with isotropic and cubic symmetries, only two and three distinct eigenvalues were found, respectively. Four different eigenvalues were found for materials with transverse isotropic and hexagonal symmetries. Five different eigenvalues exist for materials with tetragonal symmetry. Only materials with orthotropic symmetry and no general symmetries have all six different eigenvalues. We observe that the largest eigenvalue of the elasticity tensor always has the multiplicity of one, meaning the eigentensor maximizing the strain energy is uniquely defined unless the strain is isotropic or transverse isotropic. In the latter case, the number of strains to maximize the strain energy is infinite. Next, we will discuss how to predict the principal orientation

of the material based on the largest eigenvalue and corresponding strain eigentensor with the assumption of orthotropic symmetry.

6.1.2 Proof of the conjecture in 2D

The proof of the conjecture consists of two steps. In the first step, we study the optimal orientation of the material for a given unit strain. We first calculate the strain energy which is a function of the relative orientation between the material and the given strain. We then show that the alignment of the principal orientation of material and principal directions of the given strain is one of the potential stationary points when maximizing or minimizing the strain energy. This first step is inspired by the work of Cheng and Pedersen [22].

In the second step, we show that other potential stationary points will not become actual stationary points when the given strain eigentensor has the potential to maximizes the strain energy among all possible unit strains. Therefore the principal orientation of the material is aligned with the principal directions of the dominant eigentensor.

The following is the detailed proof of the conjecture in 2D. The elasticity tensor of 2D orthotropic material, when its principal orientation coincides with the reference coordinate system, takes the form:

$$C = \begin{bmatrix} C_{11} & C_{12} & 0 \\ C_{12} & C_{22} & 0 \\ 0 & 0 & C_{33} \end{bmatrix}$$

For a given strain ϵ, let θ be the angle between the principal orientation of the orthotropic material and the principal directions of the strain. The rotation matrix in Mandel notation is:

$$R = \begin{bmatrix} c^2 & -s^2 & -\sqrt{2}cs \\ s^2 & c^2 & \sqrt{2}cs \\ \sqrt{2}cs & -\sqrt{2}cs & -2s^2 \end{bmatrix}$$

where $c = cos(\theta)$ and $s = sin(\theta)$. For different relative orientations θ, the strain energy is calculated:

$$\begin{aligned} U =& \epsilon^T R C R^T \epsilon \\ =& (\epsilon_1 c^2 + \epsilon_2 s^2)^2 C_{11} + (\epsilon_2 c^2 + \epsilon_1 s^2)^2 C_{22} + \\ & 2(\epsilon_2 c^2 + \epsilon_1 s^2)(\epsilon_1 c^2 + \epsilon_2 s^2) C_{12} + 2c^2 s^2 (\epsilon_1 - \epsilon_2)^2 C_{33} \end{aligned}$$

where $\epsilon = [\epsilon_1, \epsilon_2, 0]^T$ is the given strain in its principal directions.

To maximize or minimize the strain energy, we shall evaluate its derivatives. The partial derivative of U for a given strain with respect to θ is:

$$\begin{aligned} \frac{\partial U}{\partial \theta} &= \epsilon^T \frac{\partial R}{\partial \theta} C R^T \epsilon + \epsilon^T R C \frac{\partial R}{\theta}^T \epsilon = 2\epsilon^T \frac{\partial R}{\theta} C R^T \epsilon \\ &= -2sin(2\theta)(\epsilon_1 - \epsilon_2)[cos(2\theta)(\epsilon_1 - \epsilon_2)(C_{11} - 2C_{12} \\ &\quad + C_{22} - 2C_{33}) + C_{11}(\epsilon_1 + \epsilon_2) - C_{22}(\epsilon_1 - \epsilon_2)] \end{aligned}$$

Let $\partial U / \partial \theta = 0$, we have the following solutions:

$$\theta = 0^\circ \text{ or } 90^\circ \tag{6.1}$$

$$\theta = \pm \frac{1}{2} arccos[\frac{C_{11}(\epsilon_1 + \epsilon_2) - C_{22}(\epsilon_1 - \epsilon_2)}{(\epsilon_1 - \epsilon_2)(C_{11} - 2C_{12} + C_{22} - 2C_{33})}] \tag{6.2}$$

where the first solution (Equation 6.1) implies alignment of the principal strain and the principal orientation of orthotropic material, the second solution (Equation 6.2) is a non-trivial high shear case and is not always feasible [22]. It is straightforward to show that the 0° alignment renders a higher strain energy than the 90° alignment. However, it is less straightforward to show the existence of the second solution and when it maximize or minimize the strain energy. Of course, none of these would matter if the given strain were isotropic and the derivative of U were always 0.

Nonetheless, to prove our conjecture, we only need to show that the second solution is not

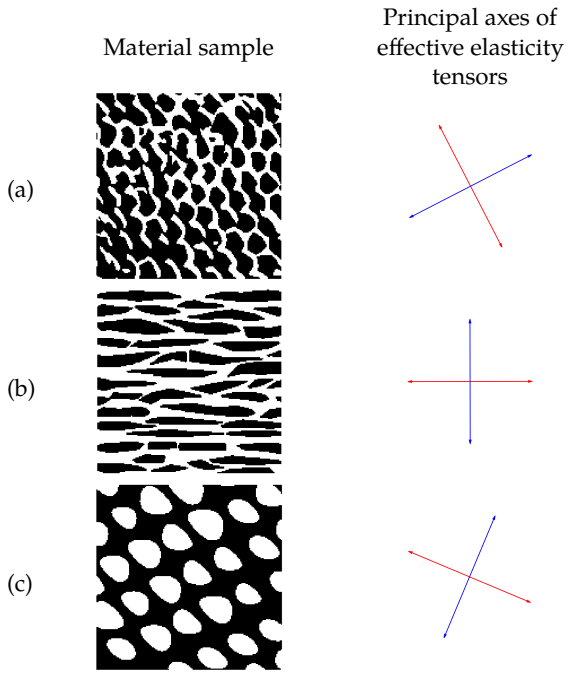

Figure 6.2: The principal axes of the effective elasticity tensors of 2D sample material structures. Red and blue arrows represent the major and minor axes, respectively. The median axes are represented in blude arrows. Young's modulus and Poisson's ratio, $E = 1$ MPa, $\nu = 0.3$ and $E = 0.02$ MPa, $\nu = 0.3$ are assigned to the white and black phases, respectively.

feasible when the given strain is the dominant strain eigentensor of the material's elasticity tensor. Recall that the largest eigenvalue of the elasticity tensor does not repeat itself, meaning that the unit strain to maximize the strain energy is always uniquely defined (except for the isotropic strain, as shown both in the third solution and in Table 6.1). Since U is an even function of θ, the two results in the second solution inevitably lead to the same strain energy, which contradicts the uniqueness of the largest eigenvalue. As a result, the second solution is not feasible when the given strain is the dominant eigentensor and therefore the principal orientation of an orthotropic material coincides with the principal directions of the given strain. This concludes the proof in 2D.

6.1.3 Discussion for 3D cases

Due to the number of terms involved, we were not able to give a close form solution of the relative orientation to maximize or minimize the strain energy in 3D as we did in 2D. However, we were able to verify that α , β , $\gamma \in \{0°, 90°\}$, Tait - Bryan angles representing the relative orientations between the principal directions of the given strain and principal axes of the orthotropic material, are stationary points for the strain energy.

The elasticity tensor of 3D orthotropic material, when its principal orientation coincides with the reference coordinate system, takes the form:

$$\begin{bmatrix} C_{11} & C_{12} & C_{13} & 0 & 0 & 0 \\ C_{12} & C_{22} & C_{23} & 0 & 0 & 0 \\ C_{13} & C_{23} & C_{33} & 0 & 0 & 0 \\ 0 & 0 & 0 & C_{44} & 0 & 0 \\ 0 & 0 & 0 & 0 & C_{55} & 0 \\ 0 & 0 & 0 & 0 & 0 & C_{66} \end{bmatrix}$$

Just like in 2D case, the strain energy may be calculated for different relative orientations:

$$U = \epsilon^T R C R^T \epsilon$$

where R is the rotation matrix in Mandel notation mapped from the tensor notation with the form:

$$\begin{bmatrix} 1 & 0 & 0 \\ 0 & \cos(\gamma) & -\sin(\gamma) \\ 0 & \sin(\gamma) & \cos(\gamma) \end{bmatrix} \begin{bmatrix} \cos(\beta) & 0 & \sin(\beta) \\ 0 & 1 & 0 \\ -\sin(\beta) & 0 & \cos(\beta) \end{bmatrix} \begin{bmatrix} \cos(\alpha) & -\sin(\alpha) & 0 \\ \sin(\alpha) & \cos(\alpha) & 0 \\ 0 & 0 & 1 \end{bmatrix}$$

It is easy to verify in MATLAB that α , β , $\gamma \in \{0°, 90°\}$ are indeed stationary points for the strain energy. These observations, together with the proof in 2D, lead us to conjecture that the proposed

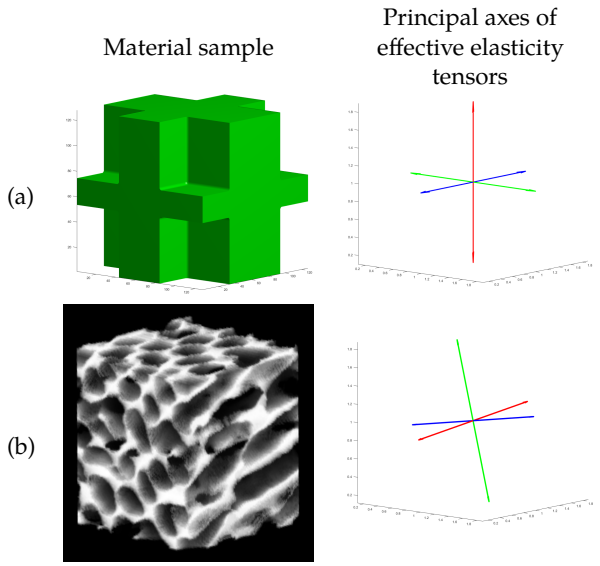

Figure 6.3: The principal axes of the effective elasticity tensors of 3D sample material structures. Red and blue arrows represent the major and minor axes, respectively. Young's modulus and Poisson's ratio, $E = 1$ MPa, $\nu = 0.3$ and $E = 0.02$ MPa, $\nu = 0.3$ are assigned to the white and black phases, respectively.

method is also applicable in 3D.

6.1.4 Principal axes of an anisotropic material

Most anisotropic materials are not perfectly orthotropic: some materials are only approximately orthotropic while others may share other type of material symmetry, e.g. triclinic, or no symmetry at all. Yet the proposed method to identify the three orthogonal axes still applies as the Eigen decomposition of the elasticity tensor does not assume any material symmetries. We define these three orthogonal axes as the principal axes of the material, which represents the principal directions of the unit strain maximizing the strain energy. This generalization allows us to define the orientation of anisotropic materials.

Figure 6.2 shows the principal axes of the effective elasticity tensors of the sample materials. Young's modulus and Poisson's ratio, $E = 1$ MPa, $\nu = 0.3$ and $E = 0.02$ MPa, $\nu = 0.3$ are assigned

to the white and black phases, respectively. Our efficient method of estimating effective elasticity tensors will be discussed in the next section. What's worth to note is that the orientation of Figure 6.2 (c) does not correspond to the pattern in the structure by direct visual examination. However, the pattern becomes clear if lines parallel to the predicted major axis are drawn over the sample material.

Figure 6.3 shows two examples of the algorithm in 3D. Same as the 2D examples, Young's modulus and Poisson's ratio, $E = 1$ MPa, $\nu = 0.3$ and $E = 0.02$ MPa, $\nu = 0.3$ are assigned to the white and black phases, respectively. In the first example, the major and minor axes align with the directions with most and least cross-section areas, therefore the stiffest and softest directions, respectively. In the second example, the major axis aligns with the direction of the pore and the directions of the minor and median axes capture the shape of the pore.

6.1.5 Limitation

One limitation of the algorithm is that the principal axes of the material cannot be completely determined if the directions of the principal strain or stress are not fully determined, i.e. two or more of the principal strains or stresses are identical. Table 6.1 shows effective stiffness, its largest eigenvalue and dominant eigenvector of the same material structure rotated at 0, 30, and 45 degrees. Ignoring the discretization errors, every strain tensor maximizing the strain energy having identical principal strains in X-Y plane demonstrates that the proposed algorithm can not detect the principal axes for this particular material structure. In addition, the three material structures sharing the same eigenvectors further reflects this limitation. We believe this usually happens when the material structure is isotropic or shows certain symmetries and expect this scenario less likely to happen with random heterogeneous materials.

Table 6.1: Effective stiffness, its largest eigenvalue and associated eigenvector of the same material structure rotated at 0, 30, and 45 degrees. Ignoring the discretization errors, every strain tensor maximizing the strain energy having identical principal strains in X-Y plane demonstrates that the proposed algorithm can not detect the principal axes for this particular material structure. Young's modulus and Poisson's ratio, $E = 1$ MPa, $\nu = 0.3$ and $E = 0.02$ MPa, $\nu = 0.3$ are assigned to the white and black phases, respectively.

Material structure	Effective stiffness tensor	Largest eigenvalue	Eigenvector
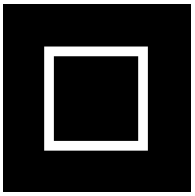	$\begin{bmatrix} 0.1982 & 0.0706 & 0.0806 & 0 & 0 & 0 \\ 0.0706 & 0.1982 & 0.0806 & 0 & 0 & 0 \\ 0.0806 & 0.0806 & 0.2421 & 0 & 0 & 0 \\ 0 & 0 & 0 & 0.1200 & 0 & 0 \\ 0 & 0 & 0 & 0 & 0.1200 & 0 \\ 0 & 0 & 0 & 0 & 0 & 0.0958 \end{bmatrix}$	0.3703	$\begin{bmatrix} 0.5283 \\ 0.5281 \\ 0.6648 \\ 0 \\ 0 \\ 0 \end{bmatrix}$
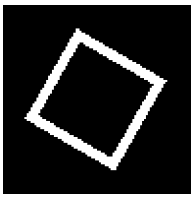	$\begin{bmatrix} 0.1874 & 0.0814 & 0.0806 & 0 & 0 & -0.0087 \\ 0.0814 & 0.1873 & 0.0806 & 0 & 0 & 0.0087 \\ 0.0806 & 0.0806 & 0.2421 & 0 & 0 & 0 \\ 0 & 0 & 0 & 0.1199 & 0 & 0 \\ 0 & 0 & 0 & 0 & 0.1200 & 0 \\ -0.0087 & 0.0087 & 0 & 0 & 0 & 0.1174 \end{bmatrix}$	0.3703	$\begin{bmatrix} 0.5282 \\ 0.5282 \\ 0.6648 \\ 0 \\ 0 \\ 0 \end{bmatrix}$
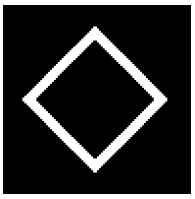	$\begin{bmatrix} 0.1832 & 0.0848 & 0.0804 & 0 & 0 & 0 \\ 0.0848 & 0.1832 & 0.0804 & 0 & 0 & 0 \\ 0.0804 & 0.0804 & 0.2412 & 0 & 0 & 0 \\ 0 & 0 & 0 & 0.1196 & 0 & 0 \\ 0 & 0 & 0 & 0 & 0.1196 & 0 \\ 0 & 0 & 0 & 0 & 0 & 0.1242 \end{bmatrix}$	0.3691	$\begin{bmatrix} 0.5285 \\ 0.5285 \\ 0.6644 \\ 0 \\ 0 \\ 0 \end{bmatrix}$

6.2 Spatial orientation of the sample material structure

The orientation of material properties can, and often will, vary from point to point. To characterize the coarse scale orientation field of the sample structure, we first need to evaluate the effective material properties of neighborhoods in the sample material at the fine scale. The process to calculate the effective material property is commonly referred as homogenization [48]. One popular strategy for homogenizing a material structure numerically is through Finite Element Method (FEM) where six independent periodic boundary conditions are imposed [151]. Though being effective, the FEM approach may become computationally too expensive to evaluate multiple fine-scale structures in the sample.

Facing this challenge, the effective material properties are often estimated through various homogenization theories, including the Gibson model for cellular materials [38], Voigt - Ruess bounds, Hashin - Strikman bounds [42], Green's function based method [107, 80], and power law [9] which is frequently used in SIMP-based topology optimization [8]. Many of these homogenization theories rely on the rotation invariant volume fraction as the sole characterization of the material structure, therefore, failing to capture the important anisotropic structural information of the material.

Instead, we propose to use the two-point correlation function of the material structure to efficiently estimate the effective property of the material. We start from the Lippmann-Schwinger equation:

$$\epsilon(x) = \epsilon^0 - \int_\Omega \Gamma(x, x')\delta C(x')\epsilon(x')dx', \tag{6.3}$$

where ϵ is the strain distribution of material structure under the constant strain ϵ^0 on the coarse scale, Γ is the second derivative of Green's function which is the impulse response of homogeneous reference material C^0, and δC is the difference between the elasticity tensors of the fine scale material structure and the reference homogenization material. The effective elasticity tensor may be derived by eliminating ϵ and ϵ^0 (see Appendix C for details):

$$\begin{aligned} C^{\text{eff}} &= C^0 + \langle \delta C(x) \rangle - \langle \int_\Omega \delta C(x)\Gamma(x, x')\delta C(x')\, dx' \rangle + \\ &\langle \int_\Omega \int_\Omega \delta C(x)\Gamma(x, x')\delta C(x')\, \Gamma(x, x'')\delta C(x'')\, dx''dx' \rangle - \cdots \end{aligned} \tag{6.4}$$

where $\langle \ldots \rangle$ is the expectation of a function. Clearly, the integrands bear the form of correlation functions. We estimate the effective elasticity tensor of the material by truncating after the first line of this equation, which is informationally equivalent to the two-point correlation function of the material.

To make this more explicit, let's assume heterogeneous material has two phases and $C^0 = C_1$ is the material property of phases 1 in a two-phase material, so that $\delta C(x) = I^{(1)}(x)(C_2 - C_1)$.

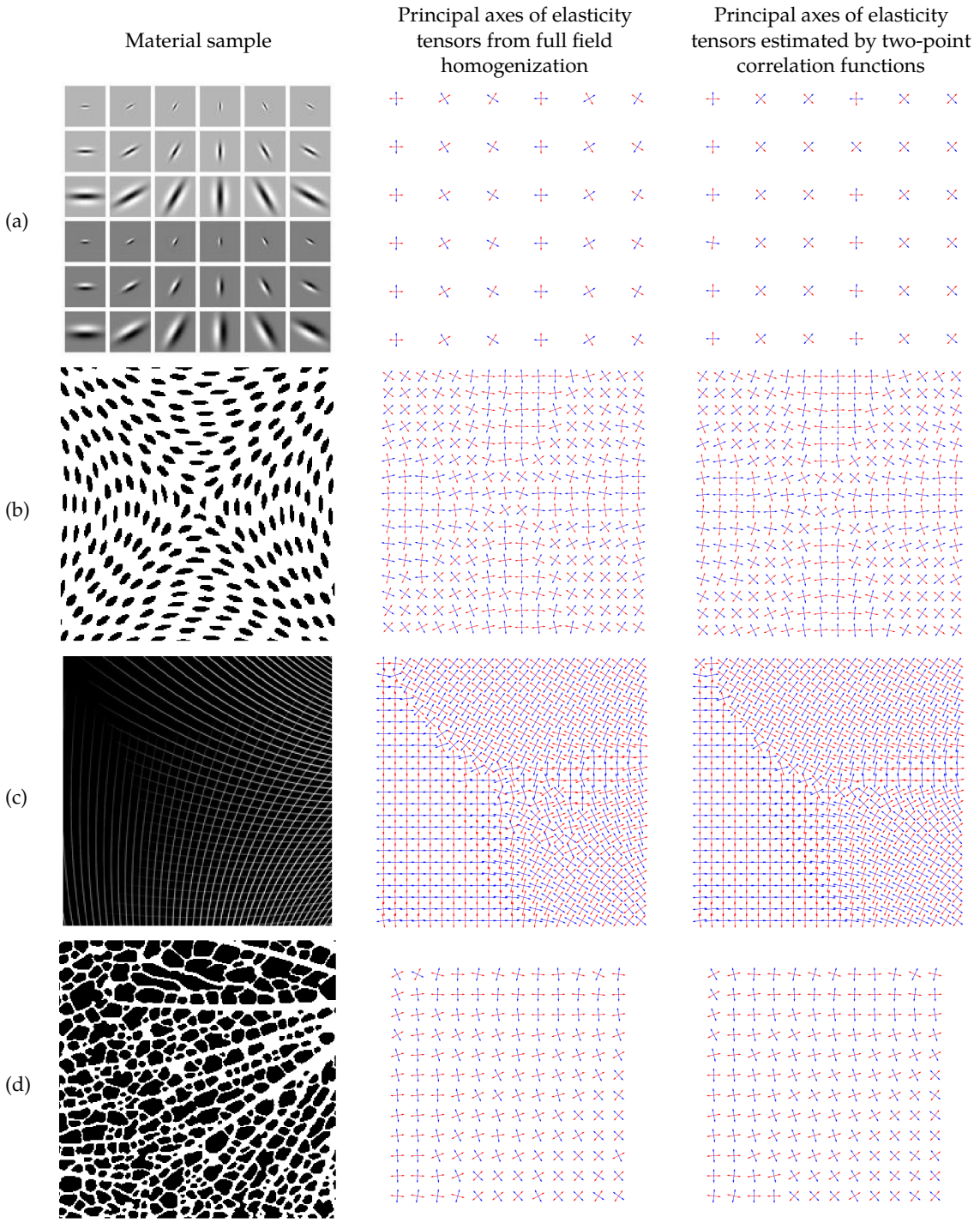

Figure 6.4: The principal directions of neighborhoods in the sample material structures. The first column shows the sample material structure. The second column shows the principal axes calculated from the fully homogenized elasticity tensors and the third column shows the principal axes calculated from elasticity tensors estimated by two-point correlation functions. Red arrows represent the major axes and blue arrows represent the minor axes. Young's modulus and Poisson's ratio, $E = 1$ MPa, $\nu = 0.3$ and $E = 0.02$ MPa, $\nu = 0.3$ are assigned to the white and black phases, respectively.

Table 6.2: Comparison of computation time between full field homogenization and the proposed two-point correlation function based method. Time is in seconds

Material	Full field	Correlation	Speed-up (times)
Figure 6.2 (a)	542.25	54.62	9.93×
Figure 6.2 (b)	6028	53.43	112.82×
Figure 6.4 (a)	51.20	2.07	24.73×
Figure 6.4 (b)	80.91	5.48	14.76×
Figure 6.4 (c)	31.68	2.69	11.78×
Figure 6.4 (d)	106.27	6.73	15.79×

Equation 6.4 becomes

$$\begin{aligned} C^{\text{eff}} =& C_1 + (C_2 - C_1)\langle S_1^{(1)}(x)\rangle - (C_2 - C_1)^2\langle \int_\Omega \Gamma(x, x') S_2^{(1)}(x, x')\, dx' \rangle + \\ & (C_2 - C_1)^3\langle \int_\Omega \int_\Omega \Gamma(x, x')\, \Gamma(x, x'') S_3^{(1)}(x, x', x'')\, dx'' dx' \rangle - \cdots \end{aligned} \tag{6.5}$$

which represents the elasticity tensor by a series expansion of all orders of correlation functions. The assumption may be relaxed for material to have more than two phases, but the equation will have significantly more terms.

Equation 6.4 and 6.5 allow the proposed method to take two different forms of inputs: (1) we may be given the detailed image of the material structure and our method only using information that is equivalent to the two-point correlation function, (2) or we may be given the correlation function of the material structure as the input to Equation 6.5. The two different types of the input will result in the same estimation of the effective elasticity tensor.

Figure 6.4 shows the spatial variation of principal axes within sample materials. The second and third column of Figure 6.4 compare the principal axes calculated from the effective elasticity tensors estimated from all terms (therefore, full field estimation) in Equation 6.4 and terms equivalent to two-point correlation functions, respectively. Each set of principal axes is calculated from the effective elasticity tensor of a neighborhood in the sample material. The effects of different neighborhood sizes are discussed in the conclusion section.

The computation time and the relative speed-ups are reported in Table 6.2. An average of

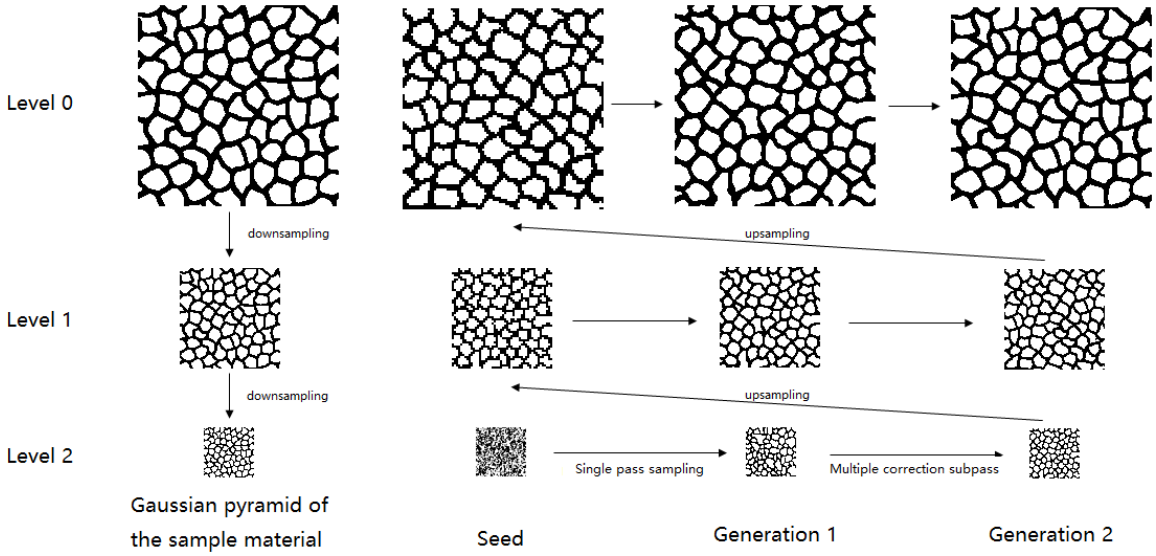

Figure 6.5: Parallel synthesis algorithm with Gaussian pyramid and correction subpasses.

16 times decrease in computation time is observed for 2D materials. The time to estimate each individual neighborhood by the correlation function based method depends only on the size of the neighborhood. As a result, the time to estimate effective elasticity tensors of the two material structures in Figure 6.2 are nearly identical since they are decretized with the same resolution.

6.3 Synthesis with rotated neighborhoods

Texture synthesis techniques are used to generate structures with non-uniform orientations from the sample material. Our implementation is inspired by results in [177, 73] with the difference that our sample material may have non-uniform orientations predicted by the method proposed in the previous section. To address this issue, we first rotate its neighborhoods to align their principal axes with the lattice grid of the image. During the synthesis, we may rotate every neighborhood in the sample material to align with the target orientation field; or equivalently, we may rotate the neighborhood window of the synthesized structure and leave the input material sample intact. The latter approach is adopted in our implementation given its computational efficiency.

Gaussian pyramid and correction subpasses are used to make the algorithm parallel (Figure 6.5). The Gaussian pyramid is a stack of series of images which are smoothed (blurred) by a Gaussian kernel and then down-sampled. After finishing the sampling at the lower resolution, the result will be up-sampled to be the template of sampling at the higher resolution. The sampling will be determined by sites sampled at the lower resolution. The benefit of using Gaussian Pyramid is twofold: firstly, it alleviates the computational burden without jeopardizing the actual size of the neighborhood by using a much smaller window size for comparison at different levels of resolution. Secondly, lower level Gaussian Pyramid can be seen as a good initial guess to guide the sampling and therefore eliminate the dependency on sampling order. In this process, closer sites gain more weight than sites further apart.

Since the material structures are synthesized with neighborhoods upsampled from a lower level of the image pyramid, these neighborhoods do not accurately represent the material at the current level of the MRF. Additional passes of sampling are required by using the neighborhoods from the current level of resolution. However, the concurrent resampling of all sites may lead to slow convergence or even cyclic changes because the neighbors of a site are also updating. To address this issue, we perform multiple resampling subpasses where only one site within a neighborhood is resampled in a single subpass.

Figure 6.6 shows the design of two-scale structures with Figure 6.4(d) as the sample input. The top row of the Figure 6.6 shows the relative density distribution of cantilever beams designed by SIMP - based topology optimization [78, 10] with fixtures at the left edge and downward loads at the lower right corner. The objective of the optimization is to minimize the structure's compliance (total strain energy, a measure of global deformation). SIMP employs power law as the material interpolation scheme to relate the relative density ρ and Young's modulus of the material:

$$E = E_{min} + \rho^p (E_0 - E_{min}), \qquad \rho \in [0, 1] \tag{6.6}$$

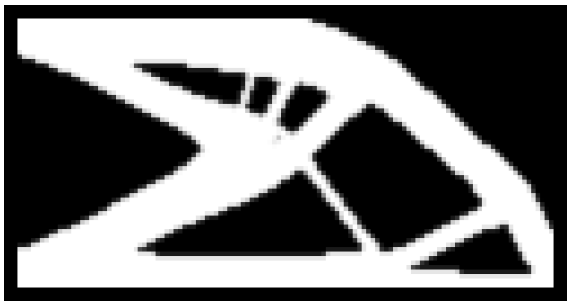

(a) Density distribution by SIMP with penalty factor equals 3.

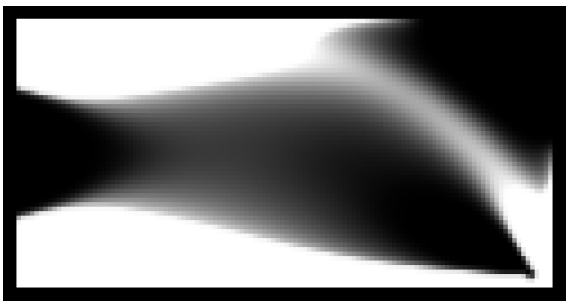

(b) Density distribution by SIMP with penalty factor equals 1.

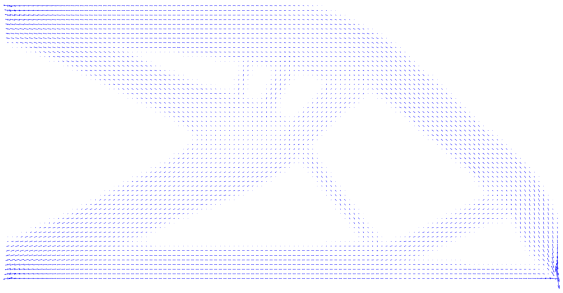

(c) Principal stress field of (a).

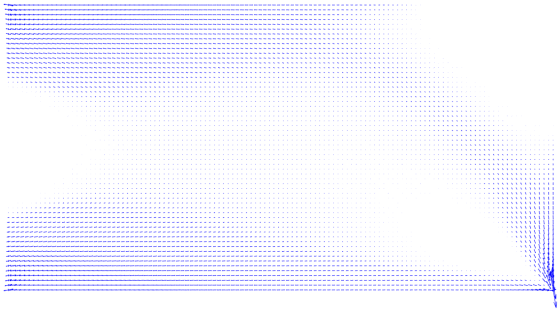

(d) Principal stress field of (b).

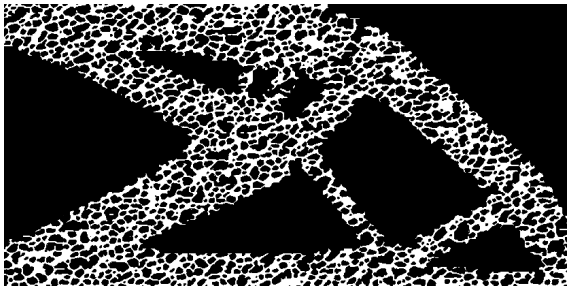

(e) Structure sampled without rotation of neighborhoods.

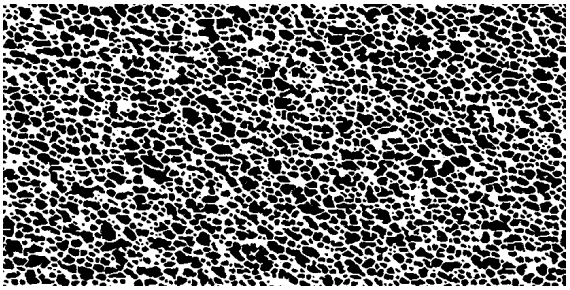

(f) Structure sampled without rotation of neighborhoods.

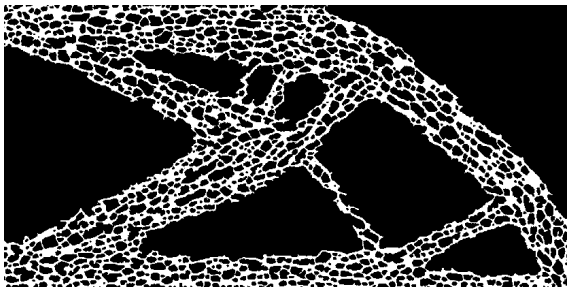

(g) Sampling result with neighborhood orientations following the direction of major principal strain of (c).

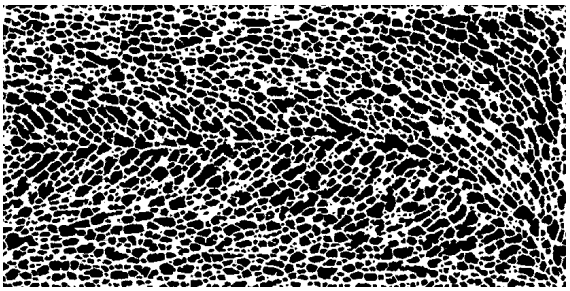

(h) Sampling result with neighborhood orientations following the direction of major principal strain of (d).

Figure 6.6: Two-scale structures synthesis with sample material of non-uniform orientations.

Table 6.3: Overall volume fractions and compliances of the structures in Figure 6.6 after refinement. Young's modulus and Poisson's ratio, $E = 1$ MPa, $\nu = 0.3$ and $E = 0.02$ MPa, $\nu = 0.3$ are assigned to the white and black phases, respectively.

Structure	Volume fraction	Compliance	Relative difference
e	0.240	5280.3557	60.51 %
g	0.231	2085.2674	
f	0.438	2378.2289	39.80 %
h	0.412	1431.6915	

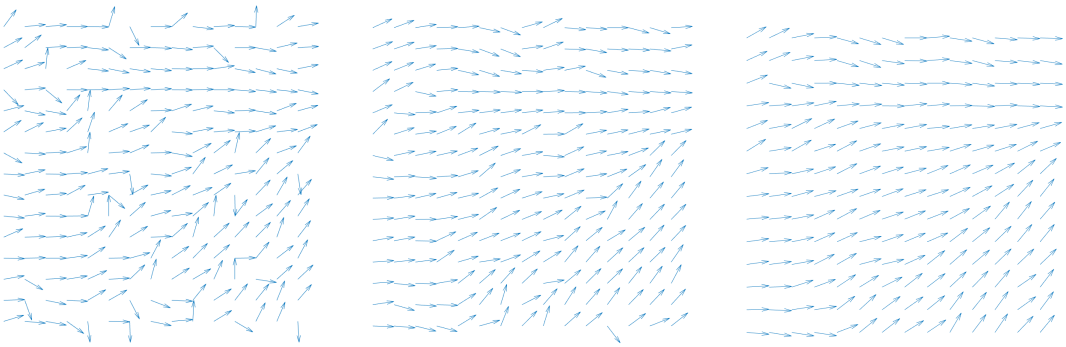

(a) 23×23 (b) 33×33 (c) 45×45

Figure 6.7: Principal axes of different sizes of neighborhoods. Only directions of major principal axes are shown for better clarity.

where E_0 and E_{min} are Young's moduli of the solid and void materials, respectively. E_{min} is non-zero to avoid singularity of the finite element stiffness matrix. Power p penalizes intermediate relative density and driving the structure towards a black-and-white design on the coarse scale.

The top row images on the left and right are optimization results with penalty factors p equal 3 and 1, respectively. Images on the second row represent the principal stress field inside the cantilever beams under the same boundary conditions as the optimization. The target orientation of the material structure is generated to follow the direction of major principal stress. Images on the third row show the sampling of design space without any rotation of the neighborhoods. These structures are generated to contrast with structures on the last row, which are designed material structures whose orientations follow the directions of major principal stress. The compliance of the

structures generated with and without the rotation of the neighborhoods is reported in Table 6.3. Stress concentrations near the boundary conditions may cloud the significance of the results. To remove such effects, we refine the generated structure by making the area near boundary conditions solid. Volume fractions and compliance of the refined structure, as well as their relative difference, are also reported in Table 6.3. The results clearly demonstrate the effectiveness of the proposed method by decreasing the total compliances of the synthesized structures by roughly 60% and 40%, respectively. It is also worth noting that the Figure 6.6(g) results in a smaller compliance than Figure 6.6(f) with only about the half of its volume fraction.

6.4 Discussion

We proposed a sample-based two-scale structures synthesis approach that explicitly controls the spatial orientations of the anisotropic effective properties on the coarse scale. An automatic way to characterize the material anisotropy is proposed by directly determining the principal axes of the fine scale structure from its effective elasticity tensor. The expensive numerical homogenization process for the effective elasticity tensor is replaced by a much more efficient two-point correlation function based method with minimum impacts on accuracy. The proposed method extends naturally other tensorial material properties, including electrical and thermal conductivity.

The current implementation infers the target orientation field from the principal stress field of a cantilever beam designed by SIMP-based topology optimization method. This is heuristics for two reasons. Firstly, the material is assumed isotropic during the SIMP iteration and therefore does not provide the optimal material property distribution for the beam that will subsequently be made from anisotropic two-scale structures. For a better integration of the two scales, the constraints imposed by the sample materials could be included in the optimization iterations to concurrently update both isotropic and anisotropic aspects of the coarse scale effective material properties. Secondly, the alignment of the principal axes of material and the principal direction of the stress only guarantee

to maximize the strain energy only when the material is orthotropic and the stress is not high shear (see Equation 6.1). The direction to maximize the efficiency of a general anisotropic material is still an open issue for a given arbitrary stress.

Another open issue in the present work is the size of the neighborhood for the evaluation of material properties. Figure 6.7 shows the effects of different neighborhood size on orientations of neighborhoods. It is evident that orientations from larger neighborhood render smoother and more continuous variation while ones from the smaller neighborhood are more sensitive to local variations of the material structures. In our implementation, we opt for the larger neighborhood size to capture the general trend within the sample material structure. Albeit requiring a longer time to evaluate, a larger neighborhood can potentially improve the computational efficiency by interpolating the distribution of principal axes from a few sampling neighborhoods due to the relative smoothness of the field.

Chapter 7

Conclusions and open issues

In this thesis, we proposed and developed sample-based material structure modeling via a Markov random field. By interpreting a material structure as a collection of neighborhoods, the proposed method facilitates the design and manufacturing of material structures towards desired structural and mechanical properties while preserving the microscopic geometry of the sample material structure. We investigated the reconstruction of stationary material, design and reconstruction of functionally graded material, and design with neighborhood orientations to not only demonstrate the effectiveness of the proposed method but also further our own understanding. Efficient homogenization methods based on the Green's function and FFT are also explored to facilitate the design of material structure towards target mechanical properties. The contribution of the thesis is summarized as follows:

In Chapter 3, we proposed the reconstruction of stationary material structures by sampling the Markov random field of the sample material with the Wei-Levoy algorithm. We demonstrate that the proposed method is not only compatible with the classic optimization - based reconstruction method by preserving lower order correlation functions, but also exceeds it by preserving higher - order correlation functions, Minkowski functionals, and mechanical properties of the sample material. Assuming the existence of a germ-grain model of the material sample, we propose and verify a

systematic approach to determine the optimal neighborhood size, a key parameter in the MRF model, based on the two-point correlation function. With Gaussian pyramid, our implementation is fully parallelable and suitable for the integration into the existing CAD system as a query-based method.

In Chapter 4, the model proposed in Chapter 3 is generalized to facilitate the design and reconstruction of non-stationary material structures. As MRF is inherently non-parametric, the spatial variation of material structures on the macroscopic scale is formulated and controlled directly by material properties. A hybrid sampling algorithm is proposed to efficiently sample the MRF model with a well-defined design space. To circumvent the expensive solution of boundary value problem, the spatially varying material properties are represented and controlled using the notion of material descriptors which include common geometric, statistical, and topological measures such as correlation functions and Minkowski functionals. The issue of compatibility between the reference material structure and the target properties field is identified.

In Chapter 5, we explored the homogenization of material structure to better facilitate the design of functionally graded materials. We showed an explicit relationship between the effective elasticity tensor and the correlation functions of the material structure. A Green's function and FFT - based homogenization method is investigated for the efficient evaluation of the mechanical properties of the neighborhoods. We show that the formulated integral equation can be converted into a system of linear equations which is symmetric and positive definite with the appropriate reference material property and therefore can be solved efficiently using the conjugate gradient method. To compare the proposed homogenization method with physical test results, an effective geometry - material model is proposed to evaluate the mechanical performance of additively manufactured structures.

In Chapter 6, we further expanded the design space of material structures by controlling the orientation of neighborhoods during the sampling process. Since simply selecting neighborhoods with desired orientations eliminates too many suitable neighborhoods, we expand the design space to include the rotation of neighborhoods. Such expansion of the design space may be implemented

when the properties that need to be preserved can be safely regarded as rotational invariant. With the assumption of orthotropic symmetry, we proposed an automatic way to determine the principal axes of a neighborhood directly from its elasticity tensor. Experiment results show the effectiveness the proposed methods.

One apparent limitation of the proposed method is that it cannot guarantee that the specified distribution of material properties is achieved, because this explicitly requires compatibility between the reference material structure and the target properties field, as identified in Chapter 4. We note, however, that the notion of (N, D)-compatibility allows fine tuning the tradeoffs between the neighborhood and the descriptor incompatibilities. Methods for evaluating the compatibilities *a priori* appear to be a useful direction for future explorations.

Remedies for large incompatibilities include modifying the target property fields, enriching or modifying the reference material structure, or both. For example, the reference material structure may be modified using morphological operations to increase compatibility, but such modifications could also alter the properties of the reference material. New reference material structures could also be designed by other methods reviewed in Chapter 2, when the target properties are beyond the reach of the direct modification of the reference material structure.

The sensitivity of different material descriptors under morphological change is also worth exploring. With the understanding of structure - physical property relationship, the sensitivity can provide insightful predictions on the physical properties of material structure under perturbations. This may facilitate the development of novel random heterogeneous material.

Currently, the generation of material structure and the design of material property distribution are treated as separated processes. The knowledge of target material property distribution is always assumed. However, the change of material structure does affect the optimal solution of the macroscopic property distribution. A better integration of the two scales is desired in the future.

The link to the manufacturing parameters and constraint of the manufacturing process also plays an important role in the design of material structure. Additive manufacturing is especially suitable

to fabricate the complex structure designed by the proposed method. Discussions in Chapter 5 related manufacturing process to the mechanical performance of the printed structure. However, other aspects of manufacturability, such as the connectivity of the structure, the requirement of the support, should also be studied in the future.

Appendix A

Green's function for elasticity

The elastic Green's function $G_{ij}(x, x')$ is defined as the displacement in the i - direction at x due to a point force in the j - direction at x'. It is the solution $u_i(x)$ of Equation (5.1) when the body force b_j is a delta function, i.e. $b_k(x) = \delta(x - x')\delta_{jk}$ The Equation (5.1) and the symmetry of strain tensor directly gives

$$[C_{ijkl}u_{k,l}]_{,j} + b_i = 0, \tag{A.1}$$

Consider a constant point force F acting at x' in Ω, the displacement field caused by F is

$$u_k(x) = G_{kp}(x, x')F_p. \tag{A.2}$$

The displacement gradient and stress field are

$$\begin{aligned} u_{k,l}(x) &= G_{kp,l}(x, x')F_p, \\ \sigma_{ij}(x) &= C_{ijkl}(x)G_{kp,l}(x, x')F_p. \end{aligned} \tag{A.3}$$

If force F is acting on point $x' \in \Omega$, then F must be balanced by the tractions on the boundary $\partial\Omega$:

$$\begin{aligned} F_i + \int_{\partial\Omega} \sigma_{ij}(x) n_j(x)\, dS = 0, \\ F_i + \int_{\partial\Omega} C_{ijkl}(x) G_{kp,l}(x, x') n_j(x) F_p\, dx = 0. \end{aligned} \tag{A.4}$$

By divergence theorem

$$F_i + \int_{\Omega} [C_{ijkl}(x) G_{kp,l}(x, x')]_{,j} F_p\, dx = 0. \tag{A.5}$$

F_i can be moved into the volume integral by the Dirac delta function

$$\int_{\Omega} \{[C_{ijkl}(x) G_{kp,l}(x, x')]_{,j} F_p + F_i \delta(x - x')\}\, dx = 0. \tag{A.6}$$

Factoring F_p out using Kronecker delta function

$$\int_{\Omega} \{[C_{ijkl}(x) G_{kp,lj}(x, x')]_{,j} + \delta_{ip}\delta(x - x')\} F_p\, dx = 0. \tag{A.7}$$

Since this holds for any arbitrary Ω and any arbitrary constant point force F, it must holds for every point:

$$[C_{ijkl}(x) G_{kp,l}(x, x')]_{,j} + \delta_{ip}\delta(x - x') = 0. \tag{A.8}$$

Since Equation (A.1) is linear in b, for arbitrary b, by superposition:

$$u_k(x) = \int_{\Omega} G_{kp}(x, x') b_p(x')\, dx'. \tag{A.9}$$

For an infinite and uniform material, C_{ijkl} is constant and $G(x, x') = G(x - x') = G(x)$ by setting $x' = 0$. Then Equation (A.8) becomes:

$$C_{ijkl} G_{kp,jl}(x) + \delta_{ip}\delta(x) = 0. \tag{A.10}$$

Let the forward and inverse Fourier transform of $G(x)$ be

$$\begin{aligned} \hat{G}_{ij}(\xi) &= \int_{-\infty}^{\infty} G_{ij}(x) e^{-i\xi x} dx, \\ G_{ij}(x) &= \int_{-\infty}^{\infty} \hat{G}_{ij}(\xi) e^{i\xi x} d\xi. \end{aligned} \tag{A.11}$$

Note that index i should not be confused with complex number $i = \sqrt{-1}$. With $\delta(x) = \int_{-\infty}^{\infty} e^{i\xi x} d\xi$, substitute Equation (A.11) into Equation (A.10):

$$\int_{-\infty}^{\infty} \Big[i^2 \xi_j \xi_l C_{ijkl} \hat{G}_{kp}(\xi) + \delta_{ip} \Big] e^{i\xi x} d\xi = 0. \tag{A.12}$$

For this to be true at all x, we must have:

$$\begin{aligned} -\xi_j \xi_l C_{ijkl} \hat{G}_{kp}(\xi) + \delta_{ip} &= 0, \\ \hat{G}_{ki}(\xi) &= (C_{ijkl} \xi_j \xi_l)^{-1}. \end{aligned} \tag{A.13}$$

The Green's operator is the second order derivative of the Green's function:

$$\Gamma_{mnpq} = -\frac{1}{4} \Big[\frac{\partial^2 G_{mp}}{\partial x_n \partial x_q} + \frac{\partial^2 G_{np}}{\partial x_m \partial x_q} + \frac{\partial^2 G_{mq}}{\partial x_n \partial x_p} + \frac{\partial^2 G_{nq}}{\partial x_m \partial x_p} \Big]. \tag{A.14}$$

In frequency domain:

$$\begin{aligned} \hat{\Gamma}_{mnpq} = \frac{1}{4} \Big[&(C_{pjml} \xi_j \xi_l)^{-1} \xi_n \xi_q + (C_{pjnl} \xi_j \xi_l)^{-1} \xi_m \xi_q + \\ &(C_{qjml} \xi_j \xi_l)^{-1} \xi_n \xi_p + (C_{qjnl} \xi_j \xi_l)^{-1} \xi_m \xi_p \Big]. \end{aligned} \tag{A.15}$$

For isotropic material with Lame coefficients λ and μ:

$$\begin{aligned} C_{ijkl} =& \lambda\delta_{ij}\delta_{kl} + \mu(\delta_{ik}\delta_{jl} + \delta_{il}\delta_{jk}), \\ C_{ikjl}\xi_k\xi_l =& (\lambda+\mu)\xi_i\xi_j + \mu|\xi|^2\delta_{ij}, \\ \hat{\Gamma}_{ijkl} =& \frac{1}{4\mu|\xi|^2}(\delta_{ik}\xi_l\xi_j + \delta_{il}\xi_k\xi_j + \delta_{jk}\xi_l\xi_i + \delta_{lj}\xi_i\xi_k) \\ & - \frac{\lambda+\mu}{\mu(\lambda+2\mu)}\frac{\xi_i\xi_j\xi_k\xi_l}{|\xi|^4}. \end{aligned} \tag{A.16}$$

Appendix B

Three notations for the constitutive equation

B.1 Tensor notation

The constitutive relation for linear elasticity is described by the fourth-rank tensor C_{ijkl}, defined according to

$$\sigma_{ij} = C_{ijkl}\epsilon_{kl} \tag{B.1}$$

Independent of material symmetry, there are three important symmetry restrictions on the elasticity tensor C_{ijkl}:

$$C_{ijkl} = C_{jikl}, \qquad C_{ijkl} = C_{ijlk}, \qquad C_{ijkl} = C_{klij} \tag{B.2}$$

The first two are minor symmetries and follow from the symmetries of stress and strain tensor, the last one is major symmetry and is the result of the thermodynamic requirement that no work be produced by the elastic material in a closed loading cycle [99]. The following equation is used to

transform between coordinate systems:

$$C'_{mnop} = R_{mi}R_{nj}R_{ok}R_{pl}C_{ijkl}, \tag{B.3}$$

where R factors are direction cosines.

The tensor notation is good for mathematical deduction, but it is less straightforward for computation on some simple tasks, such as eigenvalue and inversion. For this reason, matrix notations is often adopted for these tasks.

B.2 Voigt notation

Given the symmetry of the fourth - rank tensor, it is easy to see that Equation B.1 can be written in matrix notation with the mapping $\sigma^V = \{\sigma_{11}, \sigma_{22}, \sigma_{33}, \sigma_{23}, \sigma_{13}, \sigma_{12}\}$ and $\epsilon^V = \{\epsilon_{11}, \epsilon_{22}, \epsilon_{33}, 2\epsilon_{23}, 2\epsilon_{13}, 2\epsilon_{12}\} = \{\epsilon_{11}, \epsilon_{22}, \epsilon_{33}, \gamma_{23}, \gamma_{13}, \gamma_{12}\}$:

$$\begin{bmatrix} \sigma_{11} \\ \sigma_{22} \\ \sigma_{33} \\ \sigma_{23} \\ \sigma_{13} \\ \sigma_{12} \end{bmatrix} = \begin{bmatrix} C_{1111} & C_{1122} & C_{1133} & C_{1123} & C_{1113} & C_{1112} \\ C_{2211} & C_{2222} & C_{2233} & C_{2223} & C_{2213} & C_{2212} \\ C_{3311} & C_{3322} & C_{3333} & C_{3323} & C_{3313} & C_{3312} \\ C_{2311} & C_{2322} & C_{2333} & C_{2323} & C_{2313} & C_{2312} \\ C_{1311} & C_{1322} & C_{1333} & C_{1323} & C_{1313} & C_{1312} \\ C_{1211} & C_{1222} & C_{1233} & C_{1223} & C_{1213} & C_{1212} \end{bmatrix} \begin{bmatrix} \epsilon_{11} \\ \epsilon_{22} \\ \epsilon_{33} \\ \gamma_{23} \\ \gamma_{13} \\ \gamma_{12} \end{bmatrix} \tag{B.4}$$

where $\gamma_{23} = 2\epsilon_{23}$, $\gamma_{13} = 2\epsilon_{13}$ and $\gamma_{12} = 2\epsilon_{12}$ are engineering shear strains. The factor of 2 is used to preserve the elastic energy.

There are several difficulties associated with Voigt notation. Firstly, different baseis are used for $\boldsymbol{\sigma}$ and $\boldsymbol{\epsilon}$ and therefore different transformation matrix is used for strain and stress during coordinate system transformation. Secondly, these transformation matrices are not orthonormal and thus characteristics such as norm and eigenvalues of $\boldsymbol{\sigma}$, $\boldsymbol{\epsilon}$ and $\mathbf{C}$ are no longer rotation invariant and not

preserved.

B.3 Mandel notation

Mandel notation, also known as the Kelvin notation, is different from the Voigt notation in the mapping of strain and stress. The same mapping is used for both stress and strain:

$$\sigma^{M} = \{\sigma_{11}, \sigma_{22}, \sigma_{33}, \sqrt{2}\sigma_{23}, \sqrt{2}\sigma_{13}, \sqrt{2}\sigma_{12}\} \tag{B.5}$$

and

$$\epsilon^{M} = \{\epsilon_{11}, \epsilon_{22}, \epsilon_{33}, \sqrt{2}\epsilon_{23}, \sqrt{2}\epsilon_{13}, \sqrt{2}\epsilon_{12}\} \tag{B.6}$$

The constitutive equation under Mandel notation is defined as follows:

$$\begin{bmatrix} \sigma_{11} \\ \sigma_{22} \\ \sigma_{33} \\ \sqrt{2}\sigma_{23} \\ \sqrt{2}\sigma_{13} \\ \sqrt{2}\sigma_{12} \end{bmatrix} = \begin{bmatrix} C_{1111} & C_{1122} & C_{1133} & \sqrt{2}C_{1123} & \sqrt{2}C_{1113} & \sqrt{2}C_{1112} \\ C_{2211} & C_{2222} & C_{2233} & \sqrt{2}C_{2223} & \sqrt{2}C_{2213} & \sqrt{2}C_{2212} \\ C_{3311} & C_{3322} & C_{3333} & \sqrt{2}C_{3323} & \sqrt{2}C_{3313} & \sqrt{2}C_{3312} \\ \sqrt{2}C_{2311} & \sqrt{2}C_{2322} & \sqrt{2}C_{2333} & 2C_{2323} & 2C_{2313} & 2C_{2312} \\ \sqrt{2}C_{1311} & \sqrt{2}C_{1322} & \sqrt{2}C_{1333} & 2C_{1323} & 2C_{1313} & 2C_{1312} \\ \sqrt{2}C_{1211} & \sqrt{2}C_{1222} & \sqrt{2}C_{1233} & 2C_{1223} & 2C_{1213} & 2C_{1212} \end{bmatrix} \begin{bmatrix} \epsilon_{11} \\ \epsilon_{22} \\ \epsilon_{33} \\ \sqrt{2}\epsilon_{23} \\ \sqrt{2}\epsilon_{13} \\ \sqrt{2}\epsilon_{12} \end{bmatrix} \tag{B.7}$$

Same as the Voigt notation, the Mandel notation preserves the elastic energy. In addition, the Mandel notation has many advantages over the Voigt notation. Most importantly, the strain and stress vector are under the same basis and therefore using the same transformation matrix during coordinate system transformation. Such transformation matrix is orthonormal and therefore characteristics such as norm and eigenvalues of $\boldsymbol{\sigma}$, $\boldsymbol{\epsilon}$ and $\mathbf{C}$ are rotation invariant and preserved. The tensorial equivalents between 4-*th* rank tensor notation and the Mandel notation is shown in [99]. We use Mandel notation based on its invariant property.

The transformation matrix for Mendal notation can be constructed from the transformation of strain in tensor notation:

$$\epsilon' = R\epsilon R^T = \begin{bmatrix} R_{11} & R_{12} & R_{13} \\ R_{21} & R_{22} & R_{23} \\ R_{31} & R_{32} & R_{33} \end{bmatrix} \begin{bmatrix} \epsilon_{11} & \epsilon_{12} & \epsilon_{13} \\ \epsilon_{21} & \epsilon_{22} & \epsilon_{23} \\ \epsilon_{31} & \epsilon_{32} & \epsilon_{33} \end{bmatrix} \begin{bmatrix} R_{11} & R_{21} & R_{31} \\ R_{12} & R_{22} & R_{32} \\ R_{13} & R_{23} & R_{33} \end{bmatrix} \tag{B.8}$$

In Mandel notation, $\epsilon^{M'} = R^M \epsilon^M$, where

$$R^M = \begin{bmatrix} R_{11}^2 & R_{12}^2 & R_{13}^2 & \sqrt{2}R_{12}R_{13} & \sqrt{2}R_{11}R_{13} & \sqrt{2}R_{11}R_{12} \\ R_{21}^2 & R_{22}^2 & R_{23}^2 & \sqrt{2}R_{22}R_{23} & \sqrt{2}R_{21}R_{23} & \sqrt{2}R_{22}R_{21} \\ R_{31}^2 & R_{32}^2 & R_{33}^2 & \sqrt{2}R_{33}R_{32} & \sqrt{2}R_{33}R_{31} & \sqrt{2}R_{31}R_{32} \\ \sqrt{2}R_{21}R_{31} & \sqrt{2}R_{22}R_{32} & \sqrt{2}R_{23}R_{33} & R_{22}R_{32} + R_{23}R_{32} & R_{21}R_{33} + R_{31}R_{23} & R_{21}R_{32} + R_{31}R_{22} \\ \sqrt{2}R_{11}R_{31} & \sqrt{2}R_{12}R_{32} & \sqrt{2}R_{13}R_{23} & R_{12}R_{23} + R_{32}R_{13} & R_{11}R_{33} + R_{13}R_{31} & R_{11}R_{32} + R_{31}R_{12} \\ \sqrt{2}R_{11}R_{21} & \sqrt{2}R_{12}R_{22} & \sqrt{2}R_{13}R_{23} & R_{12}R_{23} + R_{22}R_{13} & R_{11}R_{23} + R_{21}R_{13} & R_{11}R_{22} + R_{21}R_{12} \end{bmatrix} \tag{B.9}$$

For example,

$$R = \begin{bmatrix} 1 & 0 & 0 \\ 0 & c & -s \\ 0 & s & c \end{bmatrix} \tag{B.10}$$

is the rotation around the x axis, where $c = \cos(\theta)$ and $s = \sin(\theta)$. The associated rotation in the Mendal notation is:

$$R^M = \begin{bmatrix} 1 & 0 & 0 & 0 & 0 & 0 \\ 0 & c^2 & s^2 & -\sqrt{2}sc & 0 & 0 \\ 0 & s^2 & c^2 & \sqrt{2}sc & 0 & 0 \\ 0 & \sqrt{2}sc & -\sqrt{2}sc & c^2 - s^2 & 0 & 0 \\ 0 & 0 & 0 & 0 & c & s \\ 0 & 0 & 0 & 0 & -s & c \end{bmatrix} \tag{B.11}$$

Rotations around other axes can be easily derived.

Appendix C

Effective elasticity tensor by correlation functions

In this section, we derive relationship between correlation functions and effective elasticity tensor from Neumann series expansion of the Lippmann - Schwinger equation. We first eliminate strain ϵ from Equation 6.3. Rearrange ϵ and ϵ^0 and multiple C on the both sides of the Equation 6.3:

$$\epsilon = [I + \Gamma\delta C]^{-1}\epsilon^0 \tag{C.1}$$

$$\sigma = (C^0 + \delta C)[I + \Gamma\delta C]^{-1}\epsilon^0 \tag{C.2}$$

Take the average on both side of Equation (C.1) and Equation (C.2)

$$\overline{\epsilon} = \langle [I + \Gamma\delta C]^{-1} \rangle \epsilon^0 \tag{C.3}$$

$$\overline{\sigma} = \langle (C^0 + \delta C)[I + \Gamma\delta C]^{-1} \rangle \epsilon^0 \tag{C.4}$$

Combine Equation (C.3) and Equation (C.4) to eliminate ϵ^0

$$\overline{\sigma} = \langle (C^0 + \delta C)[I + \Gamma \delta C]^{-1} \rangle \langle [I + \Gamma \delta C]^{-1} \rangle^{-1} \overline{\epsilon}$$

By the definition of effective elastic tensor

$$\begin{aligned} C^{\text{eff}} &= \langle (C^0 + \delta C)[I + \Gamma \delta C]^{-1} \rangle \langle [I + \Gamma \delta C]^{-1} \rangle^{-1} \\ &= C^0 + \langle \delta C[I + \Gamma \delta C]^{-1} \rangle \langle [I + \Gamma \delta C]^{-1} \rangle^{-1} \end{aligned} \tag{C.5}$$

If two bodies of the same domain are subject to the same displacement boundary condition, they share the same mean strain, i.e. $\epsilon^0 = \overline{\epsilon}$. Equation (C.1) becomes

$$\overline{\epsilon} = \langle [I + \Gamma \delta C]^{-1} \rangle \overline{\epsilon} \tag{C.6}$$

Multiply Equation (C.6) on both side of Equation (C.5)

$$\begin{aligned} \overline{\sigma} = C^{\text{eff}} \overline{\epsilon} &= C^0 \overline{\epsilon} + \langle \delta C[I + \Gamma \delta C]^{-1} \rangle \overline{\epsilon} \\ C^{\text{eff}} &= C^0 + \langle \delta C[I + \Gamma \delta C]^{-1} \rangle \end{aligned} \tag{C.7}$$

Use Neumann series (generalized geometric series) to expand the right side of Equation (C.7)

$$\begin{aligned} C^{\text{eff}} &= C^0 + \langle \delta C \rangle - \langle \delta C \Gamma \delta C \rangle + \langle \delta C \Gamma \delta C \Gamma \delta C \rangle - \cdots \\ &= C^0 + \langle \delta C(x) \rangle - \langle \delta C(x) \int_\Omega \Gamma(x, x') \delta C(x') \, dx' \rangle \\ &\quad + \langle \delta C(x) \int_\Omega \Gamma(x, x') \delta C(x') \, dx' \int_\Omega \Gamma(x, x'') \delta C(x'') \, dx'' \rangle \cdots \end{aligned}$$

where C^0 is the constant reference material property and $\delta C(x) = C(x) - C^0$. Combine the integrals and move $\delta C(x)$ inside:

$$C^{\text{eff}} = C^0 + \langle \delta C(x) \rangle - \langle \int_\Omega \delta C(x) \Gamma(x, x') \delta C(x') \, dx' \rangle +$$
$$\langle \int_\Omega \int_\Omega \delta C(x) \Gamma(x, x') \delta C(x') \, \Gamma(x, x'') \delta C(x'') \, dx'' dx' \rangle - \cdots$$

Bibliography

[1] C. H. Arns, M. a. Knackstedt, W. V. Pinczewski, and K. R. Mecke. Euler-Poincaré characteristics of classes of disordered media. *Physical review. E, Statistical, nonlinear, and soft matter physics*, 63(3 Pt 1):031112, feb 2001.

[2] M. Ashikhmin. Synthesizing natural textures. *Proceedings of the 2001 symposium on Interactive 3D graphics*, pages 217–226, 2001.

[3] C. Barnes, E. Shechtman, A. Finkelstein, and D. B. Goldman. PatchMatch: A Randomized Correspondence Algorithm for Structural Image Editing. *ACM Transactions on Graphics*, 28(3):1, 2009.

[4] C. Barnes, F.-l. Zhang, L. Lou, X. Wu, and S.-m. Hu. PatchTable: Efficient Patch Queries for Large Datasets and Applications. *ACM Transactions on Graphics*, 34(4):97:1–97:10, 2015.

[5] C. Beisbart, M. S. Barbosa, H. Wagner, and L. D. F. Costa. Extended morphometric analysis of neuronal cells with Minkowski valuations. *European Physical Journal B*, 52(4):531–546, 2006.

[6] C. Beisbart, R. Dahlke, K. R. Mecke, and H. Wagner. Vector- and tensor-valued descriptors for spatial patterns. In *Morphology of condensed matter*, page 24. Springer, 2002.

[7] C. Bellehumeur, L. Li, Q. Sun, and P. Gu. Modeling of Bond Formation Between Polymer Filaments in the Fused Deposition Modeling Process. *Journal of Manufacturing Processes*, 6(2):170–178, 2004.

[8] M. P. Bendsøe. Optimal shape design as a material distribution problem. *Structural Optimization*, 1(4):193–202, 1989.

[9] M. P. Bendsøe and O. Sigmund. Material interpolation schemes in topology optimization. *Archive of Applied Mechanics*, 69(9-10):635–654, 1999.

[10] M. P. Bendsoe and O. Sigmund. *Topology optimization: theory, methods, and applications*. Springer Science & Business Media, 2013.

[11] M. Beran. Statistical Continuum Theories. *Journal of Rheology*, 9(1):339, 1965.

[12] V. Birman and L. W. Byrd. Modeling and Analysis of Functionally Graded Materials and Structures. *Applied Mechanics Reviews*, 60(5):195, 2007.

[13] A. Biswas, V. Shapiro, and I. Tsukanov. Heterogeneous material modeling with distance fields. *Computer Aided Geometric Design*, 21(3):215–242, mar 2004.

[14] S. Bose, M. Roy, and A. Bandyopadhyay. Recent advances in bone tissue engineering scaffolds. *Trends in Biotechnology*, 30(10):546–554, 2012.

[15] R. Bostanabad, A. T. Bui, W. Xie, D. W. Apley, and W. Chen. Stochastic microstructure characterization and reconstruction via supervised learning. *Acta Materialia*, 103:89–102, 2016.

[16] R. Bostanabad, W. Chen, and D. W. Apley. Characterization and reconstruction of 3D stochastic microstructures via supervised learning. *Journal of Microscopy*, 264(3):282–297, 2016.

[17] S. Brisard and L. Dormieux. FFT-based methods for the mechanics of composites: A general variational framework. *Computational Materials Science*, 49(3):663–671, 2010.

[18] S. Brisard and L. Dormieux. Combining Galerkin approximation techniques with the principle of Hashin and Shtrikman to derive a new FFT-based numerical method for the homogenization of composites. *Computer Methods in Applied Mechanics and Engineering*, 217-220:197–212, 2012.

[19] B. Brunet-Imbault, G. Lemineur, C. Chappard, R. Harba, and C.-L. Benhamou. A new anisotropy index on trabecular bone radiographic images using the fast Fourier transform. *BMC medical imaging*, 5:4, 2005.

[20] R. Cang and M. Y. Ren. Deep Network-Based Feature Extraction and Reconstruction of Complex Material Microstructures. In *Volume 2B: 42nd Design Automation Conference*, number 50114, page V02BT03A008. ASME, aug 2016.

[21] Y. Chen. 3D texture mapping for rapid manufacturing. *Computer-Aided Design and Applications*, 4(1-6):761–771, 2007.

[22] G. Cheng and P. Pedersen. On sufficiency conditions for optimal design based on extremum principles of mechanics. *Journal of the Mechanics and Physics of Solids*, 45(1):135–150, 1997.

[23] J. R. Cho and D. Y. Ha. Optimal tailoring of 2D volume-fraction distributions for heat-resisting functionally graded materials using FDM. *Computer Methods in Applied Mechanics and Engineering*, 191(29-30):3195–3211, 2002.

[24] D. R. Clarke. Interpenetrating Phase Composites. *Journal of the American Ceramic Society*, 75(4):739–758, 1992.

[25] J. Corney and C. Torres-Sanchez. Towards functionally graded cellular microstructures. *Journal of Mechanical Design*, 131(September 2009):1–7, 2008.

[26] P. B. Corson. Correlation Functions for Predicting Properties of Heterogeneous Materials - 2. Empirical Construction of Spatial Correlation Functions for Two-Phase Solids. *Journal of Applied Physics*, 45(7):3165–3170, 1974.

[27] S. C. Cowin. The relationship between the elasticity tensor and the fabric tensor. *Mechanics of Materials*, 4(2):137–147, 1985.

[28] D. Cule and S. Torquato. Generating random media from limited microstructural information via stochastic optimization. *Journal of Applied Physics*, 86(6):3428, 1999.

[29] S. Darabi, E. Shechtman, C. Barnes, D. B. Goldman, and P. Sen. Image melding: combining inconsistent images using patch-based synthesis. *ACM Transactions on Graphics*, 31(4):1–10, 2012.

[30] T. Davidson. An Introduction to Failure Analysis for Metallurgical Engineers. *TMS Outstanding Student Paper Contest Winner– 1999 Undergraduate Division*, 1999.

[31] J. S. De Bonet. Multiresolution sampling procedure for analysis and synthesis of texture images. In *Proceedings of the 24th annual conference on Computer graphics and interactive techniques SIGGRAPH 97*, volume 31, pages 361–368. ACM Press/Addison-Wesley Publishing Co., 1997.

[32] E. Doubrovski, E. Tsai, D. Dikovsky, J. Geraedts, H. Herr, and N. Oxman. Voxel-based fabrication through material property mapping: A design method for bitmap printing. *Computer-Aided Design*, 2014.

[33] W. J. Drugan and J. R. Willis. A micromechanics-based nonlocal constitutive equation and estimates of representative volume element size for elastic composites. *Journal of the Mechanics and Physics of Solids*, 44(4):497–524, 1996.

[34] A. Efros and W. Freeman. Image Quilting for Texture Synthesis and Transfer. In *Proceedings of the 28th annual conference on Computer graphics and interactive techniques*, volume 1, pages 1–6. Los Angeles, California, USA, 2001.

[35] O. Fryazinov, M. Sanchez, and A. Pasko. Shape conforming volumetric interpolation with interior distances. *Computers & Graphics*, 46:149–155, 2015.

[36] O. Fryazinov, T. Vilbrandt, and A. Pasko. Multi-scale space-variant FRep cellular structures. *Computer-Aided Design*, 45(1):26–34, jan 2013.

[37] L. J. Gibson and M. F. Ashby. The Mechanics of Three-Dimensional Cellular Materials. *Proceedings of the Royal Society A: Mathematical, Physical and Engineering Sciences*, 382(1782):43–59, 1982.

[38] L. J. Gibson and M. F. Ashby. *Cellular solids: Structure and properties*, volume 123. Cambridge university press, Cambridge, England, 1990.

[39] L. Graham-Brady and X. F. Xu. Stochastic Morphological Modeling of Random Multiphase Materials. *Journal of Applied Mechanics*, 75(6):061001, 2008.

[40] E. Y. Guo, N. Chawla, T. Jing, S. Torquato, and Y. Jiao. Accurate modeling and reconstruction of three-dimensional percolating filamentary microstructures from two-dimensional micrographs via dilation-erosion method. *Materials Characterization*, 89:33–42, mar 2014.

[41] T. P. Harrigan and R. W. Mann. Characterization of microstructural anisotropy in orthotropic materials using a second rank tensor. *Journal of Materials Science*, 19(3):761–767, 1984.

[42] Z. Hashin and S. Shtrikman. A variational approach to the theory of the elastic behaviour of multiphase materials. *Journal of the Mechanics and Physics of Solids*, 11(2):127–140, 1963.

[43] D. J. Heeger and J. R. Bergen. Pyramid-based texture analysis/synthesis. *Proceedings., International Conference on Image Processing*, page 10, 1995.

[44] R. Hill. A Theory of the Yielding and Plastic Flow of Anisotropic Metals. *Proceedings of the Royal Society of London A: Mathematical, Physical and Engineering Sciences*, 193(1033):281–297, 1948.

[45] R. Hill. Elastic properties of reinforced solids: Some theoretical principles. *Journal of the Mechanics and Physics of Solids*, 11(5):357–372, 1963.

[46] R. Hill. A self-consistent mechanics of composite materials. *Journal of the Mechanics and Physics of Solids*, 13(4):213–222, 1965.

[47] Y. Holdstein, A. Fischer, L. Podshivalov, and P. Z. Bar-Yoseph. Volumetric texture synthesis of bone micro-structure as a base for scaffold design. In *2009 IEEE International Conference on Shape Modeling and Applications, SMI 2009*, pages 81–88. IEEE, jun 2009.

[48] S. J. Hollister and N. Kikuehi. A comparison of homogenization and standard mechanics analyses for periodic porous composites. *Computational Mechanics*, pages 73–95, 1992.

[49] Y. Hu, V. Y. Blouin, and G. M. Fadel. Design for Manufacturing of 3D Heterogeneous Objects With Processing Time Consideration. *Journal of Mechanical Design*, 130(3):031701, 2008.

[50] J. Huang, G. M. Fadel, V. Y. Blouin, and M. Grujicic. Bi-objective optimization design of functionally gradient materials. *Materials & Design*, 23(7):657–666, 2002.

[51] A. T. Huber and L. J. Gibson. Anisotropy of foams. *Journal of Materials Science*, 23(8):3031–3040, 1988.

[52] D. W. Hutmacher. Scaffolds in tissue engineering bone and cartilage. *Biomaterials*, 21(24):2529–2543, 2000.

[53] D. Inglis and S. Pietruszczak. Characterization of anisotropy in porous media by means of linear intercept measurements. *International Journal of Solids and Structures*, 40(5):1243–1264, 2003.

[54] L. Jaworska, M. Rozmus, B. Królicka, and A. Twardowska. Functionally graded cermets. *Journal of Achievements in Materials and Manufacturing Engineering*, 17(1-2):73–76, 2006.

[55] C. Jiang, M. L. Giger, M. R. Chinander, J. M. Martell, S. Kwak, and M. J. Favus. Characterization of bone quality using computer-extracted radiographic features. *Medical physics*, 26(6):872–9, jun 1999.

[56] Z. Jiang, W. Chen, and C. Burkhart. Hybrid approach to 3d porous microstructure reconstruction via Gaussian random field. In *Proceedings of the ASME Design Engineering Technical Conference*, volume 2, pages 1033–1042, 2012.

[57] Y. Jiao, F. Stillinger, and S. Torquato. Modeling heterogeneous materials via two-point correlation functions: Basic principles. *Physical Review E*, 76(3):1–15, sep 2007.

[58] Y. Jiao, F. H. Stillinger, and S. Torquato. A superior descriptor of random textures and its predictive capacity. *Proceedings of the National Academy of Sciences of the United States of America*, 106(42):17634–9, 2009.

[59] Joachim Ohser and K. Schladitz. *3D Images of Materials Structures: Processing and Analysis*. Vch Pub, Weinheim, Germany, 2009.

[60] S. R. Kalidindi, M. Binci, D. Fullwood, and B. L. Adams. Elastic properties closures using second-order homogenization theories: Case studies in composites of two isotropic constituents. *Acta Materialia*, 54(11):3117–3126, jun 2006.

[61] T. Kanit, S. Forest, I. Galliet, V. Mounoury, and D. Jeulin. Determination of the size of the representative volume element for random composites: Statistical and numerical approach. *International Journal of Solids and Structures*, 40(13-14):3647–3679, 2003.

[62] W. S. Kendall and M. V. Lieshout. *Stochastic Geometry: Likelihood and Computation*. Monographs on statistics and applied probability. Chapman & Hall/CRC, 1998.

[63] R. A. Ketcham and T. M. Ryan. Quantification and visualization of anisotropy in trabecular bone. *Journal of Microscopy*, 213(2):158–171, 2004.

[64] J. Korringa. Theory of elastic constants of heterogeneous media. *Journal of Mathematical Physics*, 14(4):509–513, 1973.

[65] X. Kou and S. Tan. Heterogeneous object modeling: A review. *Computer-Aided Design*, 39(4):284–301, apr 2007.

[66] X. Kou and S. Tan. A simple and effective geometric representation for irregular porous structure modeling. *Computer-Aided Design*, 42(10):930–941, oct 2010.

[67] X. Kou and S. S. Tan. Modeling Functionally Graded Porous Structures with Stochastic Voronoi Diagram and B-Spline Representations. In *2010 International Conference on Manufacturing Automation*, pages 99–106. IEEE, 2010.

[68] P. Koutsourelakis and G. Deodatis. Simulation of multidimensional binary random fields with application to modeling of two-phase random media. *Journal of engineering mechanics*, (June):619–631, 2006.

[69] E. Kröner. Bounds for effective elastic moduli of disordered materials. *Journal of the Mechanics and Physics of Solids*, 25(2):137–155, 1977.

[70] A. Kumar, L. Nguyen, M. Degraef, and V. Sundararaghavan. A Markov random field approach for microstructure synthesis. *Modelling and Simulation in Materials Science and Engineering*, page 35015, 2016.

[71] C. Lang, J. Ohser, and R. Hilfer. On the analysis of spatial binary images. *Journal of microscopy*, 203(Pt 3):303–13, sep 2001.

[72] F. Latief, A. Biswas, U. Fauzi, and R. Hilfer. Continuum reconstruction of the pore scale microstructure for Fontainebleau sandstone. *Physica A: Statistical Mechanics and its Applications*, 389(8):1607–1618, apr 2010.

[73] S. Lefebvre and H. Hoppe. Parallel controllable texture synthesis. *ACM Transactions on Graphics*, 24(3):777, jul 2005.

[74] S. Lefebvre and H. Hoppe. Appearance-space texture synthesis. *ACM Transactions on Graphics*, 25(3):541, jul 2006.

[75] D. Legland, K. Kiêu, and M. Devaux. Computation of Minkowski measures on 2D and 3D binary images. *Image Analysis and Stereology*, pages 83–92, 2007.

[76] E. Levina and P. J. Bickel. Texture synthesis and nonparametric resampling of random fields. *The Annals of Statistics*, 34(4):1751–1773, aug 2006.

[77] H. Liu, T. Maekawa, N. M. Patrikalakis, E. M. Sachs, and W. Cho. Methods for feature-based design of heterogeneous solids. *Computer-Aided Design*, 36(12):1141–1159, 2004.

[78] K. Liu and A. Tovar. An efficient 3D topology optimization code written in Matlab. *Structural and Multidisciplinary Optimization*, pages 1175–1196, 2014.

[79] X. Liu and V. Shapiro. Random Heterogeneous Materials via Texture Synthesis. *Computational Materials Science*, 99:177–189, 2014.

[80] X. Liu and V. Shapiro. Homogenization of material properties in additively manufactured structures. *Computer-Aided Design*, 78:71–82, may 2016.

[81] X. Liu and V. Shapiro. Sample-based Design of Functionally Graded Material Structures. In *2016 International Design Engineering Technical Conferences and Computers and Information in Engineering Conference*. American Society of Mechanical Engineers, 2016.

[82] X. Liu and V. Shapiro. Sample-based synthesis of two-scale structures with anisotropy. *Computer-Aided Design*, Accepted, 2017.

[83] Y. Liu, W. Lin, and J. Hays. Near-regular texture analysis and manipulation. In *ACM Transactions on Graphics (TOG)*, volume 23, pages 368–376. ACM, 2004.

[84] Y. Liu, M. Steven Greene, W. Chen, D. Dikin, and W. K. Liu. Computational microstructure characterization and reconstruction for stochastic multiscale material design. *Computer-Aided Design*, 45(1):65–76, apr 2013.

[85] LORD KELVIN (W. THOMSON). Elements of a Mathematical Theory of Elasticity. *Philosophical Transactions of the Royal Society of London*, 146:481–498, 1856.

[86] P. Louis and A. M. Gokhale. Application of Image Analysis for Characterization of Spatial Arrangements of Features in Microstructure. *Metallurgical and Materials Transactions A*, 26(6):1449–1456, 1995.

[87] R. M. Mahamood, E. T. A. Member, M. Shukla, and S. Pityana. Functionally Graded Material : An Overview. *World Congress on Engineering*, III:2–6, 2012.

[88] M. S. Mamadapur. *Constitutive Modeling of Fused Deposition Modeling Acrylonitrile Butadiene Styrene (ABS)*. PhD thesis, Texas A&M University, 2007.

[89] C. Manwart and R. Hilfer. Reconstruction of random media using Monte Carlo methods. *Physical review. E, Statistical physics, plasmas, fluids, and related interdisciplinary topics*, 59(5 Pt B):5596–9, may 1999.

[90] C. Manwart, S. Torquato, and R. Hilfer. Stochastic reconstruction of sandstones. *Physical review. E, Statistical physics, plasmas, fluids, and related interdisciplinary topics*, 62(1 Pt B):893–9, jul 2000.

[91] W. B. March, A. J. Connolly, and A. G. Gray. Fast algorithms for comprehensive n-point correlation estimates. *Proceedings of the 18th ACM SIGKDD international conference on Knowledge discovery and data mining - KDD '12*, page 1478, 2012.

[92] F. A. Marin, R. H. R. Wechsler, J. A. Frieman, R. C. Nichol, and F. Marín. Modeling the Galaxy Three-Point Correlation Function. *The Astrophysical Journal*, 672(2):849–860, 2008.

[93] W. Matusik, M. Zwicker, and F. Durand. Texture design using a simplicial complex of morphable textures. *ACM Transactions on Graphics*, 24(3):787, 2005.

[94] B. McCarthy. Characterization of geometric deviations in FDM. Master's thesis, University of Wisconsin, Madison, 2015.

[95] K. R. Mecke. Additivity, Convexity, and Beyond: Applications of Minkowski Functionals in Statistical Physics. *Statistical Physics and Spatial Statistics*, pages 111–184, 2000.

[96] K. R. Mecke, T. Buchert, and H. Wagner. Robust Morphological Measures for Large-Scale Structure in the Universe. *Astronomy & Astrophysics*, 288:17, 1994.

[97] K. R. Mecke and D. Stoyan. *Statistical physics and spatial statistics: the art of analyzing and modeling spatial structures and pattern formation*. Lecture notes in physics. Springer, 2000.

[98] H. Mehboob and S.-H. Chang. Optimal design of a functionally graded biodegradable composite bone plate by using the Taguchi method and finite element analysis. *Composite Structures*, 119:166–173, 2015.

[99] M. M. Mehrabadi and S. C. Cowin. Eigentensors of linear anisotropic elastic materials. *Quarterly Journal of Mechanics and Applied Mathematics*, 44(2):331, 1991.

[100] J. C. Michel, H. Moulinec, and P. Suquet. A computational scheme for linear and non-linear composites with arbitrary phase contrast. In *5th U.S. National Congress on Computational Mechanics, 4-6 Aug. 1999*, volume 52, pages 139–160, 2001.

[101] G. Milton. *Theory of Composites*. Cambridge university press, 2002.

[102] G. W. Milton. Bounds on the elastic and transport properties of two-component composites. *Journal of the Mechanics and Physics of Solids*, 30(3):177–191, 1982.

[103] I. C. C. o. P.-s. Modelling. Berea Sandstone. aug 2014.

[104] R. Monetti, J. Bauer, I. Sidorenko, D. Müller, E. Rummeny, M. Matsuura, F. Eckstein, E.-M. Lochmüller, P. Zysset, and C. Räth. Assessment of the human trabecular bone structure using Minkowski functionals. In X. P. Hu and A. V. Clough, editors, *Medical Imaging 2009: Biomedical Applications in Molecular, Structural, and Functional Imaging*, volume 7262, page 72620N. Society of Photo-Optical Instrumentation Engineers, feb 2009.

[105] T. Mori and K. Tanaka. Average stress in matrix and average elastic energy of materials with misfitting inclusions. *Acta Metallurgica*, 21(5):571–574, 1973.

[106] S. Moser. Mesostructured Cellular Materials Generator.

[107] H. Moulinec and P. Suquet. A numerical method for computing the overall response of nonlinear composites with complex microstructure. *Computer Methods in Applied Mechanics and Engineering*, 157(1-2):69–94, 1998.

[108] R. Murugan and S. Ramakrishna. Design strategies of tissue engineering scaffolds with controlled fiber orientation. *Tissue Engineering*, 13(8):1845–1866, 2007.

[109] S. Niezgoda, D. M. Turner, D. Fullwood, and S. R. Kalidindi. Optimized structure based representative volume element sets reflecting the ensemble-averaged 2-point statistics. *Acta Materialia*, 58(13):4432–4445, aug 2010.

[110] F. Nogata and H. Takahashi. Intelligent functionally graded material: Bamboo. *Composites Engineering*, 5(7):743–751, jan 1995.

[111] A. Odgaard, E. B. Jensen, and H. J. Gundersen. Estimation of structural anisotropy based on volume orientation. A new concept. *Journal of microscopy*, 157(Pt 2):149–162, 1990.

[112] N. Oxman, S. Keating, and E. Tsai. Functionally Graded Rapid Prototyping. In *Innovative Developments in Virtual and Physical Prototyping*, pages 483–489. CRC Press, Boca Raton, Florida, sep 2011.

[113] R. Paget and I. D. Longstaff. Texture synthesis via a noncausal nonparametric multiscale Markov random field. *IEEE transactions on image processing : a publication of the IEEE Signal Processing Society*, 7(6):925–31, jan 1998.

[114] J. H. Panchal, S. R. Kalidindi, and D. L. McDowell. Key computational modeling issues in Integrated Computational Materials Engineering. *Computer-Aided Design*, 45(1):4–25, jan 2013.

[115] S.-M. Park, R. H. Crawford, and J. J. Beaman. Volumetric multi-texturing for functionally gradient material representation. In *Proceedings of the sixth ACM symposium on Solid modeling and applications - SMA '01*, SMA '01, pages 216–224, New York, NY, USA, 2001. ACM.

[116] A. Pasko, V. Adzhiev, B. Schmitt, and C. Schlick. Constructive hypervolume modeling. *Graphical models*, 63(6):413–442, 2001.

[117] A. Pasko, O. Fryazinov, T. Vilbrandt, P.-A. Fayolle, and V. Adzhiev. Procedural function-based modelling of volumetric microstructures. *Graphical Models*, 73(5):165–181, 2011.

[118] P. Pedersen. Simple transformations by proper contracted forms: can we change the usual practice? *Communications in Numerical Methods in Engineering*, 11(10):821–829, 1995.

[119] M. Pernice. *Fabric Tensor-based Poroelastic Materials: a" Direct" Approach*. PhD thesis, Università degli Studi di Napoli Federico II, 2008.

[120] A. C. Pipkin. *A Course on Integral Equations*. Springer Science & Business Media, 1991.

[121] X. Qian and D. Dutta. Design of heterogeneous turbine blade. *Computer-Aided Design*, 35(3):319–329, 2003.

[122] C. Redenbach. Microstructure models for cellular materials. *Computational Materials Science*, 44(4):1397–1407, 2009.

[123] C. Redenbach, O. Wirjadi, S. Rief, and A. Wiegmann. Modeling of ceramic foams for filtration simulation. *Advanced Engineering Materials*, 13(3):171–177, 2011.

[124] I. E. Reimanis. Functionally Graded Materials. In *Handbook of Advanced Materials*, pages 465–486. John Wiley & Sons, Inc., 2004.

[125] A. P. Roberts and E. J. Garboczi. Computation of the linear elastic properties of random porous materials with a wide variety of microstructure. *Proceedings of the Royal Society of London A: Mathematical, Physical and Engineering Sciences*, 458(2021):1033–1054, 2002.

[126] G. Saheli, H. Garmestani, and B. L. Adams. Microstructure design of a two phase composite using two-point correlation functions. *Journal of ComputerAided Materials Design*, 11(2-3):103–115, 2005.

[127] M. Saitou and Y. Fukuoka. Stripe pattern formation in Ag-Sb co-electrodeposition. In *Electrochimica Acta*, volume 50, pages 5044–5049, 2005.

[128] G. E. Schröder-Turk, S. Kapfer, B. Breidenbach, C. Beisbart, and K. R. Mecke. Tensorial Minkowski functionals and anisotropy measures for planar patterns. *Journal of microscopy*, 238(1):57–74, apr 2010.

[129] G. E. Schröder-Turk, W. Mickel, S. C. Kapfer, F. M. Schaller, B. Breidenbach, D. Hug, and K. R. Mecke. Minkowski tensors of anisotropic spatial structure. *New Journal of Physics*, 15(8):083028, aug 2013.

[130] C. Schroeder, W. Regli, a. Shokoufandeh, and W. Sun. Computer-aided design of porous artifacts. *Computer-Aided Design*, 37(3):339–353, mar 2005.

[131] L. I. Sedov and P. G. Hodge. *Introduction to the Mechanics of a Continuous Medium*, volume 33 of *Prentice-Hall series in engineering of the physical sciences*. Prentice-Hall, 1966.

[132] C. C. Seepersad, J. K. Allen, D. L. McDowell, and F. Mistree. Robust Design of Cellular Materials With Topological and Dimensional Imperfections. *Journal of Mechanical Design*, 128(6):1285, 2006.

[133] J. R. Shewchuk. An Introduction to the Conjugate Gradient Method Without the Agonizing Pain. *Science*, 49(CS-94-125):64, 1994.

[134] O. Sigmund. Materials with prescribed constitutive parameters: An inverse homogenization problem. *International Journal of Solids and Structures*, 31(17):2313–2329, 1994.

[135] O. Sigmund. Systematic design of metamaterials by topology optimization. *IUTAM Symposium on Modelling Nanomaterials and Nanosystems*, pages 151–159, 2009.

[136] O. Sigmund and S. Torquato. Design of smart composite materials using topology optimization. *Smart Materials and Structures*, 8(3):365–379, jun 1999.

[137] E. C. N. Silva, M. C. Walters, and G. H. Paulino. Modeling bamboo as a functionally graded material: Lessons for the analysis of affordable materials. *Journal of Materials Science*, 41(21):6991–7004, 2006.

[138] Y. K. Siu and S. T. Tan. 'Source-based' heterogeneous solid modeling. *Computer-Aided Design*, 34(1):41–55, jan 2002.

[139] S. S. M. J. Spence, M. Gioffrè, and M. Grigoriu. Probabilistic models and simulation of irregular masonry walls. *Journal of engineering mechanics*, 134(9):750–762, 2008.

[140] J. C. Steuben, A. P. Iliopoulos, and J. G. Michopoulos. Implicit slicing for functionally tailored additive manufacturing. *Computer-Aided Design*, 2015.

[141] D. Stoyan. *Basic Ideas of Spatial Statistics*, pages 3–21. Springer Berlin Heidelberg, Berlin, Heidelberg, 2000.

[142] D. Stoyan, W. S. Kendall, and J. Mecke. *Stochastic Geometry and Its Applications*. Wiley-interscience paperback series. John Wiley & Sons, 2008.

[143] D. Stoyan and K. R. Mecke. The Boolean model: from Matheron till today. In *Space, Structure and Randomness*, pages 151–181. Springer, New York, New York, USA, 2005.

[144] Q. Sun, G. Rizvi, C. Bellehumeur, and P. Gu. Effect of processing conditions on the bonding quality of FDM polymer filaments. *Rapid Prototyping Journal*, 14(2):72–80, 2008.

[145] Y.-j. Sung and R. Farnood. Characterizing Anisotropy of the Deterministic Features in Paper Structure with Wavelet Transforms. *Journal of Industrial and Engineering Chemistry*, 13(2):225–230, 2007.

[146] K. Suresh. Efficient Microstructural Design for Additive Manufacturing. In *ASME 2014 International Design Engineering Technical Conferences and Computers and Information in Engineering Conference*, pages V01AT02A045–V01AT02A045. American Society of Mechanical Engineers, 2014.

[147] K. Suzuki and N. Kikuchi. A homogenization method for shape and topology optimization. *Computer Methods in Applied Mechanics and Engineering*, 93(3):291–318, 1991.

[148] I. Szapudi. Introduction to higher order spatial statistics in cosmology. In *Data Analysis in Cosmology*, pages 457–492. Springer, 2009.

[149] P. Tahmasebi, A. Hezarkhani, and M. Sahimi. Multiple-point geostatistical modeling based on the cross-correlation functions. *Computational geosciences*, 16(3):779–797, 2012.

[150] D. R. S. Talbot and J. R. Willis. Bounds and self-consistent estimates for the overall properties of nonlinear composites. *IMA Journal of Applied Mathematics (Institute of Mathematics and Its Applications)*, 39(3):215–240, 1987.

[151] K. Terada, M. Hori, T. Kyoya, and N. Kikuchi. Simulation of the multi-scale convergence in computational homogenization approaches. *International Journal of Solids and Structures*, 37(16):2285–2311, 2000.

[152] A. Tewari, A. M. Gokhale, J. E. Spowart, and D. B. Miracle. Quantitative characterization of spatial clustering in three-dimensional microstructures using two-point correlation functions. *Acta Materialia*, 52(2):307–319, jan 2004.

[153] T. V. Thamaraiselvi and S. Rajeswari. Biological Evaluation of Bioceramic Materials - A Review. *Trends Biomater. Artif. Organs*,, 18(1):9–17, 2004.

[154] A. W. Toga and P. M. Thompson. Three-dimensional microimaging (MRμl and μCT), finite element modeling, and rapid prototyping provide unique insights into bone architecture in osteoporosis. *Anatomical Record*, 265(2):101–110, apr 2001.

[155] X. Tong, J. Zhang, L. Liu, X. Wang, B. Guo, and H.-Y. Shum. Synthesis of bidirectional texture functions on arbitrary surfaces. In *Proceedings of the 29th Annual Conference on Computer Graphics and Interactive Techniques*, volume 21 of *SIGGRAPH '02*, pages 665–672, New York, NY, USA, 2002. ACM.

[156] S. Torquato. Modeling of physical properties of composite materials. *International Journal of Solids and Structures*, 37(1-2):411–422, jan 2000.

[157] S. Torquato. *Random heterogeneous materials: microstructure and macroscopic properties*. Interdisciplinary applied mathematics: Mechanics and materials. Springer, New York, NY, USA, 2002.

[158] S. Torquato. Statistical Description of Microstructures. *Annual Review of Materials Research*, 32(1):77–111, aug 2002.

[159] S. Torquato, G. Stell, and J. Beasley. Third-order bounds on the effective bulk and shear modulus of a dispersion of fully penetrable spheres. *International Journal of Engineering Science*, 23(3):385–392, 1985.

[160] M. Tunák and a. Linka. Analysis of planar anisotropy of fibre systems by using 2D Fourier transform. *Fibres & Textiles in Eastern Europe*, 15(5):86–90, 2007.

[161] K. Vidimče, S.-P. Wang, J. Ragan-Kelley, and W. Matusik. OpenFab. *ACM Transactions on Graphics*, 32(4):1, 2013.

[162] V. Vinogradov and G. Milton. An accelerated FFT algorithm for thermoelastic and non-linear composites. *International Journal for Numerical Methods in Engineering*, 76(11):1678–1695, 2008.

[163] J. Vondrejc, J. Zeman, and I. Marek. An FFT-based Galerkin method for homogenization of periodic media. *Computers and Mathematics with Applications*, 68(3):156–173, 2014.

[164] L.-Y. Wei. *Texture synthesis by fixed neighborhood searching*. PhD thesis, Stanford University, Stanford, CA, USA, 2001.

[165] L.-Y. Wei, S. Lefebvre, V. Kwatra, and G. Turk. State of the art in example-based texture synthesis. In *Eurographics 2009, State of the Art Report, EG-STAR*, pages 93–117, 2009.

[166] L.-Y. Wei and M. Levoy. Fast texture synthesis using tree-structured vector quantization. *Proceedings of the 27th annual conference on Computer graphics and interactive techniques - SIGGRAPH '00*, pages 479–488, 2000.

[167] L.-Y. Wei and M. Levoy. Order-independent texture synthesis. *Computer Science Department, Stanford University*, pages 2000–2003, 2002.

[168] W. J. Whitehouse. The quantitative morphology of anisotropic trabecular bone. *Journal of microscopy*, 101(Pt 2):153–168, 1974.

[169] J. Willis. Bounds and self-consistent estimates for the overall properties of anisotropic composites. *Journal of the Mechanics and Physics of Solids*, 25(3):185–202, jun 1977.

[170] J. R. Willis. Variational and Related Methods for the Overall Properties of Composites. *Advances in Applied Mechanics*, 21(C):1–78, 1981.

[171] C.-T. Wu and R. L. McCullough. Constitutive relationships for heterogeneous materials(elastic properties of polycrystals and composite materials). *Developments in composite materials-1.(A 78-38276 16-24) London, Applied Science Publishers, Ltd.*, pages 119–187, 1977.

[172] H. Xu, D. Dikin, C. Burkhart, and W. Chen. Descriptor-based methodology for statistical characterization and 3D reconstruction of microstructural materials. *Computational Materials Science*, 85:206–216, apr 2014.

[173] H. Xu, Y. Li, L. C. Brinson, and W. Chen. A Descriptor-based Design Methodology for Developing Heterogeneous Microstructural Materials System. *Journal of Mechanical Design*, 136(May):1–12, feb 2014.

[174] C. Yeong and S. Torquato. Reconstructing random media. *Physical Review E*, 58(1):224–233, jul 1998.

[175] M. Yuan and L.-S. Turng. Microstructure and mechanical properties of microcellular injection molded polyamide-6 nanocomposites. *Polymer*, 46(18):7273–7292, aug 2005.

[176] J. Zeman, J. Vondejc, J. Novák, and I. Marek. Accelerating a FFT-based solver for numerical homogenization of periodic media by conjugate gradients. *Journal of Computational Physics*, 229(21):8065–8071, 2010.

[177] J. Zhang, K. Zhou, L. Velho, B. Guo, and H.-Y. Shum. Synthesis of progressively-variant textures on arbitrary surfaces. *ACM Transactions on Graphics*, 22(3):295, 2003.

[178] X. J. Zhang, K. Z. Chen, and X. A. Feng. Optimization of material properties needed for material design of components made of multi-heterogeneous materials. *Materials and Design*, 25(5):369–378, 2004.

[179] S. C. Zhu, Y. Wu, and D. Mumford. Filters, Random Fields and Maximum Entropy (FRAME): Towards a Unified Theory for Texture Modeling. *International Journal of Computer Vision*, 27(2):107–126, 1998.

[180] T. Zisis, A. Kordolemis, and A. E. Giannakopoulos. Development of Strong Surfaces Using Functionally Graded Composites Inspired by Natural Teeth - Finite Element and Experimental Verification. *Journal of Engineering Materials and Technology*, 132(1):011010, 2010.

[181] T. I. Zohdi. Basic microstructure-macroproperty calculations. In M. Kachanov and I. Sevostianov, editors, *Solid Mechanics and its Applications*, volume 193 of *Solid Mechanics and Its Applications*, pages 365–389. Springer Netherlands, Dordrecht, 2013.